Advanced functional nanomaterials for water remediation applications

Edited by Jagpreet Singh, Valeria De Matteis, Mikhael Bechelany and Akansha Mehta

Imprint

Green synthesis of biomass-derived carbon quantum dots for photocatalytic degradation of methylene blue

Dalia Chávez-García[*1], Mario Guzman[1], Viridiana Sanchez[1]
and Rubén D. Cadena-Nava[2]

Abstract

Water pollution, significantly influenced by the discharge of synthetic dyes from industries, such as textiles, poses a persistent global threat to human health. Among these dyes, methylene blue, particularly prevalent in the textile sector, exacerbates this issue. This study introduces an innovative approach to mitigate water pollution through the synthesis of nanomaterials using biomass-derived carbon quantum dots (CQDs) from grape pomace and watermelon peel. Utilizing the hydrothermal method at temperatures between 80 and 160 °C over periods ranging from 1 to 24 h, CQDs were successfully synthesized. A comprehensive characterization of the CQDs was performed using UV–visible spectroscopy, Fourier-transform infrared spectroscopy, dynamic light scattering, Raman spectroscopy, and luminescence spectroscopy, confirming their high quality. The photocatalytic activity of the CQDs in degrading methylene blue was evaluated under both sunlight and incandescent light irradiation, with measurements taken at 20 min intervals over a 2 h period. The CQDs, with sizes ranging from 1–10 nm, demonstrated notable optical properties, including upconversion and down-conversion luminescence. The results revealed effective photocatalytic degradation of methylene blue under sunlight, highlighting the potential for scalable production of these cost-effective catalytic nanomaterials for synthetic dye degradation.

Introduction

The textile industry is known for its high consumption of water, energy, and chemical reagents. For example, manufacturing a pair of indigo-dyed pants requires at least 42 L of water, plus approximately 21 L each time they are washed at home. To ensure product quality, textile dyes are designed to be resistant to light, detergents, and cleaning products, making them diffi-

cult to remove. When these dyes are released into water bodies, they cause pollution problems such as chemical oxygen demand, toxicity, and reduced light penetration, which affects aquatic life. As a result, the textile industry is a major contributor to water pollution [1,2].

To address this issue, the textile industry must adopt more sustainable practices in water and energy use, develop environmentally friendly dyes, and implement wastewater treatment processes. Conventional wastewater treatment techniques are often ineffective against resistant dyes, necessitating more advanced and sustainable technologies [3-7]. Embracing more sustainable practices and developing eco-friendly technologies are key to achieving a balance between textile production and environmental preservation [8-14]. Researchers are exploring innovative approaches, such as advanced oxidation processes, nanotechnology-based methods, and biological treatment systems, which show promise in effectively removing pollutants from wastewater [14-16].

In this research, we focus on the synthesis of carbon quantum dots (CQDs) through a hydrothermal method using biomass from watermelon peels and grape pomace. This method is chosen for its ease of production, low cost, and scalability. We aim to evaluate the potential of CQDs as catalysts in the photocatalytic degradation of methylene blue (MB) dye in industrial wastewater.

Photocatalysis is an environmentally friendly water purification method that uses light-activated catalysts to destroy contaminants, offering an advantage over traditional methods that merely transfer contaminants between phases [17-19]. While some studies on CQDs involve costly equipment, our approach uses green synthesis with biomass, aligning with eco-friendly principles [19-21].

Carbon quantum dots are valued for their easy synthesis, good solubility, photostability, nontoxic properties, and versatile applications. They can be synthesized using various methods, including top-down approaches such as arc discharge and laser ablation, and bottom-up methods such as hydrothermal and microwave synthesis [7,22] Biomass sources for CQD synthesis include eggshells, papaya peel, and lemon peel [23-39].

Applications of CQDs range from sensing and cell imaging to drug delivery, photocatalysis, and energy conversion [26-29]. In this study, biomass from watermelon shell and grape pomace waste is used as the carbon source. The hydrothermal method employing urea, nitric acid, and water is utilized. Samples synthesized with nitric acid demonstrated superior catalytic activity in MB degradation.

Carbon quantum dots typically exhibit luminescence properties, with emission peaks in the blue region between 450 and 500 nm varying based on the solvent used [26-28]. In our research, CQDs showed upconversion emission when excited at 900 nm and down-conversion emission in the blue region. The photocatalytic activity of CQDs, under sunlight irradiation, in MB degradation has been confirmed by various studies [32-38].

In this research, samples synthesized with nitric acid exhibited the best catalytic activity in MB degradation, while those prepared with water as a solvent did not show significant catalytic activity. The samples were also characterized using UV–visible spectra, Fourier-transform infrared spectroscopy (FTIR), Raman spectroscopy, dynamic light scattering (DLS), and photoluminescence spectroscopy (PL). The utilization of biomass as a carbon source offers great opportunities due to its abundance in nature and the wide range of sources available, which exhibit good luminescent and catalytic properties.

Focusing on the hydrothermal synthesis method using biomass-derived precursors, this research aims to develop a more sustainable and cost-effective approach for producing CQDs as catalysts in the photocatalysis process. Utilizing watermelon peels and grape pomace as raw materials contributes to waste valorization and promotes a circular economy concept. The ultimate goal is to provide a greener and more efficient solution for wastewater treatment in the textile industry, reducing environmental impact and conserving clean water resources. This research represents a significant step towards addressing water pollution caused by the textile industry, and highlights the potential of nanotechnology in developing sustainable solutions.

Experimental
Materials/material synthesis
The synthesis of CQDs involved the utilization of biomass-derived precursors. The method employed was based on the hydrothermal approach reported by Yuan et al. [40] with modifications in terms of precursor selection and chemical conditions.

Two organic materials, watermelon rind and grape pomace, were used as the precursors and were obtained from waste generated by the local wine industry. Initially, small pieces of the biomass were cut and placed on metal trays, followed by drying in a convection oven at 60 °C. Subsequently, the dried precursors were individually crushed in a mortar until they formed a fine powder. Additionally, four different synthesis schemes were proposed, involving modifications in the chemical conditions of the precursor solution.

In a typical synthesis, 50 mL of deionized water was mixed with 0.5 g of biomass precursor powder (dispersion A) and stirred for 10 min. Then, 1.0 g of urea (hydrolizing agent under hydrothermal conditions) was diluted in 50 mL of deionized water to form a homogeneous solution (solution B) and then mixed with dispersion A. The final mixture was stirred for an additional 10 min. Subsequently, the mixture was transferred to a Teflon-lined stainless steel autoclave, which was sealed under pressure using a manual press. The autoclave was then placed in a convection oven and maintained at 100°C for 2 h. After the specified time had elapsed, the autoclave was allowed to cool and the solution was retrieved. After the synthesis, the solutions were filtered through a Büchner funnel equipped with a 200 nm nylon membrane (Whatman) [30] and centrifuged at 15000 rpm for 20 min.

The process previously described was repeated modifying the chemical condition by varying solution B as follows: i) 1.0 g of urea in 50 mL of deionized water (samples M1 and M5); ii) 1.0 g of urea and 5.0 mL of nitric acid (69% v/v) in 50 mL of deionized water (samples M2 and M6); iii) 2.5 mL of nitric acid (69% v/v) in 50 mL of deionized water (samples M3 and M7); and iv) 50 mL of deionized water (M4 and M8). Samples M1, M2, M3, and M4 were prepared using grape pomace peel as the biomass precursor, and samples M5, M6, M7, and M8 were prepared using watermelon peel as the biomass precursor. This information is sumarized in Table 1.

Characterizations

To determine the optoelectronic characteristics of the synthesized CQDs, UV–vis absorption spectra were measured using a Thermo Scientific Evolution 220 spectrophotometer. The CQDs were dissolved in deionized water at a ratio of 1:10 (0.3 mg of CQDs per mL) and the measurements were taken in the range of 200–800 nm. A 1 cm path length quartz cell was used for the measurements, and deionized water was used as the blank in the measurement to account for background signals. Fourier-transform infrared spectra were measured on a Spectrum Two

FT-IR/Sp 10 S/W spectrometer (USA) with a LiTaO$_3$ type detector, the wavelength used ranged from 450 to 4000 cm^{-1}. The size distribution of the synthesized CQDs was determined via DLS, which relies on the measurement of the hydrodynamic radius of the particles. The CQDs were analyzed via a Malvern NanoSizer ZP instrument. The samples were diluted in deionized water to prevent signal saturation. Multiple measurements (at least three) were performed for each sample to ensure reliable and accurate measurements. A quartz cell with a 1 cm path length was used for the DLS measurements using a Malvern Zeta-sizer equipment model 7.2. Raman spectroscopy for all samples was performed in a Horiba Jobin Yvon Xplora Raman microscope using a 532 nm laser excitation as the power source. The photoluminescence spectra of the samples were obtained with an Agilent Cary Eclipse fluorescence spectrophotometer. It consists of two Czerny–Turner slits (excitation and emission) with a double monochromator and a continuous emission xenon light source (190–900 nm). All the samples were dispersed in deionized water and analyzed with an excitation wavelength of 350 and 900 nm in aqueous medium.

Photocatalytic evaluation

The photocatalytic activity of the synthesized CQDs was studied for the photodegradation of MB in aqueous media. The tests were separately conducted using sunlight and incandescent light (tungsten halogen lamp, 40 W). Previous to exposure, the reaction mixture was kept under vigorous stirring in the absence of light for 20 min to discard any adsorption effect. On the other hand, the pH value of the reaction mixture was kept constant during the test (pH 7). To initiate the catalytic process, each CQD sample was individually applied to the degradation of the MB dye. The UV–vis absorption spectrum of the dye was monitored using a spectrophotometer (Thermo Scientific Evolution model 220) with a 1 cm path length quartz cell.

To evaluate the photocatalytic activity of the CQDs, a suspension containing CQDs and MB (10 ppm initial concentration of MB) was placed in a baker under constant stirring. Before initi-

Table 1: Synthesis conditions for CQDs.

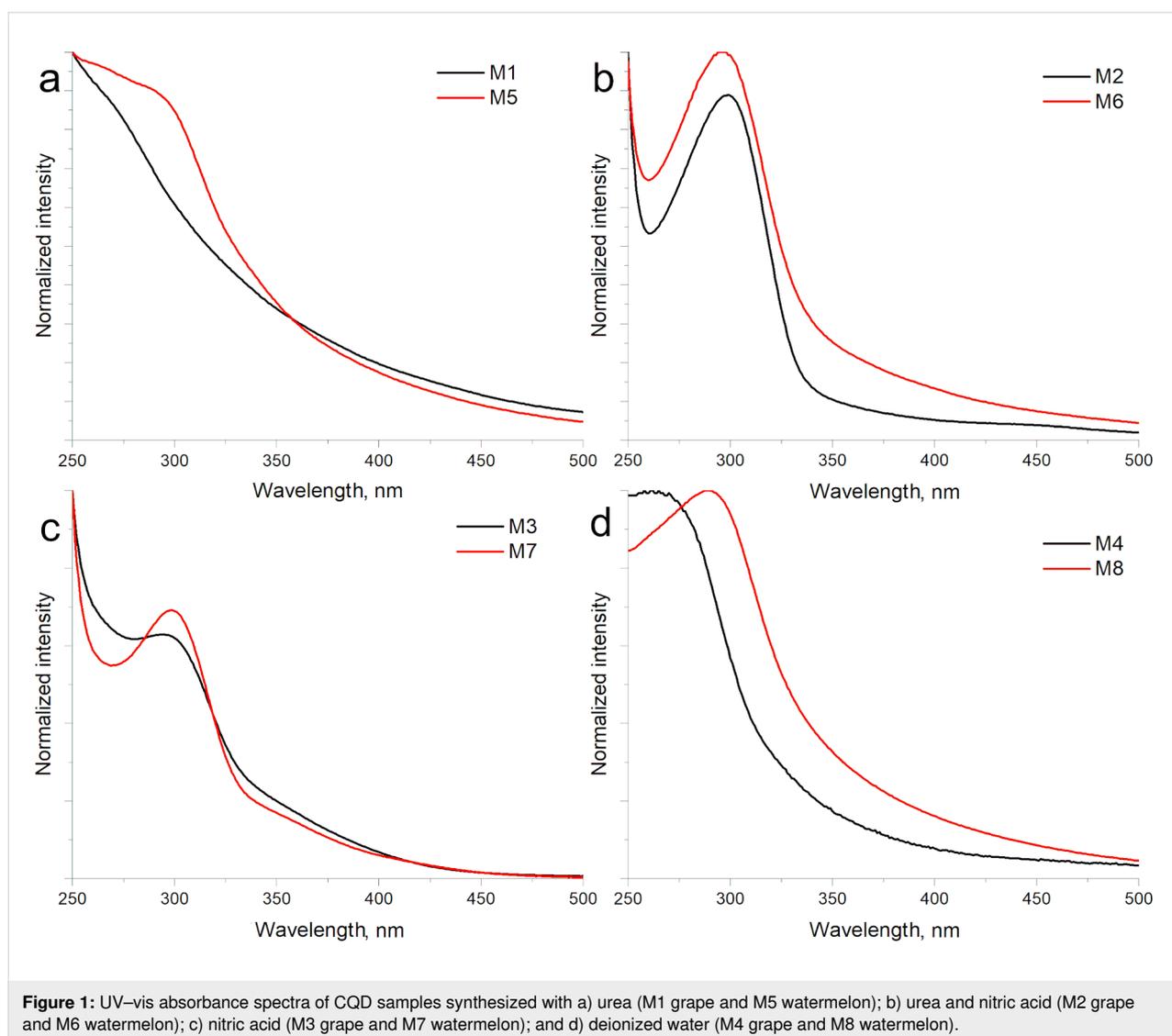| Sample	Carbon source	Chemical treatment	Hydrothermal conditions
M1	watermelon peel	urea	90 °C/2 h
M2	watermelon peel	nitric acid	90 °C/2 h
M3	watermelon peel	nitric acid + urea	90 °C/2 h
M4	watermelon peel	pure water	90 °C/2 h
M5	grape pomace	urea	90 °C/2 h
M6	grape pomace	nitric acid	90 °C/2 h
M7	grape pomace	nitric acid + urea	90 °C/2 h
M8	grape pomace	pure water	90 °C/2 h

ating the light irradiation, the suspension was stirred for 20 min at 400 rpm in a dark environment to ensure proper dispersion of the CQDs in aqueous media and the adsorption of the dye on the CQD surface. After the stirring period of 20 min, the solution absorbance was measured using a spectrophotometer in the wavelength range of 250–800 nm. This measurement marked the start of the photodegradation reaction under light radiation. In the case of tests conducted with incandescent light, a lamp was used as the light source, placed approximately 10 cm away from the solution, and the reaction was allowed to proceed for 100 min.

During the degradation tests, both sunlight and incandescent light were used, and the solution was continuously agitated. The absorbance of the solution was measured at 20 min intervals to monitor the progress of the degradation reaction. All samples were evaluated under both light sources.

Results and Discussion
UV–vis spectroscopy

UV–vis spectroscopy was used to analyze the optoelectronic properties of eight CQD samples synthesized by the hydrothermal method. All samples were diluted in deionized water to adjust the CQDs concentration to 0.3 mg/mL. Figure 1 shows the CQDs synthesized from grape pomace peel (Figure 1a) and watermelon peel (Figure 1b). It is observed that for each of the samples, its maximum absorption peak is approximately at 350 nm, which corresponds to $n–\pi^*$ transitions present in unsaturated compounds with heteroatoms (carbonyl groups). An absorbance tail is also noticed in the visible range [31,32]. The samples M6 and M7 (Figure 1b and Figure 1c) present a relatively symmetrical band also centered at 350 nm with a higher intensity for sample M6. Both samples were prepared using an oxidation process with nitric acid prior to the hydrothermal treatment to break the structure of the carbohydrate used. On

Figure 1: UV–vis absorbance spectra of CQD samples synthesized with a) urea (M1 grape and M5 watermelon); b) urea and nitric acid (M2 grape and M6 watermelon); c) nitric acid (M3 grape and M7 watermelon); and d) deionized water (M4 grape and M8 watermelon).

the other hand, samples M5 and M8 exhibit an asymmetric behavior in their absorption band centered around 340 nm. The difference can be associated with the polydispersity of the CQDs due to the absence of acid oxidation processes. In this case, the hydrothermal treatment is solely responsible for the formation of CQDs. This same condition was observed when modifying the type of precursor (grape pomace). However, in the case of the samples prepared from grape pomace, a considerably less intense band is observed for the systems prepared with urea (M1 and M5). This is possibly associated with a low production of CQDs (Figure 1a). Samples M1 and M5 exhibit a barely noticeable band between 250 and 300 nm, a typical peak was not observed for both samples probably due to the presence of some carbon impurity that hinder the detection of the π–π^* transition around 270 nm.

Dynamic light scattering

Figure 2 shows the size distribution of the CQDs by DLS. Notably, samples M2, M3, M6, and M7, synthesized with acid, exhibit characteristic sizes of quantum dots within the range of 1 to 10 nm. In contrast, samples M1 and M5, synthesized with urea, display larger sizes ranging from 10 to 100 nm, while samples M4 and M8, synthesized only using water, have sizes close to 100 nm. It is important to note that the samples prepared using grape pomace peel as the biomass source produced smaller particle sizes compared to those prepared with watermelon peel under identical synthesis conditions. The size distribution determined by DLS underlines the influence of biomass source and synthesis parameters on the resulting CQD dimensions.

Fourier-transform infrared spectroscopy

The surface chemical groups of the samples were analyzed using FTIR spectroscopy. Figure 3a displays the FTIR spectrum of the CQDs synthesized with grape pomace. Since the systems were prepared in water, some of the signals may have been shielded. In the spectrum, the absorption bands at 3350 cm^{-1} correspond to OH vibrations and N–H bonds, likely originating from water derived from the oxidation process. These bands are characteristic of the hydroxyl groups present in the acid structure. The peaks around 1600 cm^{-1} fall within the C–O range. The samples synthesized with nitric acid oxidation exhibit an additional peak at 1400 cm^{-1}, associated with C–H and C–N bending vibrations, indicating the introduction of nitrogen atoms and oxygen-containing groups. The oxidation process enhances the solubility of CQDs in water. The spectrum also shows low-intensity signals in the range of 1800 to 2500 cm^{-1}, which are characteristic of aromatic compounds [22,27].

In Figure 3b, the FTIR spectrum of the CQDs synthesized from watermelon peel is shown. Similar characteristics to the grape pomace CQDs samples can be observed, especially for sample M7, which was also synthesized using nitric acid (similar conditions as sample M3). However, the characteristic carbon/nitrogen groups of the acid, are not observed in sample M7. This could be attributed to the complete consumption of these groups during the treatment, resulting in their signals not being detected in this analysis.

Raman spectroscopy

Figure 4 shows the Raman spectra for all synthesized samples. On the left side, the spectra of the samples prepared from grape pomace are shown. Two broad bands appear in all samples, one centered around 1300 cm^{-1} and another one centered around 1550 cm^{-1}. These features can be related with the D and G bands, respectively [41]. The D band, usually centered around 1385 cm^{-1}, corresponds to C with an sp^3 hybridization and is commonly associated with disordered surfaces. On the other hand, the G band is typically located around 1575 cm^{-1}, and corresponds to C with an sp^2 hybridization which is related with the graphitic structure [41]. Nevertheless, all of our
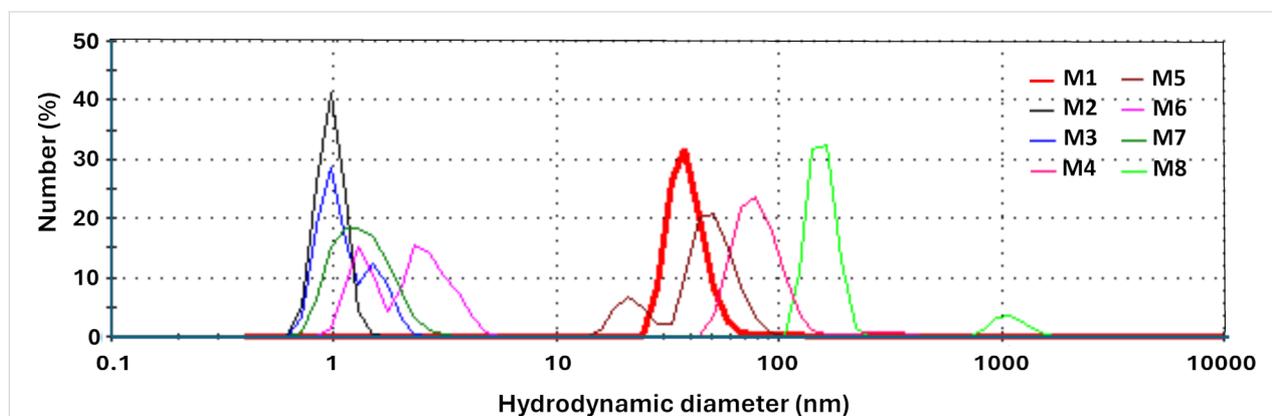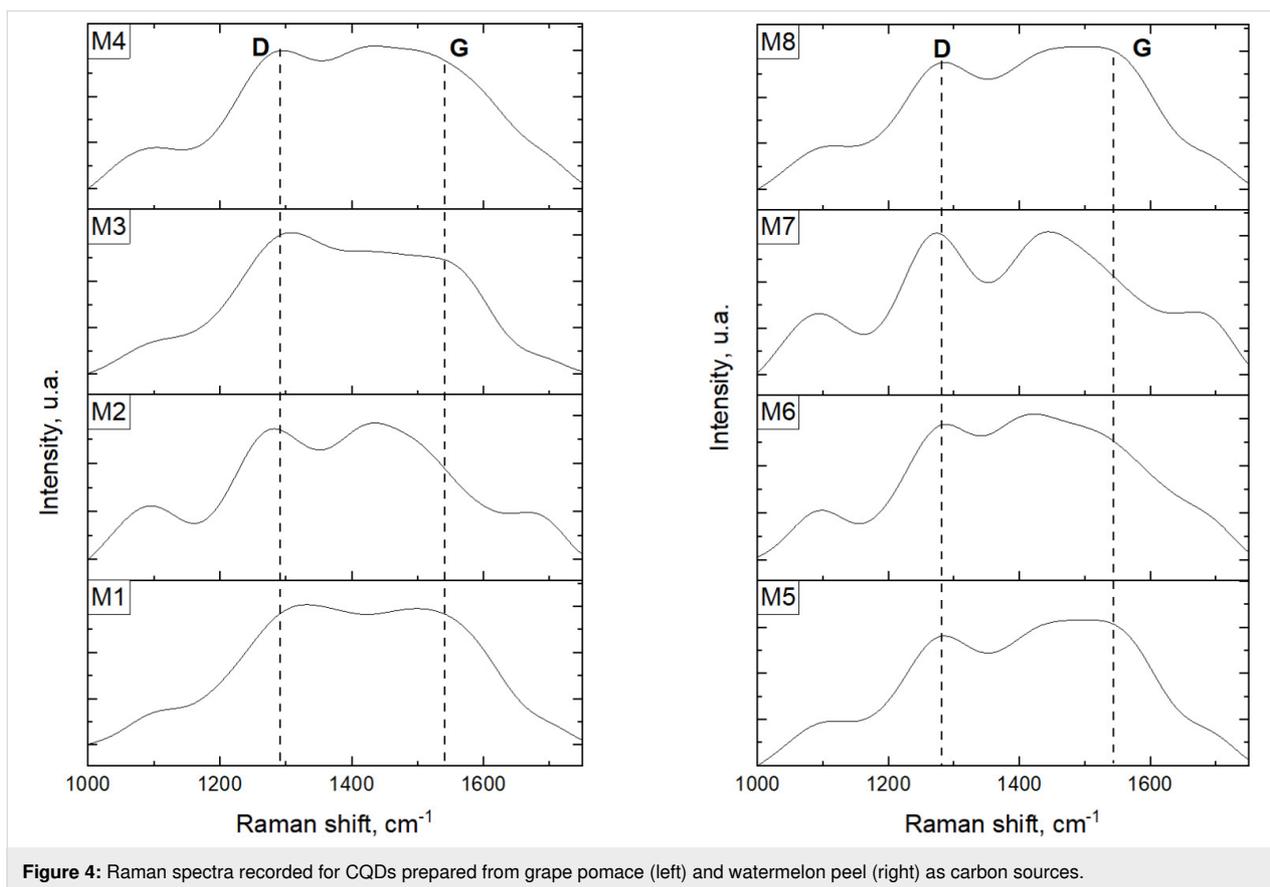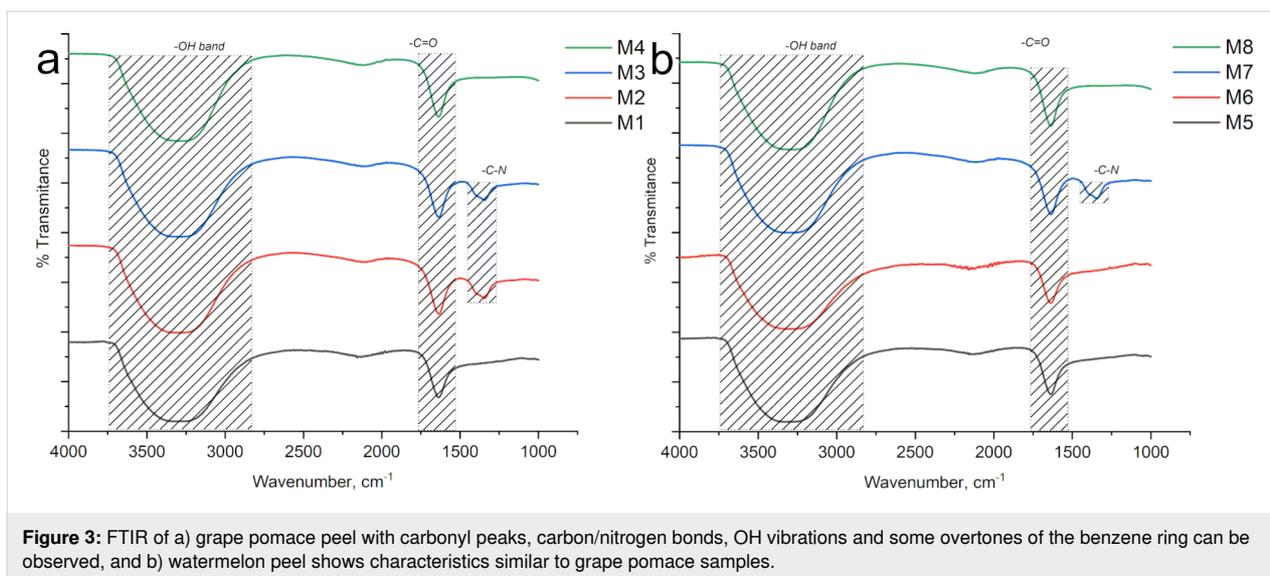

Figure 2: Size distribution of CQDs by dynamic light scattering.

Figure 3: FTIR of a) grape pomace peel with carbonyl peaks, carbon/nitrogen bonds, OH vibrations and some overtones of the benzene ring can be observed, and b) watermelon peel shows characteristics similar to grape pomace samples.

Figure 4: Raman spectra recorded for CQDs prepared from grape pomace (left) and watermelon peel (right) as carbon sources.

samples presents a noticeable broadening of the peak and a shift in the position of the D and G bands, similarly to what has been previously reported [18,42]. In both cases, such modification in the D and G bands was correlated with the presence of heteroatoms in the CQD structure. The synthesis method reported in this work involves chemical (nitric acid treatment) and physical conditions (hydrothermal treatment) which promotes the inclusion of heteroatoms into the CQDs. All the prepared CQDs samples presented an intensity ratio (I_D/I_G) around 1.0, which corresponds to a poor crystallinity in the CQDs and, as a consequence, a high relative content of defects.

Photoluminescence spectra

Investigating the underlying origin and mechanisms governing the multi-fluorescence behavior of carbon dots has garnered significant interest in recent times. Diverse research groups have delved into the fluorescence characteristics of CQDs, presenting varied mechanistic explanations. These encompass phenomena such as recombination of electron–hole pairs, quantum effects, surface functional groups, surface states, molecular states, and fluorophores exhibiting differing degrees of π-conjugation. Generally, CQDs comprise a carbon-core domain and surface domains [29].

In the context of PL processes in CQDs, the emission of fluorescence is intriguing and often associated with the presence of surface defects. Various researchers have highlighted the role of radiative recombination of electron–hole pairs and the influence of functional groups within the carbon network in driving the fluorescence phenomenon [24,30,31]. Furthermore, carbon nanomaterials exhibiting fluorescence, such as carbon oxide dots, exhibit a diverse array of structural elements, including sp^2 carbon hybridization or partial hybridization commonly observed in carbon oxide dots [30,31].

The PL down-conversion spectra of the CQDs synthesized from grape pomace and watermelon peel are shown in Figure 5a and Figure 5b, respectively. All samples were excited at a wavelength of 350 nm, and the emission was observed in the range of 440-450 nm. The samples prepared with urea, namely M1 and M5, exhibited higher intensity in the PL spectra. The PL emission of CQDs can also be influenced by the surrounding acidic conditions, potentially leading to fluorescence quenching. Notably, the sample M3 synthesized using nitric acid demon-

strated lower PL intensity, possibly due to such quenching effects under acidic conditions [32].

The upconversion luminescence observed in Figure 7 shows a phenomenon where the emitted fluorescence has a shorter wavelength than the excitation wavelength. This is different from the down-conversion luminescence, where the excitation occurs in the UV region and the emission takes place in the visible spectrum. Unlike down-conversion luminescence, upconversion luminescence does not require high photon density and can occur under normal excitation conditions [31]. Several authors have reported the existence of upconversion carbon dots (CDs). For example, Zhu et al. [43] demonstrated upconversion CDs, while Zhuo et al. [44] reported graphene CDs with upconversion luminescence. The theoretical framework proposed for upconversion photoluminescence centers on the concept of quantum confinement effect (QCE). In this scenario, electrons migrate from the lowest unoccupied molecular orbital (LUMO) to the highest occupied molecular orbital (HOMO) when the excitation wavelength surpasses 600 nm. This process is elucidated in Figure 6 [23,34].
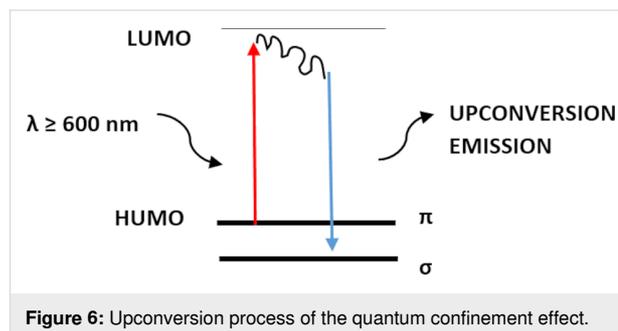

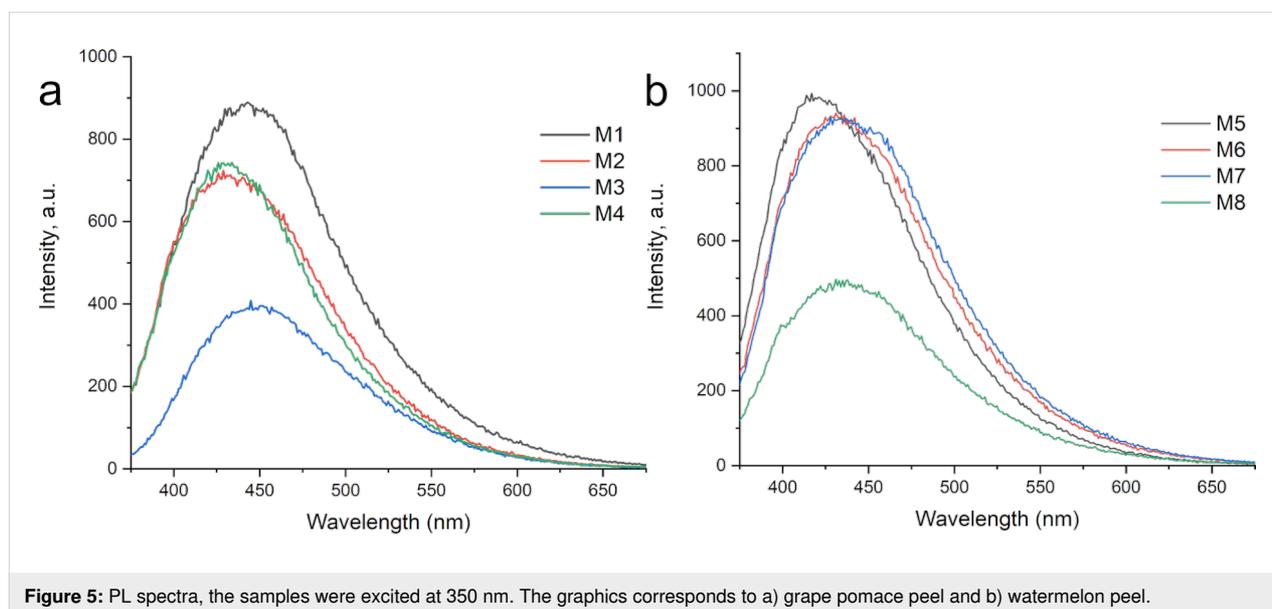**Figure 6:** Upconversion process of the quantum confinement effect.

Figure 5: PL spectra, the samples were excited at 350 nm. The graphics corresponds to a) grape pomace peel and b) watermelon peel.

In Figure 7 is observed the upconversion PL of all samples, with excitation at 900 nm and emission in the visible spectra at 720–730 nm. The samples from grape pomace were the ones with more emission than the samples from watermelon, showing similar behavior as the down-conversion process. Besides the main emission band centered around 720–730 nm, all samples exhibited a second band around 840 nm. Considering the upconversion PL mechanism, the authors consider that the presence of heteroatoms in the CQD structure promotes the formation of intermediary states, which may give place to a new emission band. A similar upconversion PL was reported by Wang et al., for CQDs obtained by the hydrothermal method and decorated with $BiVO_4$ [45].

Photocatalytic activity

To carry out the evaluation of the catalytic activity with each of the obtained samples, the curves were first fitted using the calculation of the reaction rate with the pseudo-first-order method. The calculation of the reaction rate constant can be performed using the first-order kinetic model. The first-order rate equation is given by:

$$\ln\left(\frac{C_0}{C}\right) = kt,$$

where C_0 is the initial concentration of the reactant (MB dye), C is the concentration of the reactant at time t, k is the first-order rate constant, and t is the reaction time.

The value of the kinetic rate constant (k) was estimated based on the slope of the linear fit of the $\ln(C_0/C)$ as a function of t (Figure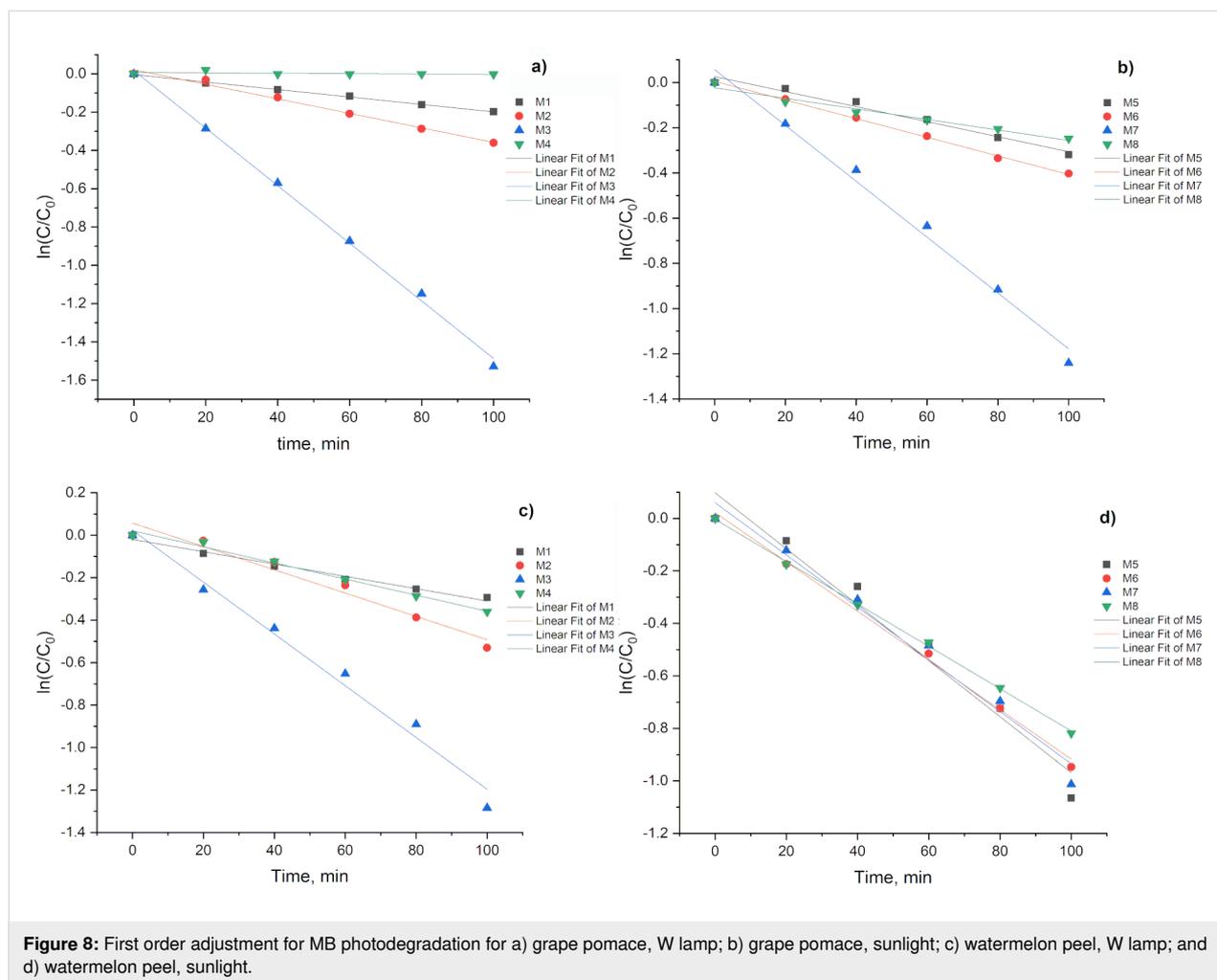 8). The concentration of MB was estimated based on the absorbance of the peak centered at 664 nm, using the Lambert–Beer law. As expected, the synthesized CQDs were catalytically active for the photodegradation of MB. All samples displayed a linear behavior and exhibited R^2 values around 0.98 for the degradation of the MB dye (Figure 8), except for the sample M4 under a tungsten 40 W lamp (W lamp), which did not show significant changes on the concentration of the MB. Besides, sample M8 displayed the second lowest rate constant, given that samples M4 and M8 were synthesized in the absence of any hydrolyzing agent (urea) or acidic compound (nitric acid). This led to poor degradation of organic matter, resulting in relatively large carbon structures (over 100 nm) as it was shown in Figure 4, which does not correspond to the size range of a CQD. Nevertheless, when these samples were exposed to sunlight, both exhibited a remarkable increment on their catalytic activity. This indicates that, even when the size on these carbon structures does not correspond to that of the CQDs, the photodegradation can be activated possibly due to an electron–hole pair on the surface of the carbon structure. Due to its size, the crystal structure effects can be enhanced.

The expected mechanism for the photodegradation of MB is related with the formation of electron–hole pairs that, due to their oxidizing properties, promotes the formation of OH^- radicals. These species are responsible for the mineralization of the MB molecule [38]. Other aspects that contribute to the MB degradation are the adsorption capacity of MB on the photocatalyst surface (i.e., CQD) and the specific surface area of the CQDs.

All samples (but M3 and M7) presented a similar behavior, increasing their photocatalytic activity when exposed to the
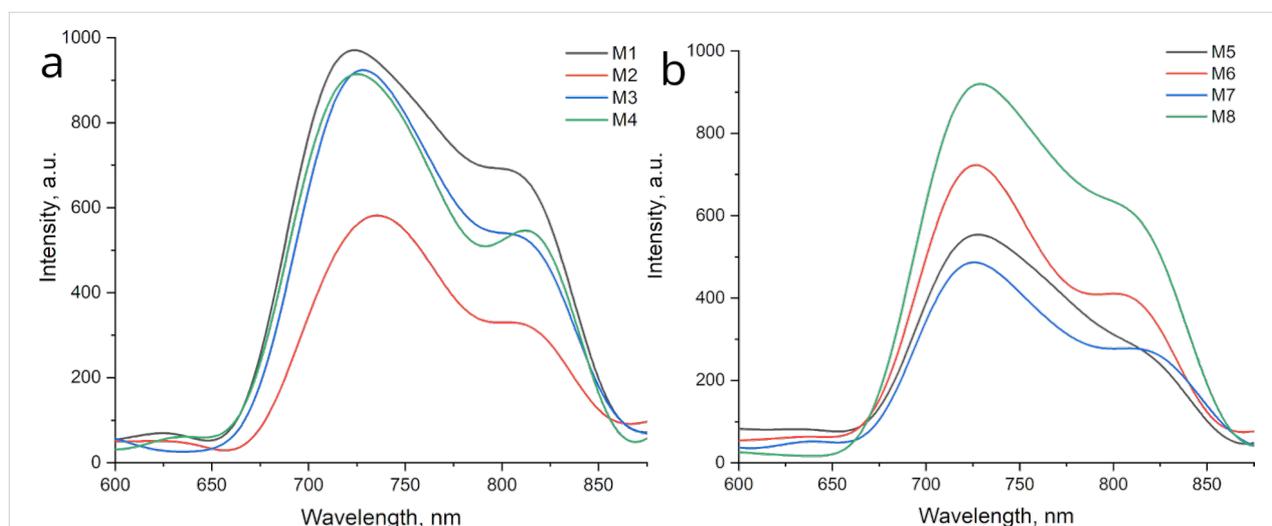
Figure 7: Upconversion PL of the samples, the graphics corresponds to grape pomace peel (M1 to M4) and watermelon peel (M5 to M8). Excitation wavelength: 900 nm.

Figure 8: First order adjustment for MB photodegradation for a) grape pomace, W lamp; b) grape pomace, sunlight; c) watermelon peel, W lamp; and d) watermelon peel, sunlight.

sunlight in comparison with their performance under incandescent lamp. It is commonly known that the sunlight emission spectrum presents a higher intensity at the ultraviolet range if compared to that of the tungsten lamp. Considering the band gap of the CQDs, we can affirm that sunlight does create electron–hole pairs more efficiently than the incandescent lamp, which increases the photocatalytic activity of the CQDs.

On the other hand, samples M3 and M7 displayed an opposed behavior, decreasing their photocatalytic activity when exposed to sunlight in comparison to the W lamp. Both samples were prepared under the same conditions but using two different sources of biomass. As nitric acid was used during the synthesis, the presence of C–N groups on the as-synthesized CQDs is expected, which was confirmed by FTIR spectroscopy (Figure 3). According to the report by Rani in 2018 [46], the presence of heteroatoms into the CQDs, such as oxygen, sulfur, and nitrogen, leads to interband states, which decreases the recombination speed of electron–hole pairs. Such delay enhances the photodegradation rate, which was observed for

both samples (M3 and M7) independently from the nature of the biomass source.

Considering that the MB molecule contains azo bonds consisting of double bonds (–N=N–), it is possible to foresee a strong interaction with C–N groups on the surface of species M3 and M7. On the other hand, such C–N groups could cause a shift in the electronic energy states [43], which facilitates the formation of electron–hole pairs when irradiated with a W lamp, resulting in a higher photocatalytic activity in comparison to that with sunlight irradiation.

Even when samples M2 and M6 were synthesized using also nitric acid, the formation of C–N groups on their surfaces could be attenuated by the urea (also used during this synthesis), given that above 90 °C urea decomposes forming basic species that can partially neutralize nitric acid acidity.

Additionally, the samples with smaller sizes (ranging from 1 to 10 nm) as determined by DLS, display higher catalytic activity.

Specifically, samples M4 and M8 synthesized from grape pomace and watermelon, respectively, show considerable catalytic activity under sunlight irradiation. However, when analyzed under incandescent light, these samples exhibit very low activity, likely due to their specific chemical composition and the variations in light intensity between the two light sources. The comparison of the kinetic rate constant (k) showing the catalytic activity is shown in Figure 9.
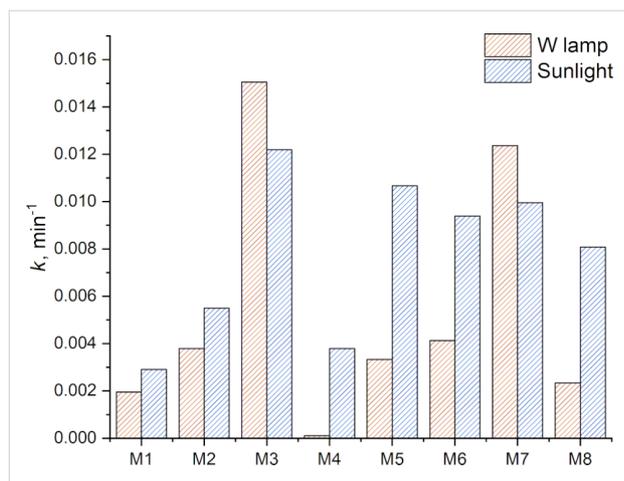
Figure 9: Rate constant values for the photocatalytic activity of CQDs synthesized from grape pomace and watermelon peel. (a) Sunlight radiation in blue, b) light radiation with W lamp in red.

Finally, in Figure 10, the percentages of degradation achieved for each of the catalysts under the irradiation of the two types of light are presented. These results confirm that sample M3 synthesized from grape pomace exhibits the highest level of degradation, reaching 78% under incandescent light and 72% under
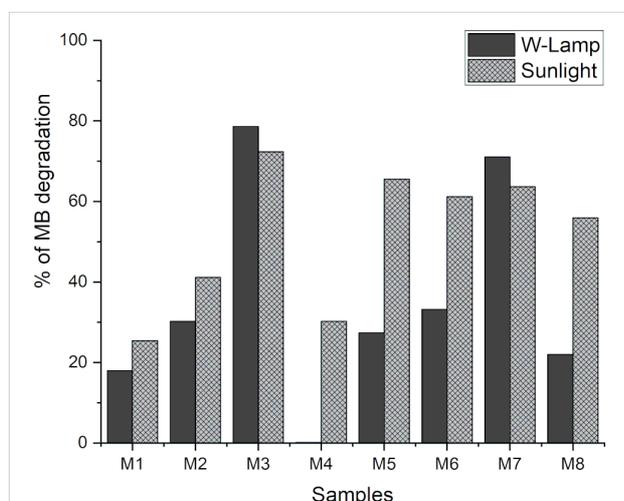
Figure 10: Percentage of MB degradation presented by CQDs to be used as catalysts in the degradation of MB dye. a) Solid bars: incandescent light, b) Hatched bars: solar light.

sunlight. Thus, it demonstrates superior activity compared to other reported CQDs used as catalysts, such as the nanomaterials obtained from uchuva and luminol.

The comparison of MB degradation from CQDs shows that most samples effectively degraded MB. Notably, samples M4 and M8, synthesized without certain compounds, exhibit limited activity under incandescent light but improve significantly under sunlight. Additionally, smaller-sized samples demonstrate higher catalytic activity, with sample M3 from grape pomace exhibiting superior performance compared to that of other reported CQDs.

Conclusion

The successful synthesis of luminescent and stable carbon quantum dots (CQDs) via the hydrothermal method using biomass as a precursor was achieved. We found that optimized synthesis parameters led to CQDs with diverse chemical characteristics. Notably, samples derived from grape pomace and watermelon peels synthesized with nitric acid, exhibited superior catalytic activity in methylene blue degradation, along with enhanced luminescence and stability compared to those synthesized with urea. It was also found that heteroatoms in the CQDs structure play an important role in the photocatalytic activity of the CQDs as well as in the upconversion photoluminescent behavior.

Our investigation also revealed that solar light was more effective than incandescent light in catalyzing reactions, and smaller-sized CQDs (1–10 nm) displayed higher catalytic activity, particularly evident in grape-pomace-derived samples. The superior performance of certain samples highlights the critical role of synthesis parameters and biomass sources in tailoring CQD properties for advanced photocatalytic applications. Furthermore, the assessment of luminescence activity unveiled the potential of CQDs for biomedical imaging, particularly with upconversion luminescence. This presents opportunities for targeted cell identification and drug delivery.

This study underscores the efficacy of the top-down hydrothermal method for CQD production, offering insights for tailored applications and emphasizing the potential of biomass-derived nanomaterials in environmental remediation and biomedicine, paving the way for the development of sustainable and effective technologies.

Acknowledgements

Conflicts of Interest

The authors declare no conflict of interest.

Author Contributions

Dalia Chávez-García: conceptualization; data curation; formal analysis; funding acquisition; investigation; methodology; project administration; resources; supervision; validation; visualization; writing – original draft; writing – review & editing. Mario Guzman: conceptualization; data curation; formal analysis; investigation; methodology; project administration; resources; software; supervision; validation; writing – review & editing. Viridiana Sanchez: data curation; formal analysis; investigation; validation. Rubén D. Cadena-Nava: formal analysis; investigation; resources; writing – review & editing.

ORCID® iDs

Dalia Chávez-García - https://orcid.org/0000-0002-1258-7238
Mario Guzman - https://orcid.org/0000-0002-0873-4936
Viridiana Sanchez - https://orcid.org/0009-0002-4517-3856
Rubén D. Cadena-Nava - https://orcid.org/0000-0001-8428-6701

Data Availability Statement

The data that supports the findings of this study is available from the corresponding author upon reasonable request.

Preprint

A non-peer-reviewed version of this article has been previously published as a preprint: https://doi.org/10.3762/bxiv.2024.12.v1

References

1. Sun, X.; Lei, Y. *TrAC, Trends Anal. Chem.* **2017,** *89,* 163–180. doi:10.1016/j.trac.2017.02.001
2. Khattab, T. A.; Abdelrahman, M. S.; Rehan, M. *Environ. Sci. Pollut. Res.* **2020,** *27,* 3803–3818. doi:10.1007/s11356-019-07137-z
3. Holkar, C. R.; Jadhav, A. J.; Pinjari, D. V.; Mahamuni, N. M.; Pandit, A. B. *J. Environ. Manage.* **2016,** *182,* 351–366. doi:10.1016/j.jenvman.2016.07.090
4. Verma, A. K.; Dash, R. R.; Bhunia, P. *J. Environ. Manage.* **2012,** *93,* 154–168. doi:10.1016/j.jenvman.2011.09.012
5. Ibupoto, A. S.; Qureshi, U. A.; Ahmed, F.; Khatri, Z.; Khatri, M.; Maqsood, M.; Brohi, R. Z.; Kim, I. S. *Chem. Eng. Res. Des.* **2018,** *136,* 744–752. doi:10.1016/j.cherd.2018.06.035
6. Asencios, Y. J. O.; Lourenço, V. S.; Carvalho, W. A. *Catal. Today* **2022,** *388–389,* 247–258. doi:10.1016/j.cattod.2020.06.064
7. Tang, L.; Ji, R.; Cao, X.; Lin, J.; Jiang, H.; Li, X.; Teng, K. S.; Luk, C. M.; Zeng, S.; Hao, J.; Lau, S. P. *ACS Nano* **2012,** *6,* 5102–5110. doi:10.1021/nn300760g
8. Fu, F.; Wang, Q. *J. Environ. Manage.* **2011,** *92,* 407–418. doi:10.1016/j.jenvman.2010.11.011
9. Sivakumar, R.; Lee, N. Y. *Chemosphere* **2022,** *286,* 131890. doi:10.1016/j.chemosphere.2021.131890
10. Khan, M.; Assal, M. E.; Tahir, M. N.; Khan, M.; Ashraf, M.; Hatshan, M. R.; Khan, M.; Varala, R.; Badawi, N. M.; Adil, S. F. *J. Saudi Chem. Soc.* **2022,** *26,* 101544. doi:10.1016/j.jscs.2022.101544
11. Wu, D.; Xie, X.; Zhang, Y.; Zhang, D.; Du, W.; Zhang, X.; Wang, B. *Front. Mater.* **2020,** *7,* 2. doi:10.3389/fmats.2020.00002
12. Shafique, M.; Mahr, M. S.; Yaseen, M.; Bhatti, H. N. *Mater. Chem. Phys.* **2022,** *278,* 125583. doi:10.1016/j.matchemphys.2021.125583
13. Frasco, M. F.; Chaniotakis, N. *Sensors* **2009,** *9,* 7266–7286. doi:10.3390/s90907266
14. SalmanOgli, A. *Cancer Nanotechnol.* **2011,** *2,* 1–19. doi:10.1007/s12645-011-0015-7
15. Wu, H.-F.; Gopal, J.; Abdelhamid, H. N.; Hasan, N. *Proteomics* **2012,** *12,* 2949–2961. doi:10.1002/pmic.201200295
16. Demchenko, A. P.; Dekaliuk, M. O. *Methods Appl. Fluoresc.* **2013,** *1,* 042001. doi:10.1088/2050-6120/1/4/042001
17. Li, H.; Kang, Z.; Liu, Y.; Lee, S.-T. *J. Mater. Chem.* **2012,** *22,* 24230–24253. doi:10.1039/c2jm34690g
18. Dong, Y.; Pang, H.; Yang, H. B.; Guo, C.; Shao, J.; Chi, Y.; Li, C. M.; Yu, T. *Angew. Chem., Int. Ed.* **2013,** *52,* 7800–7804. doi:10.1002/anie.201301114
19. Ehtesabi, H.; Nasri, R. *Adv. Nat. Sci.: Nanosci. Nanotechnol.* **2021,** *12,* 025006. doi:10.1088/2043-6262/abffc9
20. Miao, X.; Yan, X.; Qu, D.; Li, D.; Tao, F. F.; Sun, Z. *ACS Appl. Mater. Interfaces* **2017,** *9,* 18549–18556. doi:10.1021/acsami.7b04514
21. Ozyurt, D.; Kobaisi, M. A.; Hocking, R. K.; Fox, B. *Carbon Trends* **2023,** *12,* 100276. doi:10.1016/j.cartre.2023.100276
22. Wang, Y.; Hu, A. *J. Mater. Chem. C* **2014,** *2,* 6921–6939. doi:10.1039/c4tc00988f
23. Kang, C.; Huang, Y.; Yang, H.; Yan, X. F.; Chen, Z. P. *Nanomaterials* **2020,** *10,* 2316. doi:10.3390/nano10112316
24. Jusuf, B. N.; Sambudi, N. S.; Isnaeni; Samsuri, S. *J. Environ. Chem. Eng.* **2018,** *6,* 7426–7433. doi:10.1016/j.jece.2018.10.032
25. Wang, Q.; Liu, X.; Zhang, L.; Lv, Y. *Analyst* **2012,** *137,* 5392–5397. doi:10.1039/c2an36059d
26. Shahraki, H. S.; Bushra, R.; Shakeel, N.; Ahmad, A.; Quratulen; Ahmad, M.; Ritzoulis, C. *J. Bioresour. Bioprod.* **2023,** *8,* 162–175. doi:10.1016/j.jobab.2023.01.009
27. Tyagi, A.; Tripathi, K. M.; Singh, N.; Choudhary, S.; Gupta, R. K. *RSC Adv.* **2016,** *6,* 72423–72432. doi:10.1039/c6ra10488f
28. De, B.; Karak, N. *RSC Adv.* **2013,** *3,* 8286–8290. doi:10.1039/c3ra00088e
29. Sahu, S.; Behera, B.; Maiti, T. K.; Mohapatra, S. *Chem. Commun.* **2012,** *48,* 8835–8837. doi:10.1039/c2cc33796g
30. Sanchez-Sanchez, A.; Izquierdo, M. T.; Mathieu, S.; González-Álvarez, J.; Celzard, A.; Fierro, V. *Green Chem.* **2017,** *19,* 2653–2665. doi:10.1039/c7gc00491e
31. Liu, H.; Ye, T.; Mao, C. *Angew. Chem., Int. Ed.* **2007,** *46,* 6473–6475. doi:10.1002/anie.200701271
32. Prasannan, A.; Imae, T. *Ind. Eng. Chem. Res.* **2013,** *52,* 15673–15678. doi:10.1021/ie402421s
33. Kailasa, S. K. V.; Mehta, N.; Hasan, N.; Wu, H.-F. Applications of carbon dots in biosensing and cellular imaging. In *Nanobiomaterials in Medical Imaging Applications of Nanobiomaterials;* Grumezescu, A. M., Ed.; William Andrew Publishing: Oxford, UK, 2016; Vol. 8, pp 339–364. doi:10.1016/b978-0-323-41736-5.00011-x
34. Shen, J.; Zhu, Y.; Yang, X.; Li, C. *Chem. Commun.* **2012,** *48,* 3686–3699. doi:10.1039/c2cc00110a

35. Hu, C.; Li, M.; Qiu, J.; Sun, Y.-P. *Chem. Soc. Rev.* **2019,** *48,* 2315–2337. doi:10.1039/c8cs00750k
36. Singh, P.; Rani, N.; Kumar, S.; Kumar, P.; Mohan, B.; Pallavi; Bhankar, V.; Kataria, N.; Kumar, R.; Kumar, K. *J. Cleaner Prod.* **2023,** *413,* 137474. doi:10.1016/j.jclepro.2023.137474
37. Zhang, R.; Liu, Y.; Yu, L.; Li, Z.; Sun, S. *Nanotechnology* **2013,** *24,* 225601. doi:10.1088/0957-4484/24/22/225601
38. Cheng, C.; Shi, Y.; Li, M.; Xing, M.; Wu, Q. *Mater. Sci. Eng., C* **2017,** *79,* 473–480. doi:10.1016/j.msec.2017.05.094
39. Houas, A.; Lachheb, H.; Ksibi, M.; Elaloui, E.; Guillard, C.; Herrmann, J.-M. *Appl. Catal., B* **2001,** *31,* 145–157. doi:10.1016/s0926-3373(00)00276-9
40. Yuan, M.; Zhong, R.; Gao, H.; Li, W.; Yun, X.; Liu, J.; Zhao, X.; Zhao, G.; Zhang, F. *Appl. Surf. Sci.* **2015,** *355,* 1136–1144. doi:10.1016/j.apsusc.2015.07.095
41. Mathew, S. A.; Praveena, P.; Dhanavel, S.; Manikandan, R.; Senthilkumar, S.; Stephen, A. *RSC Adv.* **2020,** *10,* 24386–24396. doi:10.1039/d0ra04599c
42. Gao, D.; Zhang, Y.; Liu, A.; Zhu, Y.; Chen, S.; Wei, D.; Sun, J.; Guo, Z.; Fan, H. *Chem. Eng. J.* **2020,** *388,* 124199. doi:10.1016/j.cej.2020.124199
43. Zhu, S.; Song, Y.; Wang, J.; Wan, H.; Zhang, Y.; Ning, Y.; Yang, B. *Nano Today* **2017,** *13,* 10–14. doi:10.1016/j.nantod.2016.12.006
44. Zhuo, S.; Shao, M.; Lee, S.-T. *ACS Nano* **2012,** *6,* 1059–1064. doi:10.1021/nn2040395
45. Wang, G.; Zhang, W.; Li, J.; Dong, X.; Zhang, X. *J. Mater. Sci.* **2019,** *54,* 6488–6499. doi:10.1007/s10853-019-03316-y
46. Rani, U. A.; Ng, L. Y.; Ng, C. Y.; Mahmoudi, E.; Ng, Y.-S.; Mohammad, A. W. *J. Water Process Eng.* **2021,** *40,* 101816. doi:10.1016/j.jwpe.2020.101816

License and Terms

BEILSTEIN JOURNAL OF NANOTECHNOLOGY

Nanoarchitectonics with cetrimonium bromide on metal nanoparticles for linker-free detection of toxic metal ions and catalytic degradation of 4-nitrophenol

Akash Kumar[1,2] and Raja Gopal Rayavarapu[*1,2]

Full Research Paper

Address:
[1]Nanomaterial Toxicology Laboratory, Drug and Chemical Toxicology Group, Food, Drug and Chemical, Environment and Systems Toxicology (FEST) Divison, CSIR-Indian Institute of Toxicology Research (CSIR-IITR), Vishvigyan Bhawan, 31 Mahatma Gandhi Marg, Lucknow 226001, India and [2]Academy of Scientific and Innovative Research (AcSIR), Ghaziabad 201002, India

Email:
Raja Gopal Rayavarapu[*] - rajagopal@iitr.res.in

* Corresponding author

Abstract

Heavy metal ions and organic pollutants, such as 4-nitrophenol (4-NP), pose significant environmental and human health threats. Addressing these challenges necessitates using advanced nanoparticle-based systems capable of efficient detection and degradation. However, conventional approaches utilizing strong capping agents like cetrimonium bromide (CTAB) on nanoparticles lead to limitations due to the rigid nature of CTAB. This restricts its utility in heavy metal detection and 4-NP degradation, requiring additional surface modifications using linker molecules, thereby increasing process complexity and cost. To overcome these limitations, there is a critical need for the development of an easy-to-use, dual-functional, linker-free nanosystem capable of simultaneous detection of heavy metals and efficient degradation of 4-NP. For enabling linker-free/ligand-free detection of heavy metal ions and catalytic degradation of 4-NP, CTAB was engineered as a versatile capping agent on gold and silver nanoparticles. Various factors, including nanoparticle characteristics such as shape, size, metal composition, centrifugation, and NaOH amount, were investigated for their impact on the performance of CTAB-capped nanoparticles in heavy metal detection and 4-NP degradation. CTAB-Au nanospheres demonstrated limited heavy metal ion detection capability but exhibited remarkable efficiency in degrading 94.37% of 4-NP within 1 min. In contrast, silver nanospheres effectively detected Hg^{2+}, Cu^{2+}, and Fe^{3+} at concentrations as low as 1 ppm and degraded 90.78% of 4-NP within 30 min. Moreover, anisotropic gold nanorods (CTAB-AuNR1 and CTAB-AuNR2) showed promising sensing capabilities towards Cu^{2+}, Cr^{3+}, and Hg^{2+} at 0.5 OD, while efficiently degrading 4-NP within 5 min at 1 OD. This study emphasizes the importance of tailoring parameters of CTAB-capped nanoparticles for specific sensing and catalytic applications, offering potential solutions for environmental remediation and human health protection.

Introduction

Metal nanoparticles are widely used for a great number of applications owing to their excellent optochemical properties and high surface-to-volume ratio in comparison to bulk materials. Noble metal (gold and silver) nanoprobes are emerging as versatile colorimetric and spectrophotometric nanosensors for rapid detection/degradation of heavy metal ions and toxic pollutants that pose a serious challenge to environment and human health.

Globally, acceleration of industrial growth and urbanization led to the increased release of pollutants into the environment, causing health concerns to humans. Untreated industrial effluents are released, and most heavy metal ions accumulate in water higher than the permissible limits, pollute drinking water, and are non-biodegradable. Heavy metal ions are potentially carcinogenic, and it is hard to predict their toxicity at early stages of exposure. In addition, industrial wastewater may contain toxic compounds such as the widely used 4-nitrophenol [1]. Hence, one need is to develop a dual-functional and flexible linker-free metal nanoparticle-based sensor that is rapid and affordable for the detection of heavy metal ions as well as for the degradation of organic pollutants such as 4-nitrophenol.

Developing a robust sensing platform based on metal nanoparticles requires a modulation of the surface chemistry, which is governed by the choice of capping agents on the metal surface and further dominates functionalization. Various capping agents such as citrate, PVP, and surfactants have been the choice for metal nanoparticles. Controlled size, shape, and surface properties have been achieved using strong capping and reducing agents. Capping agents maintain size, shape, and stability of the nanoparticles, and suitable capping agents can modulate the nanoarchitectonics of the nanoparticles from atomic to molecular levels [2]. The surface capping can also influence the surface properties of the nanoparticles, making them compatible with specific environments or functional groups [3].

Surfactants bind to metal surfaces and create a stable colloidal solution by preventing the nanoparticles from aggregation or clustering [4]. CTAB is a widely used cationic surfactant that provides nanoparticle ionic stability and anisotropy [5]. Although CTAB delivers high strength to nanoparticles, the use of such nanoparticles is limited in sensing, catalysis, and biomedical applications because of post-synthesis functionalization, morphology, and toxicity [6-8]. CTAB is a resilient molecule on the nanoparticle surface because of its micellar structure and does not allow for interactions with ligands via ion–ion interactions. Therefore, multiple surface modifications or linkers must be used for selective interaction between ligand and CTAB-capped gold and silver nanoparticles [7,9].

Contaminants in form of heavy metals and pollutant such as 4-nitrophenol are both dangerous to humans [10,11]. Contamination with toxic heavy metal ions, including zinc, arsenic, aluminium, chromium, iron, cobalt, copper, nickel, mercury, cadmium, and lead, causes significant chronic damage to organ systems, beginning at the cellular level [12]. Toxic heavy metal ions such as Hg^{2+} are poisonous environmental pollutants that cause damage at the DNA level by inhibiting DNA replication and DNA polymerase activity, ultimately affecting normal cell synthesis [13]. The less toxic Fe^{3+} is an essential nutrient for human health in a lower dose, while increasing the dose also leads to undesirable side effects such as iron overload (hemochromatosis) and acute iron poisoning [14]. Similarly, other metals, including copper and cobalt, significantly damage different body parts above a threshold limit. Heavy metal ions pose a severe risk to human and environmental health [15]. Besides heavy metals, 4-nitrophenol is widely used for dye synthesis, insecticides and pesticides, indicators, and photographic chemicals [16]. Regarding the use of 4-nitrophenol, there are several toxicity concerns via different exposure routes, including dermal, oral, and inhalation [17]. Therefore, developing methods to detect heavy metals at the low concentrations usually found in environmental samples is crucial. Similarly, the removal of 4-nitrophenol from exposed site requires necessary steps.

Heavy metals are detected using high-throughput techniques, such as atomic absorption spectroscopy, atomic emission spectroscopy, surface-enhanced Raman scattering, electrochemical, fluorescence, and colorimetric methods [18,19]. Catalytic hydrogenation is the preferred method for the conversion of 4-nitrophenol to 4-aminophenol, which is less toxic [20]. However, the conversion process is laborious and requires precious metals such as palladium and platinum as catalysts [20]. Colorimetric detection methods have attracted attention because of their advantages, including simplicity, sensitivity, visualization, and real-time detection, while other methods often require expensive instrumentation and complex operational procedures [21]. Colorimetric detection of heavy metals and catalytic conversion of 4-nitrophenol can be achieved using CTAB-capped gold or silver nanoparticles because of their unique surface plasmon resonance (SPR) properties, allowing for a colorimetric analysis through a change in absorption wavelength. The color of gold and silver nanoparticles highly depends on shape, size, and pH value, which are directly influenced by the ligand–metal interaction [22]. Another essential factor is surface capping, which provides colloidal stability and the surface for ionic interaction with ligands [23]. Previously, post-synthesis surface-modified CTAB-capped gold and silver nanoparticles were used to detect various compounds, including heavy

metals [9,24]. Moudgil et al. showed that that poly-L-lysine-coated CTAB-AgNPs are selective and sensitive for detecting Hg^{2+} [9]. GSH-modified isotropic and anisotropic CTAB-AgNPs were used to detect cobalt ions. The author found that only rod-shaped particles enabled visual detection of cobalt [25]. Yagyu et al. showed the efficient removal of radioactive cesium using Prussian blue [26]. Also, 4-nitrophenol was degraded using CTAB-capped gold nanoparticles within 60 min of the reaction in the presence of thiosulfate [27]. The study concluded that nanoparticles of 13 nm can efficiently catalyze the reaction from 4-nitrophenol to 4-aminophenol [27].

A number of studies confirmed that linker-dependent detection and catalytic performance were available using CTAB-capped gold or silver nanoparticles. Unfortunately, only very few studies described CTAB-capped nanoparticles as detection and catalytic systems without surface modifications, linkers, or buffers because of the strong binding of CTAB on the nanoparticle surface. Designing CTAB-capped gold and silver nanoparticles without linker/buffer for catalysis and detection heavy metals is a current need. In this work, we have developed a linker-free nanosensor with CTAB as capping agent on both isotropic and anisotropic gold and silver nanoparticles. The CTAB-capped metal nanoparticles could sense heavy metal ions and also helped in the rapid catalytic degradation of 4-nitrophenol.

Materials and Methods
Materials
Cetrimonium bromide (CTAB) (Cat No. 52370), sodium borohydride ($NaBH_4$) (Cat No. 480886), and ascorbic acid (AA) (Cat No. A7506) were purchased from Sigma-Aldrich. Silver nitrate ($AgNO_3$) (Cat No. 1.93200.0027) and hydrochloric acid (HCl) (Cat No. 1.93001.2521) were obtained from Merck. Sodium hydroxide (NaOH) (Cat No. TC1460), chloroauric acid trihydrate ($HAuCl_4 \cdot 3H_2O$) (Cat No.10724SG001) and 4-nitrophenol (4-NP) (Cat No. 144956) were purchased from CDH fine chemicals, Finar and SRL chemicals, respectively. National Institute of Standard and Technology grade metal standards (1000 ppm) of arsenic (As^{3+}), aluminum (Al^{3+}), cadmium (Cd^{2+}), zinc (Zn^{2+}), mercury (Hg^{2+}), nickel (Ni^{2+}), copper (Cu^{2+}), chromium (Cr^{3+}), lead (Pb^{2+}), iron (Fe^{3+}), and cobalt (Co^{2+}) were purchased from CDH Fine Chemicals, India. The chemicals obtained were used without further purification. All glassware was cleaned with aqua regia and rinsed with double distilled (DD) water before use.

Cetrimonium bromide as capping agent
CTAB-AgNS (silver nanospheres) and CTAB-AuNS (gold nanospheres) were synthesized via wet chemical synthesis using slightly modified protocols [28,29]. In a typical synthesis

carried out at 80 °C, 0.5 mL of $AgNO_3$ (100 mM) was reduced using 1 mL of 100 mM $NaBH_4$ in the presence of 5 mL DD water premixed with 1 mL of 100 mM cetrimonium bromide (CTAB) under stirring at 800 rpm. Similarly, gold nanospheres were synthesized by adding 0.5 mL of 25 mM gold chloride solution to 5 mL of cetrimonium bromide (100 mM) followed with the addition of 0.5 mL $NaBH_4$ (100 mM) under stirring at 800 rpm. The silver and gold nanospheres were centrifuged at 18000g and 20000g for 20 min and 60 min, respectively, to remove impurities. The supernatants were discarded and the pellets were dispersed in DD water and stored at room temperature.

Tunable aspect ratio of gold nanorods capped with CTAB
Gold nanorods of different lengths were synthesized using a two-step protocol as described in previous reports with slight modifications [30]. Briefly, in the first step, gold seeds were prepared by mixing CTAB, $HAuCl_4 \cdot 3H_2O$ and $NaBH_4$. The seed solution acts as an initiator for synthesizing gold nanorods. In the second step, the growth solution was prepared, consisting of CTAB, $AgNO_3$, $HAuCl_4 \cdot 3H_2O$, HCl, and ascorbic acid. A typical synthesis involved the synthesis of CTAB-capped Au seeds of less than 4 nm. Addition to the growth solution in step 2 resulted in the formation of gold nanorods. The seeds were prepared using 200 µL of $HAuCl_4 \cdot 3H_2O$ (25 mM) with 2 mL of 0.1 M CTAB at 80 °C, followed by 800 µL freshly prepared ice-cold $NaBH_4$ (10 mM) added under continuous stirring (800 rpm). The Growth solution of 5 mL of CTAB (100 mM) was placed on a hot plate (80 °C), 500 µL of $HAuCl_4 \cdot 3H_2O$ (10 mM), 50 µL/120 µL (for shorter and longer nanorods, respectively) $AgNO_3$ (10 mM), 200 µL of HCl (1 M), and 80 µL of AA (100 mM) were sequentially added to the reaction mixture. Finally, 50 µL of freshly prepared seed solution was added to the growth solution to initiate the synthesis of gold nanorods. The different sizes of gold nanorods were obtained by varying the volume of $AgNO_3$ solution. Finally, anisotropic AuNR1 (shorter length) and AuNR2 (longer length) were centrifuged at 16,000g and 12,000g for 20 min, respectively, to remove excess of surfactant and any impurities.

Characterization of CTAB-capped isotropic and anisotropic metal nanoparticles
The plasmonic properties of the synthesized isotropic and anisotropic metal nanostructures were measured using an Epoch2 spectrophotometer (BioTek, USA). Hydrodynamic radius and polydispersity index (PDI) were measured using dynamic light scattering (Zetasizer Nano ZS, Malvern, UK). The zeta potential measurements were conducted to determine the surface charge for both isotropic and anisotropic metal nanoparticles using zeta cuvettes (DTS0012). The precise size

and morphology of CTAB-AgNS, CTAB-AuNS, CTAB-AuNR1, and CTAB-AuNR2 were observed under a transmission electron microscope (TEM, 120 kV; FEI Tecnai). The nanoparticles were placed onto 200-mesh carbon-coated copper grids. The average size of the nanoparticles was calculated using ImageJ software (USA). The crystal structure of CTAB-capped gold and silver nanoparticles was determined using XRD (Rigaku Smartlab, Japan) in a 2θ range of 35° to 80°. The nanoparticle solutions were air-dried, and the obtained powders (20 mg) were used for measurement. The functionalization of AgNS, AuNS, AuNR1, and AuNR2 with CTAB was validated through Fourier-transform infrared spectroscopy (Thermo Scientific, Nicolet iS5, USA). 10 mg of the air-dried nanoparticles were placed over a diamond and measured in the range of 400–4000 cm^{-1}.

Quantification of CTAB through UHPLC

The quantification of bound CTAB on the nanoparticles' surface was analyzed using ultrahigh-performance liquid chromatography (UHPLC; Shimadzu, Nexera, Tokyo, Japan). The chromatography system equipped with an SPD-M20A photodiode array (PDA) detector with a wavelength range of 190–800 nm, a degreaser (DGU-20A$_{5R}$), autosampler (SIL-30AD), and quaternary pump (LC-30AD). The separation peak for CTAB was analyzed using HpersilGold^{TM} C18 (100 × 2.1 mm, 10 μm) with a pore diameter of 1.9 μm. The injection volume was 5 μL, and the wavelength was 208 nm for CTAB quantification. The mobile phase included a mixture of acetonitrile and water (40:60 v/v) at a 0.2 mL/min flow rate. The method was developed using CTAB powder as standard at different concentrations of 0.625, 1.2, 2.5, 5, 10, and 20 μg/mL in water. The blank sample (which consisted only of solvent) was also analyzed to confirm the peak value of the compound. The supernatants of centrifuged CTAB-capped nanoparticles were used for CTAB quantification.

Stability of CTAB-capped metal nanoparticles in NaCl and NaOH solutions

In order to determine the ability and functionality of CTAB on metal nanoparticle surfaces, we have studied their stability in commonly used 1 M solutions of sodium chloride and sodium hydroxide. The stability of as-prepared and centrifuged nanoparticles of CTAB-AgNS, CTAB-AuNS, CTAB-AuNR1, and CTAB-AuNR2 were evaluated. The optical density (OD) of all CTAB-capped nanoparticles was kept in the vicinity of 0.5 ± 0.1 and 1.0 ± 0.1. Aliquots of 1 M NaOH (volumes ranging between 5–50 μL) was added to the nanoparticle solutions. Also, CTAB-AgNS, CTAB-AuNS, CTAB-AuNR1, and CTAB-AuNR2 were added to 1 M NaCl solution while keeping the optical density of the nanoparticles constant at 0.5 and 1.

Linker-free sensing of heavy metal ions

National Institute of Standard and Technology grade metal standards (1000 ppm) of As^{3+}, Al^{3+}, Cd^{2+}, Zn^{2+}, Hg^{2+}, Ni^{2+}, Cu^{2+}, Cr^{3+}, Pb^{2+}, Fe^{3+}, and Co^{2+} were diluted to a concentration of 10 ppm. A uniform concentration of nanoparticles in terms of optical density (OD) was maintained throughout the experiment. The concentration of CTAB-AgNS, CTAB-AuNS, CTAB-AuNR1, and CTAB-AuNR2 was kept at constant values of 0.5 ± 0.1 OD and 1.0 ± 0.1 OD per milliliter of water during the test. In a typical sensing experiment, the corresponding metal ions were spiked in water. Then, CTAB-AgNS, CTAB-AuNS, CTAB-AuNR1, and CTAB-AuNR2 were dispersed and examined regarding colorimetric/spectrophotometric changes. CTAB-AgNS, CTAB-AuNS, CTAB-AuNR1, and CTAB-AuNR2 were used with aliquots of NaOH (1 M) in a volume range of 5–50 μL. The pH of a sample was not measured because a volume of 5 μL NaOH already yielded pH 12. Consequently, we chose the volume of NaOH as a parameter instead of the pH value.

Catalytic degradation of 4-nitrophenol

The catalytic activity of CTAB-AgNS, CTAB-AuNS, CTAB-AuNR1, and CTAB-AuNR2 was determined by reducing 4-nitrophenol (4-NP) to 4-aminophenol (4-AP) in the presence of $NaBH_4$. All reactions were carried out at room temperature in a 3.5 mL quartz cuvette. The reagent for catalysis was added in a sequence of 2 mL of 4-nitrophenol (0.1 mM), 1 mL of $NaBH_4$ (100 mM), and 50 μL (0.5 ± 0.1 OD and 1.0 ± 0.1 OD) of CTAB-AgNS, CTAB-AuNS, CTAB-AuNR1, and CTAB-AuNR2, centrifuged and as-prepared, respectively. The catalytic conversion of 4-NP to 4-AP was measured using a UV–vis spectrophotometer at 300–900 nm. The disappearance of the color upon adding nanoparticles was measured and further, the change in the plasmon band was recorded. As controls, we chose bare nanospheres of gold/silver and compared them to the CTAB-capped metal nanoparticles [31].

Results and Discussion

Figure 1a shows the synthesis of isotropic and anisotropic metal nanoparticles using CTAB as surfactant. Silver and gold nanospheres, along with nanorods of different lengths were synthesized using wet chemical reduction, as shown in Figure 1a. A unique feature of CTAB is its robust and selective binding to certain crystal facets of metal surfaces that define the growth and nucleation of nanoparticles. CTAB on metal surfaces plays a key role in nanoparticle stabilization but hinders many applications, which in some instances require an external linker or ligand for usable applications. It was reported that for CTAB-capped nanoparticles to enable sensing, the use of a linker on CTAB was mandatory for heavy metal ion detection. Linker-free detection of heavy metals using CTAB is a challenge and
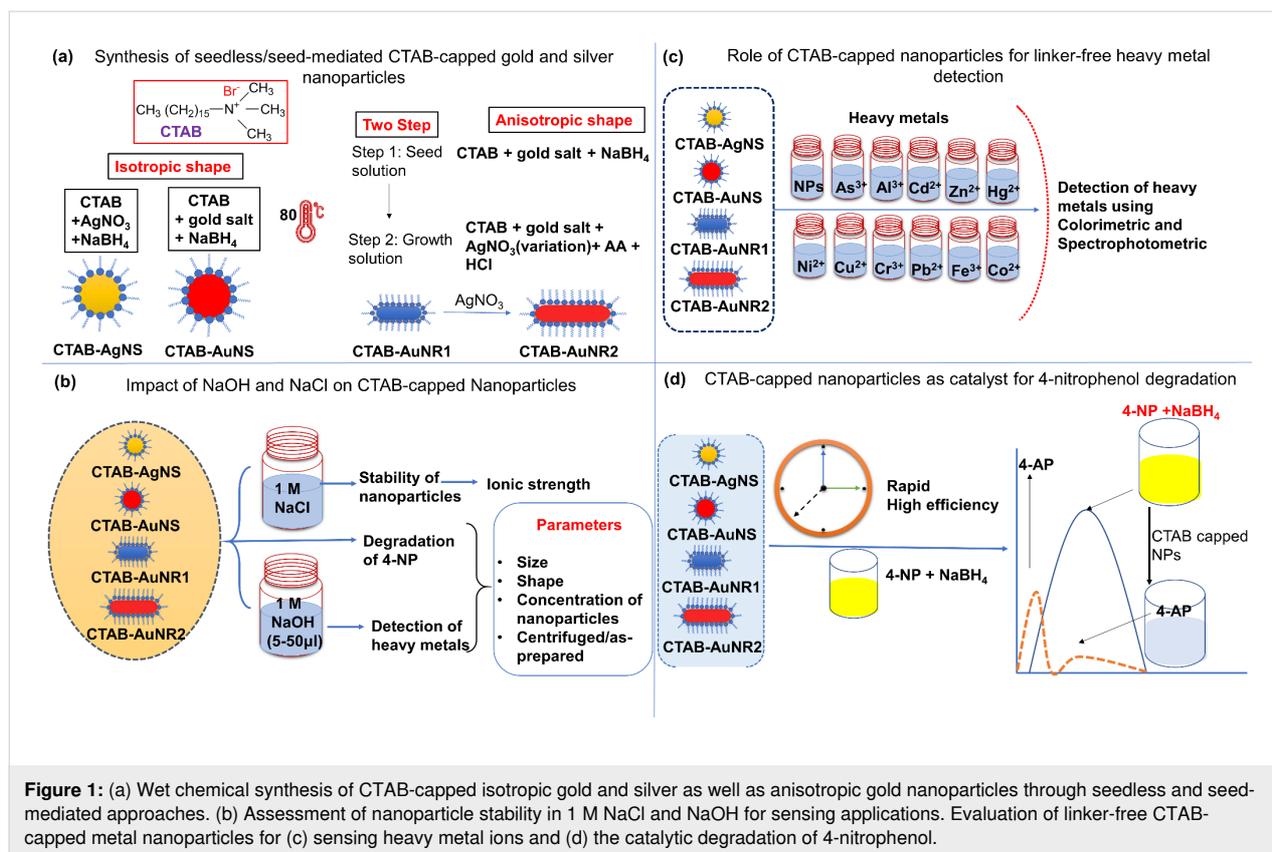
Figure 1: (a) Wet chemical synthesis of CTAB-capped isotropic gold and silver as well as anisotropic gold nanoparticles through seedless and seed-mediated approaches. (b) Assessment of nanoparticle stability in 1 M NaCl and NaOH for sensing applications. Evaluation of linker-free CTAB-capped metal nanoparticles for (c) sensing heavy metal ions and (d) the catalytic degradation of 4-nitrophenol.

pre-requisite for enabling faster and facile approaches. In this work, we designed several strategies involving the desorption of CTAB from the metal surface in the presence of solvents such as NaOH, which can tune the amount of CTAB on the surface. A recent study showed that sodium borohydride removed CTAB from metal surfaces for ligand exchange, which helped in the detection of heavy metal ions [32]. The impact of NaOH and NaCl was assessed regarding the stability of the synthesized metal nanoparticles at extreme concentrations (Figure 1b). The addition of 1 M NaOH at various volumes (5–50 μL) results in the controlled desorption of CTAB from the metal surface. A recent study demonstrated the ability of NaOH to interfere with CTAB micelles, where the pH value played a key role [33]. Optimized conditions enabled the linker-free sensing of heavy metal ions (Figure 1c). Nanoparticles dispersed in DD water were chosen as control (represented as NPs in Figure 1c). Additionally, CTAB-capped gold and silver nanoparticles have been reported for their enhanced catalytic activity. The simplest and fastest method for degradation or catalytic conversion of 4-nitrophenol is using a strong reducing agent (such as $NaBH_4$) in the presence of a catalytic agent (i.e., the nanoparticles) [27]. In the current study, we also examined the catalytic properties of CTAB-capped nanoparticles in the degradation of 4-nitrophenol (Figure 1d). The catalytic properties of CTAB-capped nanoparticles highly depend on various factors, including size,
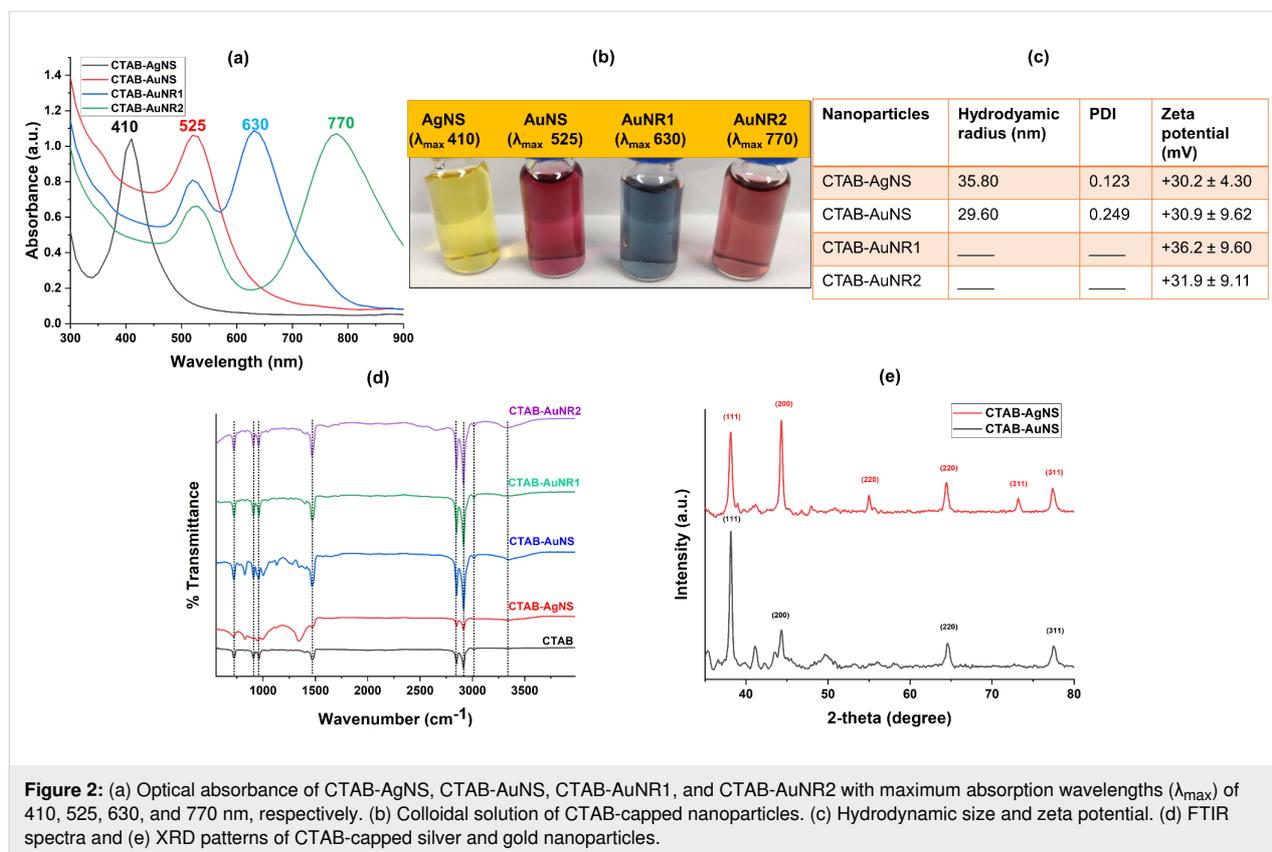
shape, and reaction parameters [34]. However, there was a gap in the literature regarding which factor is most crucial to the efficient degradation of 4-nitrophenol using nanoparticles. Some studies suggest size is essential, while others suggest pH, surface capping, and linker molecules are required to degrade 4-nitrophenol. Therefore, this study analyzed the impact of size, shape, metal type, and nanoparticle concentration on converting 4-nitrophenol to 4-aminophenol.

Characterization of CTAB-capped nanoparticles
UV–vis, DLS, Zeta, FTIR, XRD, and TEM analyses
Physicochemical characterization was performed using optical spectroscopy, DLS, FTIR, XRD, and TEM analyses. Figure 2a shows the synthesized isotropic silver and gold nanospheres with plasmon bands at 410 nm (AgNS) and 525 nm (AuNS). The anisotropic tunable gold nanorods with longitudinal plasmon bands at 630 nm (AuNR1) and 770 nm (AuNR2) indicate the formation of different lengths of nanorods.

The colloidal solutions of the metal nanoparticles having different sizes and shapes resulted in different colors (Figure 2b), a characteristic feature of gold and silver nanoparticles involving the change in surface plasmon resonance of the metal nanostructures. A single absorbance peak correlates to the symmetri-

Figure 2: (a) Optical absorbance of CTAB-AgNS, CTAB-AuNS, CTAB-AuNR1, and CTAB-AuNR2 with maximum absorption wavelengths (λ_{max}) of 410, 525, 630, and 770 nm, respectively. (b) Colloidal solution of CTAB-capped nanoparticles. (c) Hydrodynamic size and zeta potential. (d) FTIR spectra and (e) XRD patterns of CTAB-capped silver and gold nanoparticles.

cal shape and collective oscillation of free electrons on the nanoparticle surface. This phenomenon is known as localized surface plasmon resonance (LSPR), a characteristic feature of metallic nanoparticles such as gold and silver [35]. The length of the gold nanorods influences the LSPR [36]. The CTAB molecules on the shorter gold nanorods (20.8 ± 9.5 nm) are densely packed compared to longer nanorods (36.5 ± 7.3 nm). The high curvature of the nanorods leads to enhanced stabilization due to the larger inter-micellar channels generated on the flat side facets of the gold nanorods [37]. In comparison, the CTAB molecules on the longer nanorods are scattered over the side faces of the nanorods, which may lead to aggregation. Changes in pH or ionic strength are also capable of decreasing the CTAB binding to surfaces of longer gold nanorods. Therefore, longer nanorods are more prone to aggregation than shorter rods. The packing density of CTAB is also reported to be a factor that controls the size of metal nanoparticles [38]. The isotropic gold nanospheres exhibit an equal distribution of CTAB on the surfaces due to the isotropic geometry. The amount of CTAB is critical in determining the functional aspects of the metal nanospheres or nanorods.

Hydrodynamic radius, polydispersity, and surface charge of the synthesized CTAB-capped nanoparticles were measured as shown in Figure 2c. The DLS measurement indicated average

hydrodynamic radii of 35.80 and 29.60 nm for isotropic silver and gold nanospheres, respectively. DLS measurements of anisotropic nanorods (AuNR1 and AuNR2) could not be carried out because of limitations of the instrument [39]. The nanospheres of silver and gold showed good PDI values of 0.123 and 0.249 for silver and gold nanospheres, respectively (Figure 2c). The very low PDIs prove that the nanospheres are monodisperse and non-aggregated. A PDI of less than 0.3 typically indicates a relatively narrow and well-controlled size distribution [40]. CTAB forms a monolayer around the nanoparticles, providing a consistent and uniform surface coverage. This uniformity in surface passivation contributes to the narrow size distribution of the particles. The long hydrocarbon tails of the CTAB molecules extending from the nanoparticle surface create steric repulsive forces between the particles. This repulsion prevents particles from getting too close to each other, thus minimizing aggregation.

The CTAB-capped AgNS, AuNS, AuNR1, and AuNR2 showed positive zeta potential values of 30.2 ± 4.3, 30.9 ± 9.6, 36.2 ± 9.6, and 31.9 ± 9.1 mV, respectively (Figure 2c). Zeta potential values beyond −30 mV and +30 mV indicate excellent colloidal stability due to strong repulsive forces among the nanoparticles [41]. The positive zeta potential values are caused by the having positively charged head groups of CTAB mole-

cules, which are attracted to the negatively charged surfaces of the metal nanoparticles and form a cationic layer around them [28].

CTAB-AgNS, CTAB-AuNS, CTAB-AuNR1, and CTAB-AuNR2 were analyzed for functional group identification using FTIR (Figure 2d). CTAB contains a long alkyl chain that typically results in peaks at 2920 and 2850 cm^{-1} in the FTIR spectrum. These peaks correspond to the symmetric and antisymmetric stretching vibrations of alkyl C–H bonds [28]. CTAB-capped gold and silver nanoparticles exhibit peaks at the same wavenumber as the parent compound, but with different intensities (Figure 2d). The doublet at 1462 and 1472 cm^{-1} obtained from CTAB is attributed to the CH$_2$ scissoring mode and indicates close-packing of the methylene chains [42]. However, for CTAB-AgNS, CTAB-AuNS, CTAB-AuNR1, and CTAB-AuNR2, the peak splits into two parts with different intensities because of crystallinity loss in the hydrocarbon regions or the morphology of the nanoparticles. The singlets at 962 cm^{-1} for parent CTAB and 946 cm^{-1} for CTAB-AgNS correspond to C–N$^+$ stretching bands, and the shift in wavenumber might be due to the interaction between the N-containing amino group and the silver metal surface [28]. However, the peak did not shift in the case of gold nanoparticles (AuNS, AuNR1, and AuNR2). The characteristic [C–H–Ag] vibration was missing, indicating the absence of C–H binding to the metal surface. The new minor peaks of CTAB-capped AgNS and AuNS at 828, 1004, and 1130 cm^{-1}, which are not present in parent CTAB molecules, are also considered as stretching of C–N$^+$ affected by the metal surface, as described by Nikoobakht and El-Sayed for CTAB-capped gold nanoparticles [43]. The singlet at

730 cm^{-1} for parent (powder) CTAB and CTAB-capped nanoparticles is due to CH$_2$ rocking. The broad band at 3390 cm^{-1} in parent CTAB corresponds to N–H stretching, which is shifted to 3315 cm^{-1} after binding to the gold and silver nanoparticles. The overlap between peaks of parent CTAB with those of CTAB-capped metal nanoparticles indicates the successful capping of the nanoparticle surface without compromising their structural property.

To determine the crystalline structure of the synthesized silver and gold nanoparticles, silver and gold nanospheres capped with CTAB were measured with XRD (Figure 2e). The most common crystal structure of gold and silver in nanoparticles is face-centered cubic (FCC). In the XRD pattern of FCC CTAB-AuNS, we observe major diffraction peaks at around 38.2°, 44.1°, 64.5°, and 77.4°, corresponding to the (111), (200), (220), and (311) planes, respectively [42]. In the case of CTAB-AgNS, we observe major peaks at 38.1°, 44.3°, 64.4°, and 77.5°, corresponding to the (111), (200), (220), and (311) planes [44]. However, we also observed two minor peaks at 55.04° and 73.14°, which correspond to the (220) and (311) planes; these were also observed in other studies with CTAB-capped silver nanoparticles [44]. These peaks might be related to the formation of AgO in the nanoparticles, which is reported elsewhere [44].

Transmission electron microscopy (TEM) enables precise nanoparticle size and shape measurements. TEM images show that AuNR1 and AuNR2 have a rod-like shape with different sizes, whereas AuNS and AgNS are spherical (Figure 3a–d). The mean sizes of CTAB-AgNS and CTAB-AuNS are 27.4 ± 4.6
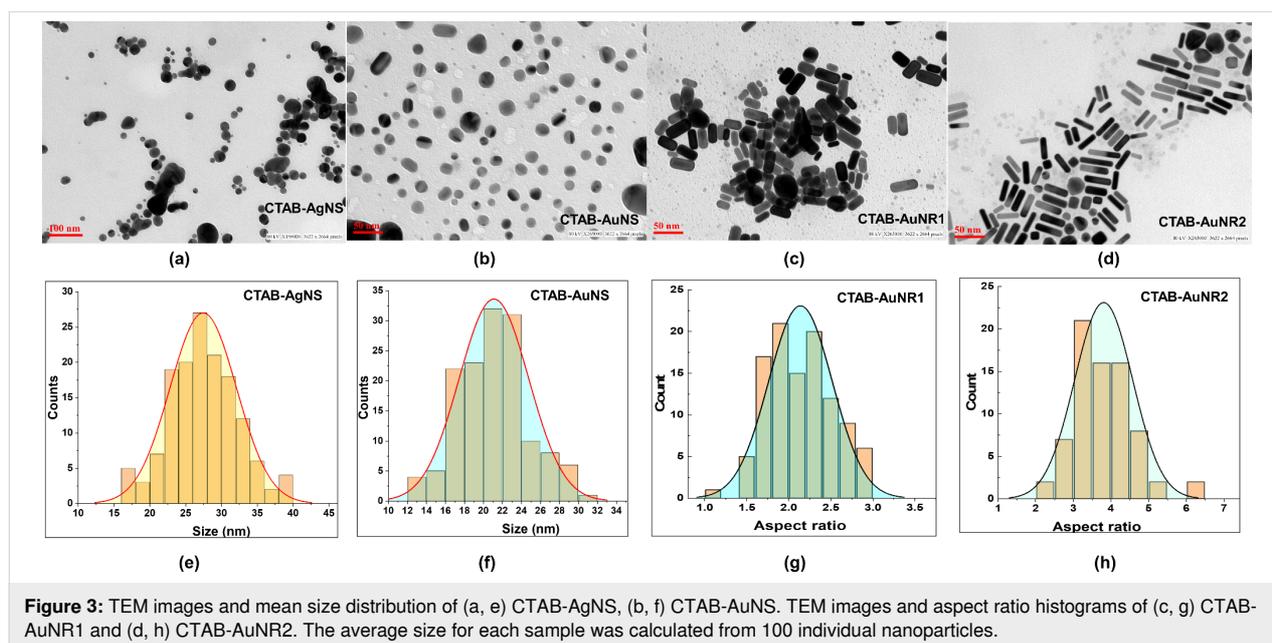
Figure 3: TEM images and mean size distribution of (a, e) CTAB-AgNS, (b, f) CTAB-AuNS. TEM images and aspect ratio histograms of (c, g) CTAB-AuNR1 and (d, h) CTAB-AuNR2. The average size for each sample was calculated from 100 individual nanoparticles.

and 21.1 ± 3.6 nm, respectively (Figure 3e and 3f). The mean average lengths of CTAB-AuNR1 and CTAB-AuNR2 were 20.76 ± 9.5 and 36.54 ± 7.3 nm, respectively. Also, there was a change in aspect ratio from 2.1 ± 0.3 to 3.8 ± 0.7 for AuNR1 and AuNR2, respectively (Figure 3g,h). Figure 3c and 3d show different sizes of nanorods for both AuNR1 and AuNR2 with 81.4% and 82.0% population, respectively. A total of 100 nanoparticles from each sample was considered for the measurements of average size.

Quantification of CTAB using UHPLC on nanoparticle surface

The quantity of CTAB on the nanoparticle surface was determined through an indirect approach wherein CTAB-capped metal nanoparticles underwent centrifugation, and the resulting supernatant was collected. The CTAB content in the supernatant was quantified using the developed UHPLC method. Subsequently, the remaining CTAB on the nanoparticles' surface was calculated by subtracting the collected CTAB amount from the initial quantity provided to the reaction mixture. In UHPLC, a peak at 208 nm, with a retention time of 0.8–0.9 min, was observed in the CTAB standard, utilizing a PDA detector within a linear range of 0.625–20 µg/mL. This standard was further applied to confirm and quantify CTAB in the nanoparticle supernatant (Supporting Information File 1, Figure S1). During sample analysis, a similar peak was consistently observed in all CTAB-capped nanoparticle supernatants, appropriately diluted within the linear range. The final concentrations of CTAB in CTAB-capped AgNS, AuNS, AuNR1, and AuNR2 were found to be 5612, 30400, 31020, and 30655 µg/mL. After centrifugation, the CTAB content in the obtained supernatant was 4756, 15940, 17200, and 18340 µg/mL, as indicated in Table 1. Consequently, the CTAB remaining on CTAB-AgNS, CTAB-AuNS, CTAB-AuNR1, and CTAB-AuNR2 surfaces was determined to be 856.30, 14460, 13820, and 12315 µg/mL, respectively. Gold nanoparticles exhibit a higher amount of bound CTAB than silver nanoparticles.

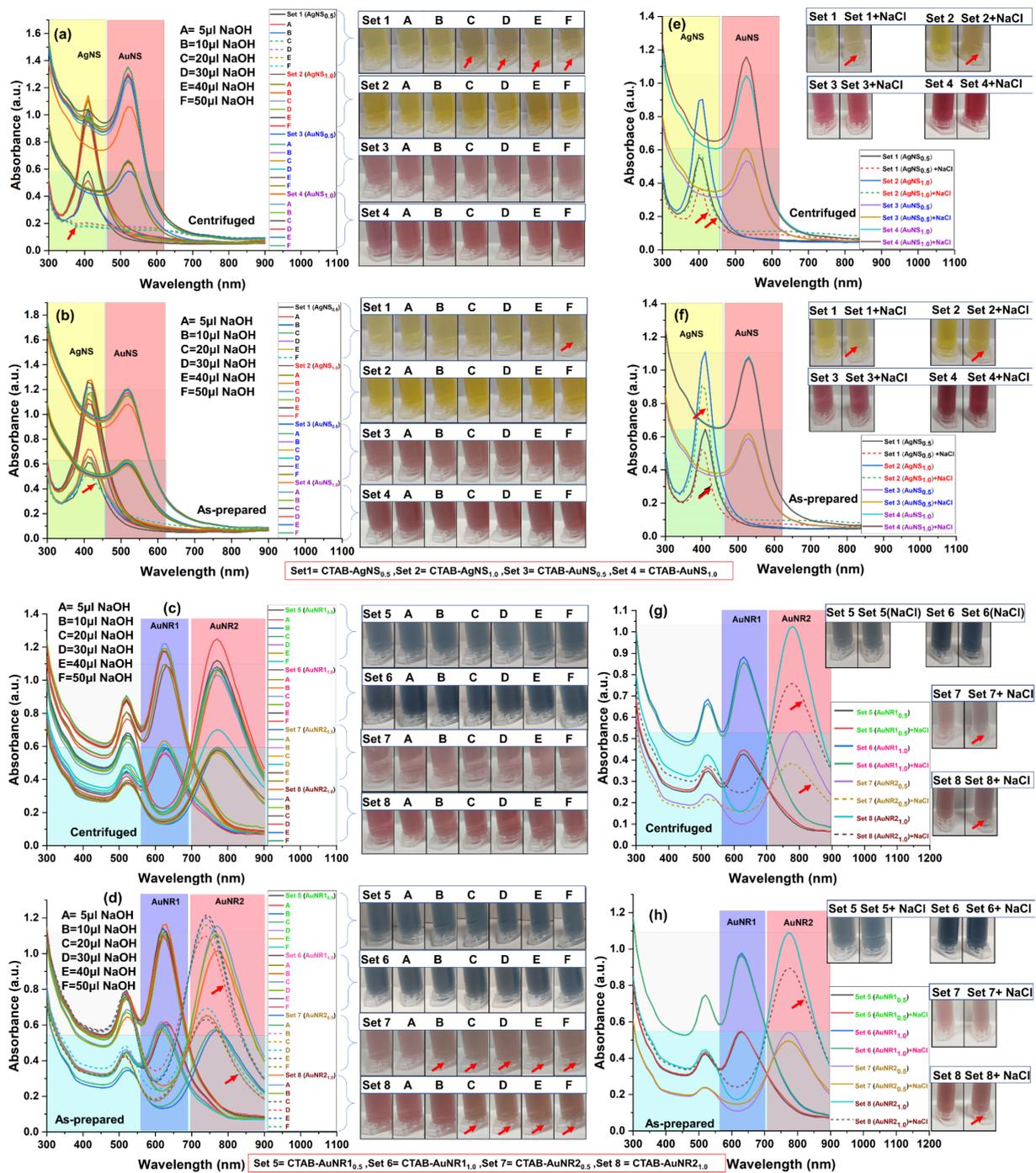## Impact of NaCl and NaOH on CTAB-capped nanoparticles

The stability and dispersibility of the CTAB-capped metal nanoparticles were assessed in 1 M NaOH and NaCl. NaOH or NaCl may lead to the desorption of CTAB from the metal surface, which plays a key role in detecting heavy metal ions. The addition of various volumes of NaOH to the metal nanoparticles of different concentrations (OD of 0.5 ± 0.1 and 1.0 ± 0.1) resulted in both colorimetric and spectrophotometric detection of heavy metal ions. The different sets 1–8 represent CTAB-AgNS, CTAB-AuNS, CTAB-AuNR1 and CTAB-AuNR2, each with 0.5 ± 0.1 and 1.0 ± 0.1 OD. As-prepared and centrifuged nanoparticles were tested to assess their stability in NaOH (5–50 µL) and NaCl. Centrifuged CTAB-AgNS$_{0.5}$ (set 1) shows NaOH volume-dependent aggregation of the silver nanospheres (Figure 4a). The peak flattening of centrifuged AgNS$_{0.5}$ from 20 µL NaOH (set 1, C–F) onward confirmed nanoparticle aggregation, leading to colorimetric differences compared to the control (Figure 4a).

In contrast, centrifuged AgNS$_{1.0}$ (set 2) was highly stable in NaOH up to 50 µL (A–F) compared to AgNS$_{0.5}$ (Figure 4a). This stability is attributed to the increased nanoparticle concentration and the amount of CTAB. A similar trend was observed in the case of as-prepared AgNS$_{0.5}$ (set 1) and AgNS$_{1.0}$ (set 2) (Figure 4b). However, the intensity of as-prepared AgNS$_{0.5}$ decreases with 50 µL NaOH, evident by a color change (Figure 4b). The stability of centrifuged and as-prepared AgNS$_{1.0}$ give a clear indication that nanoparticles with higher concentrations are stable in NaOH, which is not observed in the case of centrifuged and as-prepared AgNS$_{0.5}$. In a study by Yadav et al., NaOH (0.1 N) induced a hyperchromic effect in silver nanoparticles, which was not observed in our case [45]. In our study, no plasmonic shift was observed, but a slight decrease in intensity at lower concentrations of silver nanoparticles might be due to the strong capping of CTAB on the nanoparticles' surface. Apart from nanoparticle concentration, the amount of the capping agent on the surface of nanoparticles plays a significant role in providing stability, as reported elsewhere [3]. The concentration of CTAB that remained on silver nanoparticles after centrifugation was significantly reduced (Table 1). However, the role of the capping agent is not limited to stability; it also enhances the application potential of nanoparticles in the presence of NaOH. Gold nanoparticles are highly stable compared to silver nanoparticles, as silver nanoparticles are prone to oxidation [46].

Table 1: Quantification of CTAB using the UHPLC method.

Sample	CTAB added (µg/mL)	CTAB obtained (µg/mL)	CTAB bound on nanoparticles (µg/mL)	Binding efficiency (%)
CTAB-AgNS	5612	4756 ± 34	856.30	15.25%
CTAB-AuNS	30400	15940 ± 124	14460	47.56%
CTAB-AuNR1	31020	17200 ± 100	13820	44.55%
CTAB-AuNR2	30655	18340 ± 61	12315	40.17%

Figure 4: Impact of NaOH and NaCl on as-prepared/centrifuged CTAB-capped nanoparticles. (a, b) NaOH impact on centrifuged and as-prepared isotropic CTAB-capped nanoparticles (AgNS$_{0.5}$, AgNS$_{1.0}$, AuNS$_{0.5}$, and AuNS$_{1.0}$). (c, d) NaOH impact on centrifuged and as-prepared anisotropic CTAB-capped nanoparticles (AuNR1$_{0.5}$, AuNR1$_{1.0}$, AuNR2$_{0.5}$ and AuNR2$_{1.0}$). (e, f) NaCl impact on centrifuged and as-prepared isotropic CTAB-capped nanoparticles (AgNS$_{0.5}$, AgNS$_{1.0}$, AuNS$_{0.5}$ and AuNS$_{1.0}$). (g, h) NaCl impact on centrifuged and as-prepared anisotropic CTAB-capped nanoparticles (AuNR1$_{0.5}$, AuNR1$_{1.0}$, AuNR2$_{0.5}$, and AuNR2$_{1.0}$). The images attached with spectral absorbance show the color change upon adding NaOH and NaCl. The subscripts 0.5 and 1.0 represent the nanoparticle concentration in OD. Sets 1–8 correspond to nanoparticles AgNS$_{0.5}$, AgNS$_{1.0}$, AuNS$_{0.5}$, AuNS$_{1.0}$, AuNR1$_{0.5}$, AuNR1$_{1.0}$, AuNR2$_{0.5}$, and AuNR2$_{1.0}$ respectively. A, B, C, D, E, and F mean NaOH volumes of 5, 10, 20, 30, 40, and 50 µL, respectively, added to the nanoparticles. The short dashed line shows the change in the sample compared to the control (marked by an arrow). The first centrifuge tube in each colorimetric panel represented as control for that panel.

Interestingly, the centrifuged/as-prepared CTAB-AuNS$_{0.5}$ (set 3) and AuNS$_{1.0}$ (set 4) showed no plasmonic change upon the addition of different volumes of NaOH (Figure 4a,b). Also, no significant difference in the color of AuNS was observed (Figure 4a,b). This might be because the amount of CTAB on the gold nanospheres is significantly higher than on silver nanoparticles in both centrifuged and as-prepared samples (Table 1). This suggests that the nature of the metal and the strong capping in nanoparticles are also crucial for their enhanced stability in NaOH. In addition, the shape-dependent impact of nanoparticle stability in NaOH was evaluated using gold nanorods (AuNRs) of two different lengths.

AuNR1$_{0.5}$ (set 5), AuNR1$_{1.0}$ (set 6), AuNR2$_{0.5}$ (set 7), and AuNR2$_{1.0}$ (set 8) showed no plasmonic and colorimetric changes in the presence of NaOH (Figure 4c). The as-prepared AuNR2$_{0.5}$ and AuNR2$_{1.0}$ showed a blueshift of plasmons along with a color change in the presence of more than 10 μL and 20 μL NaOH, respectively. In contrast, AuNR1 at both OD did not show any significant changes (Figure 4d). These results revealed that longer gold rods in the as-prepared state show a blueshift of plasmons due to the easy desorption of CTAB in the presence of NaOH, which is not observed in the case of small gold nanorods and nanospheres. The CTAB is tightly packed on short nanorods and nanospheres [43]. It was reported that NaOH significantly alters the micelles of quaternary ammonium surfactants [47]. This ultimately affects the capping ability of CTAB, thus providing a platform for interaction with the ligand. Furthermore, the nanoparticles designed for sensing applications should have higher ionic strength, which provides them the capability for heavy metal sensing in real scenarios. To determine the ionic strength of the synthesized nanoparticles, their stability in ionic salts, such as NaCl, must be evaluated. Centrifuged/as-prepared CTAB-AgNS$_{0.5}$ and AgNS$_{1.0}$ show a decrease in the plasmonic intensity of nanoparticles and a change in color in the presence of NaCl (Figure 4e,f). However, no flattening or aggregation of silver nanoparticles was noticed (Figure 4e,f). The decrease in the intensity of silver nanoparticles might be due to less CTAB on the nanoparticles' surface or a decrease in CTAB CMC value. As reported elsewhere, the reduction in CTAB CMC is associated with NaCl concentration [48]. Centrifuged and as-prepared AuNS$_{0.5}$ and AuNS$_{1.0}$ showed no absorbance or colorimetric change in the presence of NaCl (Figure 4e,f).

Similarly, centrifuged and as-prepared AuNR1s (AuNR1$_{0.5}$ and AuNR1$_{1.0}$) showed no changes in plasmon frequency or color of the nanoparticles in the presence of NaCl (Figure 4g,h). Although centrifuged and as-prepared AuNR2$_{0.5}$ and AuNR2$_{1.0}$ showed a noticeable difference in the absorption spectrum compared to the control (Figure 4g,h). Previously, several reports

confirmed the use of NaOH and NaCl in nanoparticle synthesis or surface modification for different applications. This experimental study demonstrated that CTAB-capped isotropic and anisotropic nanoparticles are stable in NaOH and NaCl and will be used for further sensing applications. In comparison with other studies, the synthesized nanoparticles are stable at higher concentrations of NaCl and NaOH. The colloidal stability of nanoparticles represents the initial step towards designing them as environmental heavy metal detection probes.

Detection of heavy metals
Isotropic CTAB-capped AgNS and AuNS
A range of heavy metals, specifically As^{3+}, Al^{3+}, Cd^{2+}, Zn^{2+}, Hg^{2+}, Ni^{2+}, Cu^{2+}, Cr^{3+}, Pb^{2+}, Fe^{3+}, and Co^{2+}, each with a concentration of 1 ppm, was examined. The isotropic CTAB-capped AgNS and AuNS were used to detect heavy metals without NaOH. Centrifuged CTAB-AgNS$_{0.5}$ detected Hg^{2+} and Fe^{3+} based on changes in color and spectral absorbance compared to the control (Figure 5a).

Surprisingly, no metal detection was observed with centrifuged AgNS$_{1.0}$ (Figure 5a). This might be due to the non-availability of binding sites for metals on the surface of silver nanoparticles, as CTAB is tightly bound to the isotropic nanoparticles as discussed earlier. However, as-prepared CTAB-AgNS$_{0.5}$ and AgNS$_{1.0}$ sensed Hg^{2+} and Cu^{2+} without NaOH (Figure 5b). The decrease in plasmonic intensity of as-prepared AgNS$_{0.5}$ and AgNS$_{1.0}$ in the presence of Hg^{2+} and Cu^{2+} leads to a colorimetric change (Figure 5b). This suggests the interaction of as-prepared CTAB-capped silver nanoparticles with Cu^{2+} and Hg^{2+}, regardless of their concentration. The capping provides metal selectivity, whereas bare AgNS$_{1.0}$ (without capping) showed unspecific metal detection such as Cd^{2+}, Zn^{2+}, Hg^{2+}, Ni^{2+}, Cu^{2+}, Cr^{3+}, Pb^{2+}, Fe^{3+}, and Co^{2+} (Figure 5d). However, in another study, only Hg^{2+} was detected with silver nanoparticles capped with poly(allylamine) hydrochloride but stabilized using CTAB [49]. Also, no prominent metal detection was achieved after adding NaOH to as-prepared CTAB-AgNS$_{0.5}$ and AgNS$_{1.0}$, confirming no interaction between metal and nanoparticles (Supporting Information File 1, Figure S2 and Figure S3). The as-prepared CTAB-AgNS contains 5612 μg/mL CTAB, which changes in the case of centrifuged CTAB-AgNS to 856 μg/mL. Despite less CTAB on the silver nanoparticle surface, they showed excellent sensing capability even at lower nanoparticle concentration. The addition of NaOH (5–50 μL) to centrifuged CTAB-AgNS led to no selectivity toward metal detection with centrifuged AgNS$_{1.0}$, while aggregation of the particles was observed for AgNS$_{0.5}$ starting from 20 μL of NaOH (Figure S4 and Figure S5, Supporting Information File 1). These results reveal that the as-prepared CTAB AgNS$_{0.5}$ and AgNS$_{1.0}$ and centrifuged AgNS$_{0.5}$ selec-
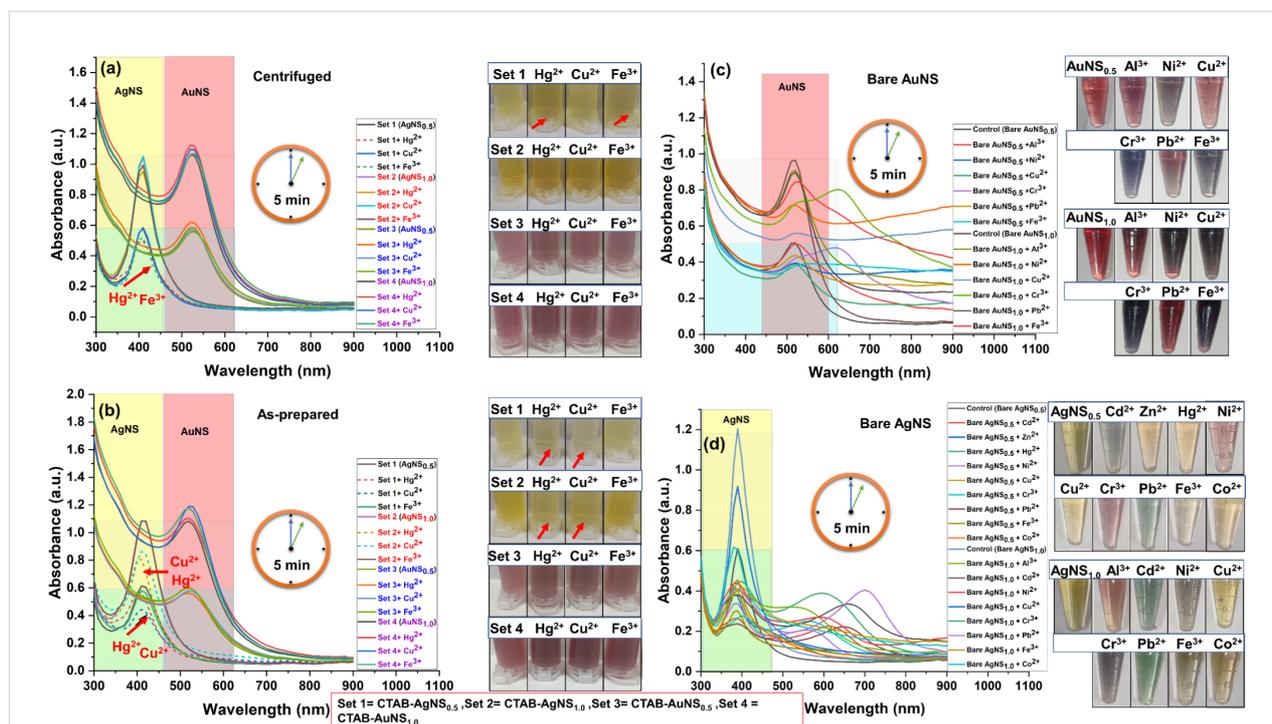
Figure 5: Spectrophotometric and colorimetric detection of heavy metals using centrifuged/as-prepared isotropic metal nanoparticles in the absence of NaOH. (a) Detection of Hg^{2+} and Fe^{3+} using centrifuged $AgNS_{0.5}$, while $AgNS_{1.0}$, $AuNS_{0.5}$, and $AuNS_{1.0}$ did not detect the metals. (b) Detection of Hg^{2+} and Cu^{2+} using as-prepared $AgNS_{0.5}$ and $AgNS_{1.0}$, while $AuNS_{0.5}$, and $AuNS_{1.0}$ did not detect the metals. (c) Detection of Al^{3+}, Ni^{2+}, Cu^{2+}, Cr^{3+}, Pb^{2+}, and Fe^{3+} using bare AuNS. (d) Detection of Al^{3+}, Cd^{2+}, Zn^{2+}, Hg^{2+}, Ni^{2+}, Cu^{2+}, Cr^{3+}, Pb^{2+}, Fe^{3+}, and Co^{2+} using silver nanospheres ($AgNS_{0.5}$ and $AgNS_{1.0}$). The subscripts 0.5 and 1.0 represent the nanoparticles concentration in terms of optical density. Sets 1–4 correspond to nanoparticles $AgNS_{0.5}$, $AgNS_{1.0}$, $AuNS_{0.5}$, and $AuNS_{1.0}$ respectively. The short dashed line shows the change in the sample compared to the control (marked by an arrow). The first centrifuge tube in each colorimetric panel represented as control for that panel.

tively detect heavy metals in the absence of NaOH, while centrifuged $AgNS_{1.0}$ showed interaction with multiple metals because of more particles with less CTAB than as-prepared particles. The bare/uncapped $AgNS_{0.5}$ and $AgNS_{1.0}$ detected various metals (Figure S10, Supporting Information File 1).

Gold nanoparticles with similar capping and size were considered to determine the role of surface capping in heavy metal detection. Interestingly, as-prepared and centrifuged CTAB-$AuNS_{0.5}$ and $AuNS_{1.0}$ showed no interaction with heavy metals without NaOH (Figure 5a,b). No metal ions were detected with as-prepared/centrifuged $AuNS_{0.5}$ and $AuNS_{1.0}$ in the absence and presence of NaOH (Figures S6–S9, Supporting Information File 1). However, bare AuNS detected various metals including Al^{3+}, Ni^{2+}, Cu^{2+}, Cr^{3+}, Pb^{2+}, and Fe^{3+} (Figure 4c and Figure S10, Supporting Information File 1). The concentrations of CTAB in as-prepared and centrifuged AuNS are 30400 and 14460 µg/mL, respectively, which is far more than in silver nanoparticles. Silver nanoparticles interact with other metals because of their strong redox potential and the lower amount of CTAB [9]. The nanoparticle shape is also a criterion for designing nanoparticles as sensing probes. Therefore, we also

assessed the potential of CTAB-capped gold nanorods (AuNR) as sensing probes for detecting heavy metals.

Anisotropic CTAB-capped gold nanorods

CTAB-$AuNR1_{0.5}$ interacted with three metal ions, namely Ni^{2+}, Cr^{3+}, and Co^{2+}, as evident through spectrophotometric and colorimetric differences compared to the control in the presence of 5–10 µL NaOH (Figure 6a,b).

The interaction of $AuNR1_{0.5}$ with Hg^{2+} leads to a slight blueshift (no prominent color change), while redshifts were observed with other metals compared to the control (Supporting Information File 1, Figure S11). As discussed in previous sections, NaOH plays a significant role in decreasing the amount of CTAB on the nanoparticles, thus providing binding sites to the metal ions. The interaction with Hg^{2+} was also evident in as-prepared and centrifuged CTAB-AgNS. Placido et al. demonstrated Hg^{2+} detection using L-cysteine-functionalized CTAB-AuNR [50]. However, multiple metals were detected, including Hg^{2+}, without surface functionalization using NaOH (5–10 µL). After increasing the added amount of NaOH to 20–50 µL, centrifuged $AuNR1_{0.5}$ selectively inter-
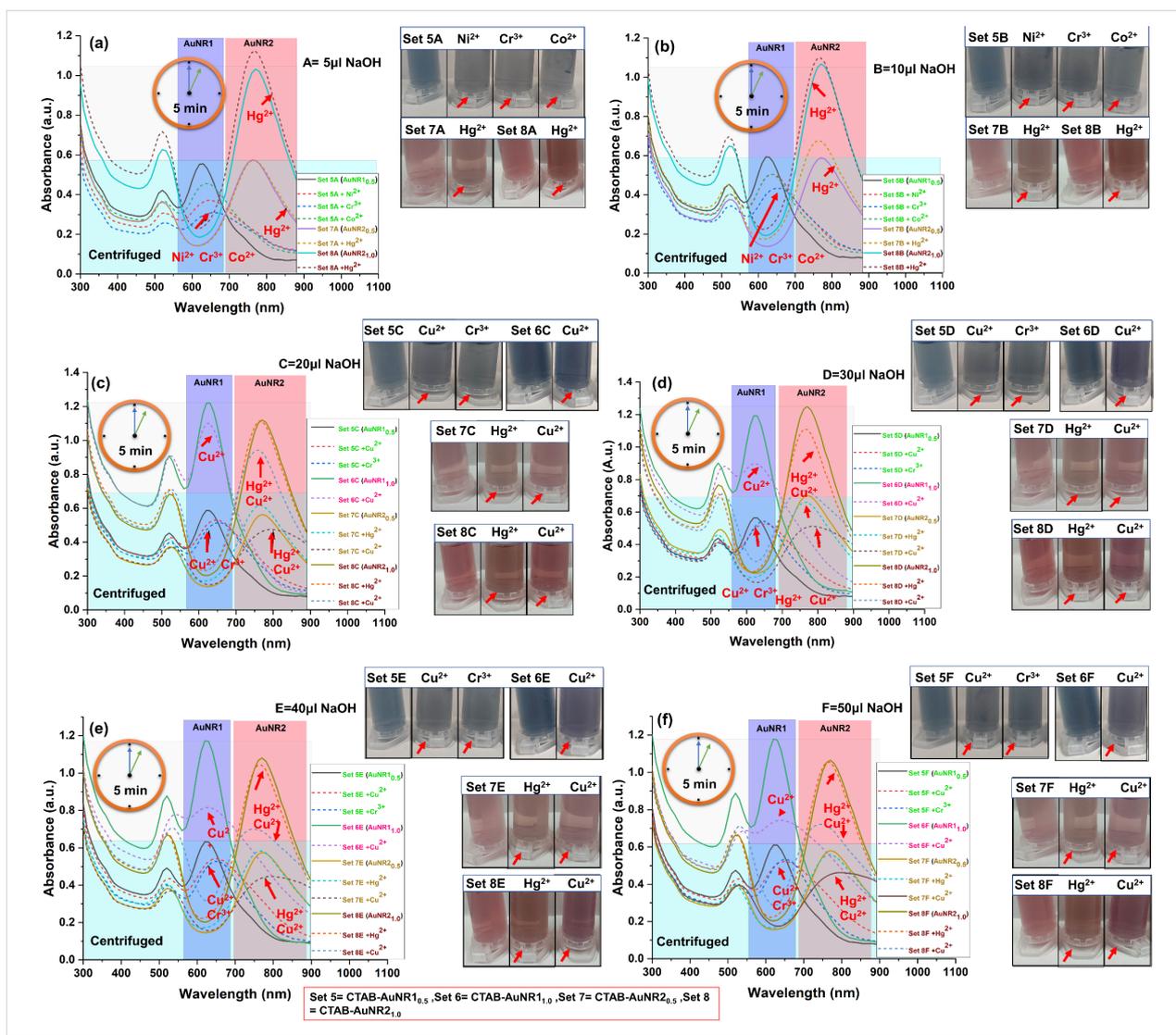
Figure 6: Spectrophotometric and colorimetric detection of heavy metals using centrifuged CTAB-AuNR1 and AuNR2 in the presence of NaOH. (a) AuNR1$_{0.5}$ (set 5) and AuNR2$_{0.5/1.0}$ (set 7 and set 8) detect Ni^{2+}, Cr^{3+} and Co^{2+}, and Hg^{2+} in the presence of 5 μL NaOH (A). (b) AuNR1$_{0.5}$ (set 5) and AuNR2$_{0.5/1.0}$ (set 7 and set 8) detect Ni^{2+}, Cr^{3+} and Co^{2+}, and Hg^{2+} in the presence of 5 μL NaOH (B); (c–f) AuNR1$_{0.5/1.0}$ (set 5 and set 6) and AuNR2$_{0.5/1.0}$ (set 7 and set 8) detect Cu^{2+}, Cr^{3+}, and Hg^{2+} in the presence of 20, 30, 40, and 50 μL of NaOH (C–F). The subscripts 0.5 and 1.0 represent the nanoparticle concentration in terms of optical density. Sets 5–8 correspond to nanoparticles AuNR1$_{0.5}$, AuNR1$_{1.0}$, AuNR2$_{0.5}$ and AuNR2$_{1.0}$, respectively. A, B, C, D, E, and F mean added NaOH volumes of 5, 10, 20, 30, 40, and 50 μL, respectively. The short-dashed line shows the change in the sample compared to the control (marked by an arrow). The first centrifuge tube in each colorimetric panel represented as control for that panel.

acted with Cu^{2+} and Cr^{3+} with prominent color and spectral changes (Figure 6c–f). The metal selectivity switched upon increasing the volume of NaOH, confirming the significant role of NaOH in designing the nanoparticle-based sensor. Selective metal detection using centrifuged AuNR1$_{0.5}$ was achieved among all metals in the presence of NaOH only (Supporting Information File 1, Figure S11). Centrifuged CTAB-AuNR1$_{0.5}$ without NaOH showed no metal detection (Supporting Information File 1, Figure S11). Apart from the amount of added NaOH, the nanoparticle concentration in terms of OD also plays a significant role in the nanoparticle–metal interactions. Increasing the nanoparticle concentration, centrifuged AuNR1$_{1.0}$

detected only copper (Cu^{2+}) upon adding NaOH (30–50 μL) to the nanoparticles of 1 OD (Figure 6d–f). The colorimetric changes could be observed by the naked eye (Figure 6d–f). There were no visual differences in the centrifuged AuNR1$_{1.0}$ plasmonic absorbance in the absence and presence of NaOH (5–20 μL) (Supporting Information File 1, Figure S12). Color or plasmon band changes can be attributed to nanoparticle–metal interactions [51]. Other researchers also explored the role of NaOH; they found that NaOH is a potent molecule that helps to remove CTAB from nanoparticles by reducing the CMC [33]. Indeed, the lower nanoparticle concentration (0.5 OD) provides high interaction due to the availability of
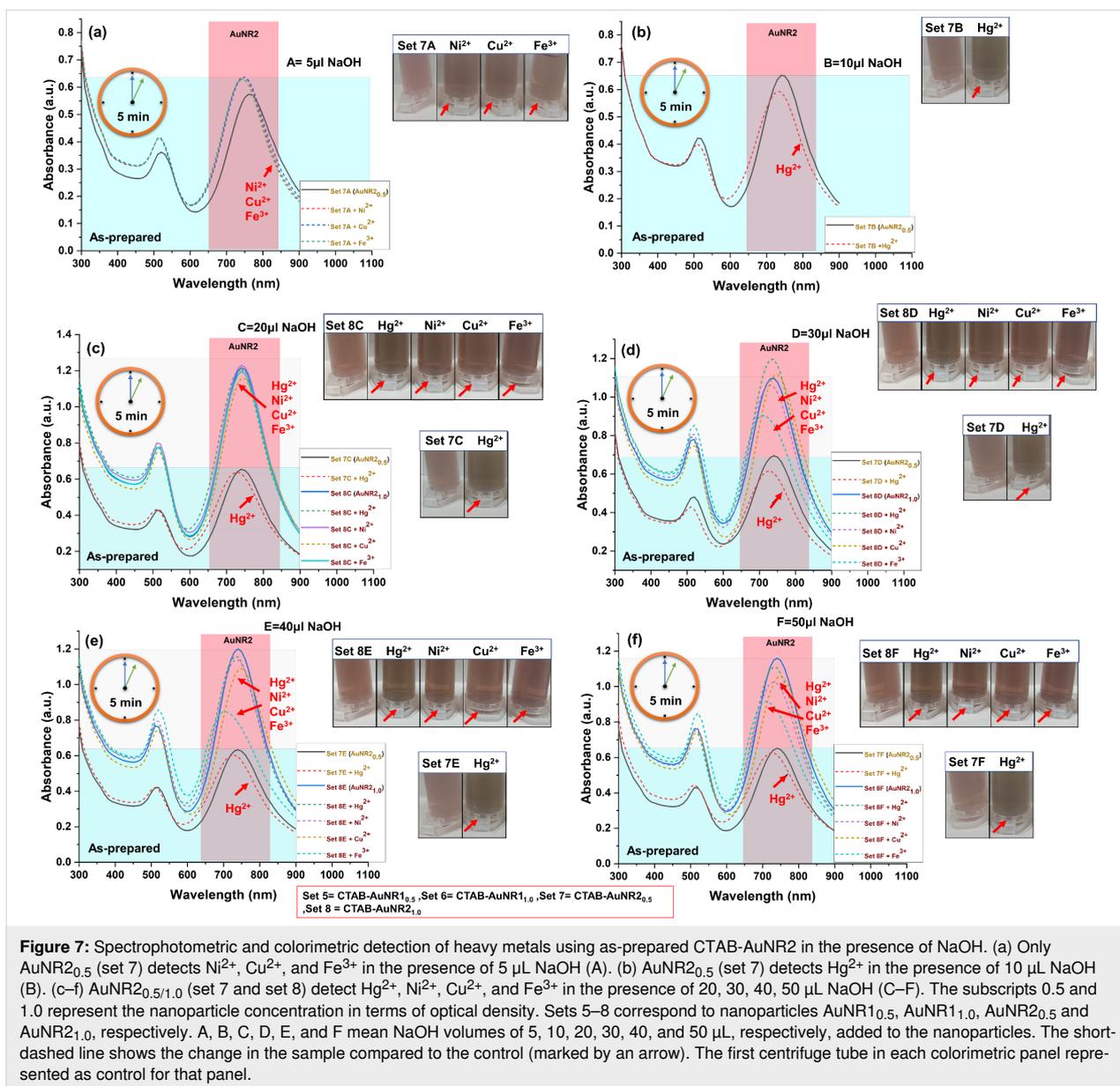
fewer particles and less amount of CTAB on their surface compared to 1 OD with the same metal concentration (1 ppm). The concentrations of CTAB in as-prepared and centrifuged AuNR1 are 31020 and 13820 µg/mL, respectively. Thus, nanoparticle concentration also played a significant role in designing the detection system for heavy metals.

Centrifuged CTAB-AuNR2$_{0.5}$ and AuNR2$_{1.0}$ spectrophotometrically detected Hg^{2+} with 5–10 µL NaOH (Figure 6a,b). The results obtained with centrifuged CTAB-AuNR2$_{0.5}$ and AuNR2$_{1.0}$ were nearly the same as for centrifuged CTAB-AuNR1$_{0.5}$ with Hg^{2+}. However, in the case of centrifuged CTAB-AuNR2$_{0.5}$, Hg^{2+} shows a prominent color change compared to centrifuged AuNR1$_{0.5}$. The detection of Hg^{2+} is also obtained with centrifuged CTAB-AgNS$_{0.5}$, but centrifuged CTAB-AuNS$_{0.5}$ did not detect any metal ions. A subtle change in capping concentration on AuNR1 and AuNR2 was observed due to their length (Table 1). The change in concentration or size of nanorods ultimately affects the sensitivity towards metal ion detection. The metal selectivity was observed for all metal ions (Supporting Information File 1, Figure S13). With increasing nanoparticle concentration, centrifuged CTAB-AuNR2$_{1.0}$ and AuNR2$_{0.5}$ detected Hg^{2+} and Cu^{2+} with 20–50 µL NaOH (Figure 6c–f). The metal selectivity was changed upon increasing the NaOH volume and concentration of nanoparticles, as also observed for the shorter nanorods. The mechanism is similar to the interaction of metals with longer nanorods. However, the change in metal selectivity is due to the size of nanorods. In NaOH absence, no metal shows prominent interaction with centrifuged CTAB-AuNR2$_{1.0}$ and AuNR2$_{0.5}$ (Supporting Information File 1, Figure S13 and Figure S14). The absence of NaOH and no metal detection indicate a strong binding of CTAB on the nanoparticles' surface. Therefore, it is certain that a minimum amount of NaOH is required to weaken the binding of CTAB without hampering the nanoparticles' sensing abilities. Furthermore, the higher CTAB concentration in as-prepared samples was also evaluated to confirm metal selectivity. The concentrations of CTAB in as-prepared and centrifuged CTAB-AuNR2 are 30655 and 12315 µg/mL, respectively; the longer nanorods have a lower amount of bound CTAB. However, in the case of as-prepared samples, nearly the same amount of CTAB is present.

In addition to this, the as-prepared CTAB-AuNR1 and CTAB-AuNR2 were also evaluated regarding heavy metal detection. Although the nanoparticle concentration has a big impact, washing nanoparticles is crucial in detecting heavy metals. As-prepared nanoparticles of the same concentration and size were evaluated to understand the impact of washing. As-prepared AuNR1 at 0.5 and 1 OD did not detect any metal through significant changes in color or plasmon resonance (Supporting

Information File 1, Figure S15 and Figure S16). However, a slight blueshift of as-prepared CTAB-AuNR1$_{0.5}$ was observed with Hg^{2+} only in the presence of various amounts (10–50 µL) of NaOH (Supporting Information File 1, Figure S15). This is evident by the blueshift of the plasmonic peak by 10 nm compared to the control samples. However, no prominent color change was observed (Supporting Information File 1, Figure S15). This is due to the excess CTAB on as-prepared AuNR1, which does not allow for interaction with metals. Only Hg^{2+} showed interaction, as observed in CTAB-AgNS, where the concentration of CTAB is much lower than in CTAB-AuNR1. Similarly, no heavy metal interaction is possible in the case of CTAB-AuNS due to tightly bound CTAB. However, in the case of CTAB-AuNR1, CTAB is tightly bound to the flat side and show an intermicellar gap at the curvature. The curvature allows for metal interaction only after adding a specific amount of NaOH. The nanoparticles (as-prepared AuNR1$_{0.5}$ and AuNR1$_{1.0}$) without NaOH showed no metal detection (Supporting Information File 1, Figure S15 and Figure S16). The robust nature of CTAB on nanoparticle surfaces is well known, thus resisting the interaction with target molecules without surface modification. In our case, NaOH was used to weaken CTAB micelles without hampering the physicochemical properties of the synthesized nanoparticles. This weakening of CTAB solves the persistent problem of surface modification or the use of linker molecules with CTAB-capped nanoparticles for sensing applications. In addition, the nanorod size might be crucial regarding nanorod–metal interactions. In a previous study conducted by Xu et al., Cu^{2+} was detected with cysteine-functionalized CTAB-AuNR (λ_{max} 800 nm), while Hg^{2+} was detected with cysteine-functionalized CTAB-AuNR (λ_{max} 650 nm) [50,52]. Both L-cysteine-functionalized CTAB-AuNR detected different metals. Thus, it was confirmed that the size of the nanoparticles is a critical parameter influencing the physical and chemical properties of gold nanoparticles. The current study also evaluated size-dependent metal sensing using longer gold nanorods with the help of NaOH. Upon the addition of a specific volume of NaOH, the absorption band of CTAB-AuNR2 was blueshifted (λ_{max} 770 ± 5 nm to 740 ± 5 nm). The shifted peak of CTAB-AuNR2 was used as a control for further heavy metal sensing experiments because no aggregation was observed. As-prepared CTAB-AuNR2$_{0.5}$ interacted only with Hg^{2+} with a prominent blueshift of the plasmonic peak after addition of 10–50 µL of NaOH (Figure 7b–f). The present study demonstrated that merely altering the parameters of nanorods is sufficient for the detection of heavy metals, eliminating the need for any additional linker or buffer.

As-prepared AuNR2$_{0.5}$ interacted with Ni^{2+}, Cu^{2+}, and Fe^{3+} metal ions in the presence of 5 µL NaOH (Figure 7a). However, no significant change in nanoparticles was observed in the

Figure 7: Spectrophotometric and colorimetric detection of heavy metals using as-prepared CTAB-AuNR2 in the presence of NaOH. (a) Only AuNR2$_{0.5}$ (set 7) detects Ni^{2+}, Cu^{2+}, and Fe^{3+} in the presence of 5 μL NaOH (A). (b) AuNR2$_{0.5}$ (set 7) detects Hg^{2+} in the presence of 10 μL NaOH (B). (c–f) AuNR2$_{0.5/1.0}$ (set 7 and set 8) detect Hg^{2+}, Ni^{2+}, Cu^{2+}, and Fe^{3+} in the presence of 20, 30, 40, 50 μL NaOH (C–F). The subscripts 0.5 and 1.0 represent the nanoparticle concentration in terms of optical density. Sets 5–8 correspond to nanoparticles AuNR1$_{0.5}$, AuNR1$_{1.0}$, AuNR2$_{0.5}$ and AuNR2$_{1.0}$, respectively. A, B, C, D, E, and F mean NaOH volumes of 5, 10, 20, 30, 40, and 50 μL, respectively, added to the nanoparticles. The short-dashed line shows the change in the sample compared to the control (marked by an arrow). The first centrifuge tube in each colorimetric panel represented as control for that panel.

absence of NaOH compared to the control (Supporting Information File 1, Figure S17). As-prepared CTAB-AuNR2$_{1.0}$ showed interaction with Hg^{2+}, Ni^{2+}, Cu^{2+}, and Fe^{3+} in the presence of 20–50 μL of NaOH with a prominent blueshift of the absorption band (Figure 7c–f). The metal selectivity changed in the case of as-prepared CTAB-AuNR2$_{1.0}$ compared to centrifuged AuNR2$_{1.0}$ and AuNR1, which might be due to the size of nanorods or shifting of the control sample peak upon the addition of NaOH. The as-prepared AuNR2$_{1.0}$ showed no plasmonic or colorimetric change with metal ions in the absence and presence of 5–20 μL NaOH (Figure 7a–c and Supporting Information File 1, Figure S18). The color and plasmon change confirmed the metal–nanoparticle interactions. Gold nanorods of two sizes (AuNR1 and AuNR2) detected different metals,

suggesting that size, concentration, and centrifuged/as-prepared nanorods are critical parameters for designing a sensing probe for heavy metals. Shape and metal (with the same capping) were also evaluated for their role in heavy metal detection. Table 2 summarizes various studies on detecting heavy metals using CTAB-capped metal nanoparticles via linkers or buffers. Table 2 includes detected metals using as-prepared/centrifuged CTAB-capped AgNS, AuNS, AuNR1, and AuNR2.

Possible mechanism of heavy metal detection

Previous studies have established that CTAB prevents interactions with ligands such as metal ions. Consequently, alternative linkers have typically facilitated metal ion detection using CTAB-capped nanoparticles. However, this study has de-

Table 2: Studies related to CTAB-capped gold and silver nanoparticles for the detection of heavy metals.

CTAB-capped nanoparticles	Ligand/linker	Buffer	Metal detected	Reference
AgNP	poly(L-lysine)	—	Hg^{2+}	[9]
AuNS (λ_{max} 530 nm)	sodium thiosulfate	—	Pb^{2+}	[24]
AuNR (λ_{max} 650 nm)	L-cysteine	—	Hg^{2+}	[50]
AuNR (λ_{max} 801 nm)	cysteine	—	Cu^{2+}	[52]
AuNR (λ_{max} 655 nm)	*N*-alkylaminopyrazole ligand, 1-[2-(octylamino)ethyl]-3,5-diphenylpyrazole	—	Hg^{2+}	[53]
AuNR (λ_{max} 732 nm)	TPDT-silicate	—	Hg^{2+}	[54]
AuNR (λ_{max} 625 nm)	$Na_2S_2O_3$	NH_3/NH_4Cl buffers (pH 10.4)	Cu^{2+}	[55]
AuNR	—	hydrogen bromide buffer solution	Cu^{2+}	[56]
AuNR (λ_{max} 700 nm)	dithiothreitol (DTT)	—	As^{3+}	[57]
AuNR	L-arginine	—	Hg^{2+}	[58]
AgNS (λ_{max} 410 nm)	—	—	Hg^{2+}, Cu^{2+}, and Fe^{3+}	this work[a]
AuNS (λ_{max} 525 nm)	—	—	—	this work[a]
AuNR1 (λ_{max} 630 nm)	—	—	Cr^{3+}, Co^{2+}, Ni^{2+}, and Cu^{2+}	
AuNR2 (λ_{max} 770 nm)	—	—	Hg^{2+}, Ni^{2+}, Fe^{3+}, and Cu^{2+}	

[a]The metal detection depends on size, shape (isotropic and anisotropic), concentration (0.5 and 1 OD), and the nature (centrifuged or as-prepared) of the nanoparticles and the volume of added NaOH.

veloped a system capable of detecting metal ions without such linkers. The detection mechanism in this study is influenced by factors such as the amount of NaOH, nanoparticle shape, and nanoparticle concentration. As previously reported, CTAB-capped silver nanospheres detected Cu^{2+} and Hg^{2+}, attributed to the interaction between the metal ions and the nanoparticles. The underlying mechanism is based on the higher affinity of Hg^{2+} towards silver, with a binding energy of 1.78 eV [9]. This strong affinity allows Hg^{2+} ions to penetrate the CTAB bilayer, particularly in AgNS, where the amount of bound CTAB is lower [9]. Additionally, Cu^{2+} ions undergo a galvanic replacement reaction with silver, facilitated by their high redox potential, enabling Cu–Ag interaction in low-bound CTAB nanoparticles [59]. In contrast, gold nanospheres did not exhibit any metal interactions in the presence of NaOH, which is attributed to the tightly bound CTAB on AuNS surfaces. However, CTAB-AuNS was reported to detect Pb^{2+} in the presence of sodium thiosulfate due to the thiol group's higher affinity for metal ions [24]. Furthermore, the study found that AuNR1 and AuNR2 detected metals only in the presence of NaOH, possibly due to the removal of CTAB from the nanorod curvature, which is known to contain less CTAB. Centrifuged $AuNR1_{0.5}$ nanorods detected Cr^{3+}, Co^{2+}, Ni^{2+}, and Cu^{2+} with NaOH volumes of 5–10 μL. Upon increasing the NaOH volume, only Cr^{3+} and Cu^{2+} were detected with $AuNR1_{0.5}$ and $AuNR1_{1.0}$ nanorods. This suggests that NaOH plays a crucial role in facilitating nanorod–metal interactions through surface CTAB dissolution. Similar to the interaction between copper and silver,

copper and gold can undergo galvanic replacement. Gold ions in solution can replace copper atoms in nanoparticles, forming bimetallic structures [60]. It is assumed that Cr^{3+} and Cu^{2+} ions interacted directly with CTAB and adsorbed onto the nanorod surface. Previous studies have shown that CTAB-AuNR in hydrogen bromide-buffered solution and coated with $Na_2S_2O_3$ in NH_3/NH_4Cl buffer selectively detect Cu^{2+} [55,56]. Additionally, L-cysteine-coated gold nanorods have been reported to detect Cu^{2+} [52]. These findings suggest that the interaction between CTAB and Cu^{2+} is independent of the ligand or buffer, as Cu^{2+} was detected across different conditions. In this study, NaOH was employed to weaken CTAB on nanorods, potentially allowing for the detection of multiple metals, which was not observed in previous studies (Table 2). Using longer nanorods (AuNR2), different metals such as Hg^{2+}, Cu^{2+}, Ni^{2+}, and Fe^{3+} were detected. The underlying mechanism is similar to that of AuNR1, where the addition of NaOH leads to weak binding of CTAB on the nanorod surface. This allowed Hg^{2+} to interact with Au due to its high affinity, similar to its interaction with Ag. Previous reports have shown that L-cysteine-, TPDT-silicate-, and L-arginine-coated AuNR can detect Hg^{2+} despite different ligand conjugations [50,54,58]. These findings suggest that metal–ion interactions with CTAB-capped nanoparticles occur through ionic interactions with the surface capping. Once the surface capping is weakened, multiple metals, rather than a single metal, can be detected. This approach enhances the sensing ability regarding various metal ions without the need for additional linkers, ligands, or buffers.

The current study demonstrates superior performance compared to traditional methods and establishes a novel multimetal detection system using CTAB-capped nanoparticles, which has not been reported before.

LOD and LOQ quantification

This study confirmed the detection of heavy metals using CTAB-capped metal nanoparticles by changing the parameters such as size, shape, as-prepared/centrifuged, and concentration of the nanoparticles, as well as the volume of added NaOH solution. However, the detected metals were at 1 ppm concentration. Therefore, it is impossible to calculate the minimum detection limit because the metal detection happened at a minimum threshold of 1 ppm. Despite that, this study allows other researchers to design nanosensors without surface modification or the use of linker molecules for multimetal detection. However, pristine isotropic gold and silver nanoparticles (without capping) detect multiple metals at 1 ppm concentration, including chromium (Supporting Information File 1, Figure S10). Furthermore, the LOD of Cr^{3+} was calculated using bare AuNS using a linear plot in the range of 100–400 ppb (Supporting Information File 1, Figure S19a,b). The LOD and LOQ of Cr^{3+} using pristine gold nanoparticles were 469.34 and 1422.25 ppb, respectively. Even though CTAB-capped nanoparticles do not go beyond 1 ppm, they are selective for metal detection, which is not the case for pristine gold nanospheres. Thus, CTAB-capped metal nanoparticles can be tailored for heavy metal detection without using linkers or buffers by modifying parameters such as size, shape, concentration, as-prepared/centrifuged, and the volume of NaOH solution.

Catalytic efficiency of CTAB-capped nanoparticles

The catalytic efficiency of CTAB-capped metal nanoparticles was investigated using 4-nitrophenol, a commonly employed substrate for assessing the catalytic efficiency of nanoparticles, as a substrate. Previous studies on CTAB-capped nanoparticles have suggested their role as a catalytic agent for the conversion of 4-NP to 4-AP in the presence of $NaBH_4$ [27]. All catalysis experiments were conducted in situ by performing the reduction reaction in a standard 1 cm path length quartz cuvette and measuring the spectral changes as the reaction progressed. The experimental setup involved an aqueous solution of 0.1 mM 4-NP and 0.1 M $NaBH_4$, followed by the addition of CTAB-capped nanoparticles. Immediately after the addition of $NaBH_4$, a color change from light yellow to yellow-green was observed; simultaneously, the spectral absorption changed from 317 to 400 nm due to the formation of 4-nitrophenolate ions in the reaction medium [61]. The reduction of 4-nitrophenolate ions to 4-aminophenol was initiated only upon the addition of nanoparticles as a catalyst, and reaction kinetics were monitored using a UV–visible spectrophotometer. The visible change from yellow

to a colorless solution corresponded to a decrease in the peak intensity at 400 nm and the formation of a minor peak around 300 nm due to the formation of 4-aminophenol. The catalytic conversion of 4-nitrophenol by as-prepared CTAB-$AgNS_{0.5}$ and CTAB-$AgNS_{1.0}$ was completed in 115 and 65 min with catalytic efficiencies of 87.82% and 89.14%, respectively, (Figure 8a,b).

Using centrifuged CTAB-$AgNS_{0.5}$ and CTAB-$AgNS_{1.0}$, the degradation times were 40 and 30 min with catalytic efficiencies of 93.13% and 90.78%, respectively (Figure 8c,d). Shaikh et al. showed the degradation of 4-NP using ginger extract-stabilized CTAB-capped silver nanospheres [62]. However, the current study observed the degradation of 4-NP based on nanoparticle concentration and preparation conditions without using any linker. Centrifuged particles are more efficient compared to as-prepared nanoparticles. In comparison, CTAB and pristine AgNPs (1 OD) degraded 4-NP within 60 and 40 min, respectively (Supporting Information File 1, Figure S20). CTAB-AgNPs degrade 4-NP faster because of a synergistic effect. Furthermore, the impact of the metal with the same capping was also evaluated. Using as-prepared CTAB-$AuNS_{0.5}$ and CTAB-$AuNS_{1.0}$, the degradation of 4-NP was achieved in 3 and 1 min with catalytic efficiencies of 93.91% and 94.37%, respectively (Figure 8e,f). The present findings corroborate those reported by Satapathy and colleagues. The authors concluded that the degradation of 4-NP highly depends on the nanoparticle concentration, which is also observed in our study [61]. Compared to the as-prepared nanoparticles, centrifuged CTAB-$AuNS_{0.5}$ and $AuNS_{1.0}$ took 5 and 3 min with catalytic efficiencies of 87.97% and 93.20%, respectively, for the degradation of 4-NP (Figure 8g,h). The time required for the degradation of 4-NP using centrifuged gold nanospheres is higher than that using as-prepared AuNS. This might be due to the lower amount of CTAB in centrifuged AuNS. The degradation times of 4-NP using CTAB and bare/uncapped AuNS were 60 and 5 min, respectively (Supporting Information File 1, Figure S20). This confirmed that gold nanoparticles have catalytic activity against 4-NP, enhanced upon capping with CTAB. However, it was reported that the shape of nanoparticles also influences their catalytic property in the degradation of 4-NP [63]. Figure 9a,b shows the decrease in optical absorption of 4-NP (λ_{max} 400 nm) using as-prepared CTAB-$AuNR1_{0.5}$ and $AuNR1_{1.0}$ as reaction catalysts. The Figure inset represents a color change from yellow to colorless obtained within 8 and 5 min with catalytic efficiencies of 93.83% and 94.37%, respectively, after the addition of as-prepared CTAB-$AuNR1_{0.5}$ and $AuNR1_{1.0}$.

A similar trend was observed in the case of centrifuged AuNR1, where a high nanoparticle concentration ($AuNR1_{1.0}$) required less time than a lower concentration ($AuNR1_{0.5}$) (Figure 9c,d).
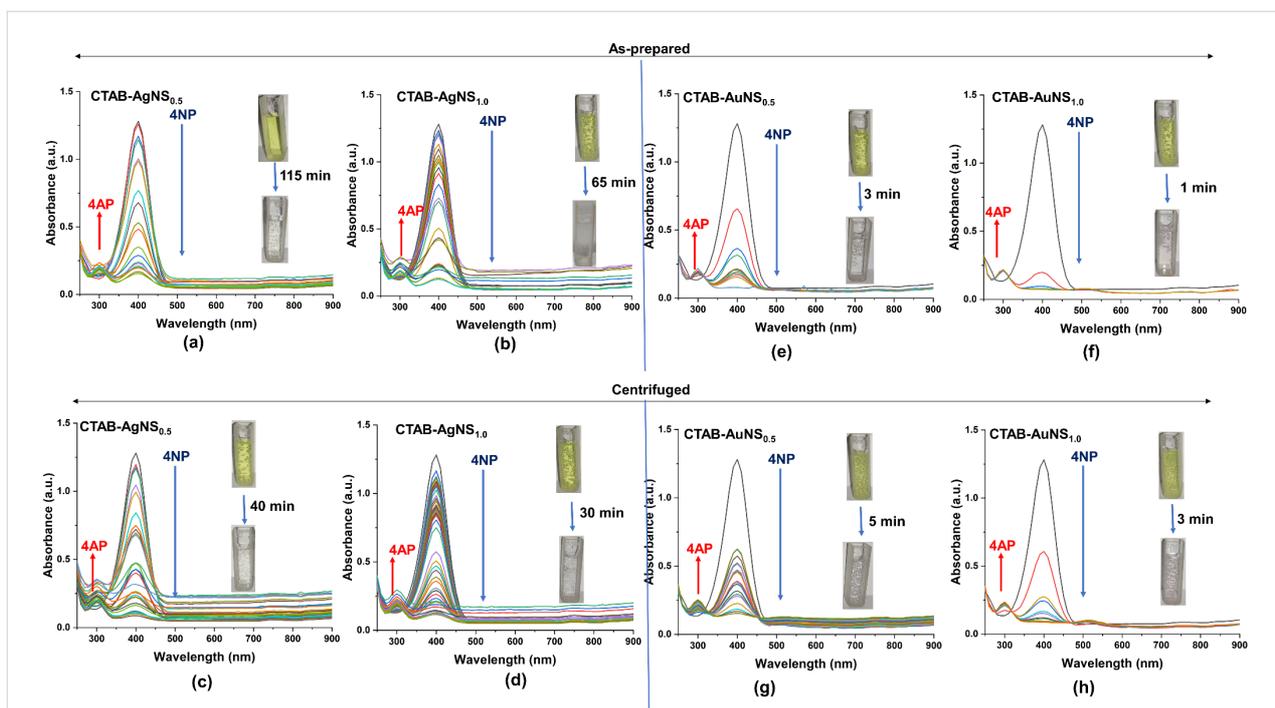
Figure 8: Degradation of 4 nitrophenol (4-NP) to 4 aminophenol (4-AP) using CTAB-AgNS and AuNS. (a) As-prepared $AgNS_{0.5}$, (b) as-prepared $AgNS_{1.0}$, (c) centrifuged $AgNS_{0.5}$, (d) centrifuged $AgNS_{1.0}$, (e) as-prepared $AuNS_{0.5}$, (f) as-prepared $AuNS_{1.0}$, (g) centrifuged $AuNS_{0.5}$, and (h) centrifuged $AuNS_{1.0}$. The inset color shows a change in the degradation of 4-NP to 4-AP. The subscripts 0.5 and 1.0 represent the nanoparticle concentration in terms of optical density.
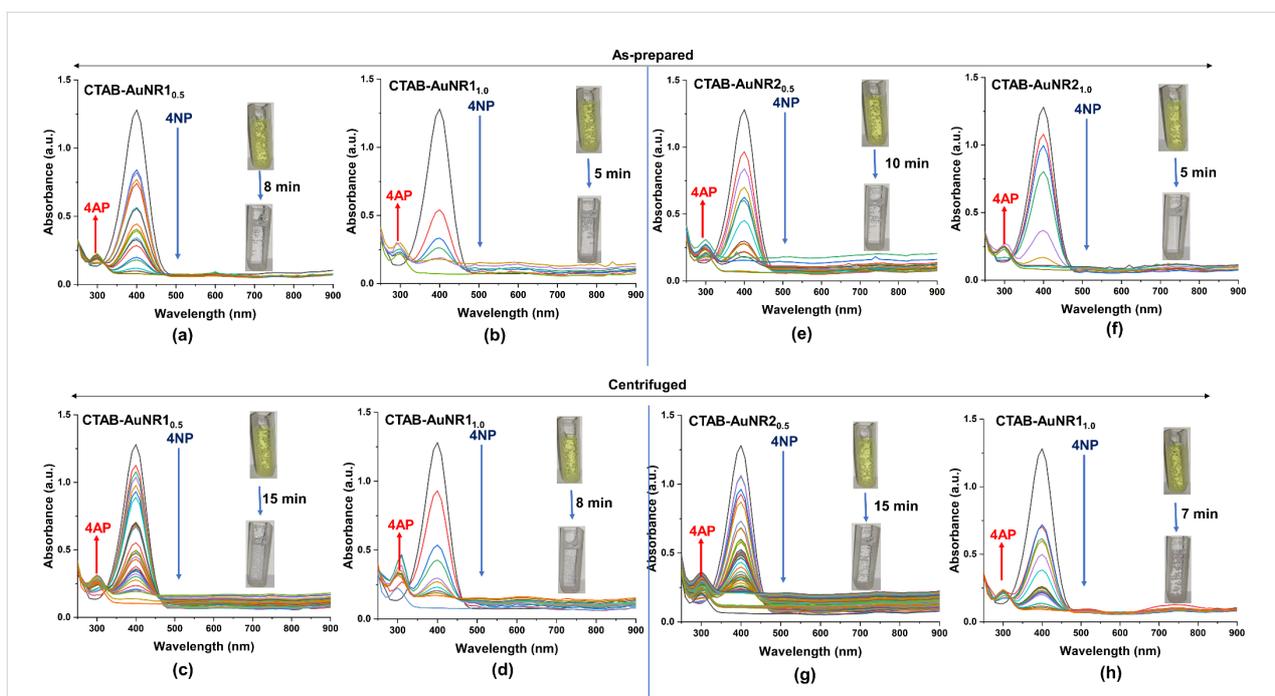
Figure 9: Degradation of 4 nitrophenol (4-NP) to 4 aminophenol (4-AP) using CTAB-AuNR1 and AuNR2. (a) As-prepared $AuNR1_{0.5}$, (b) as-prepared $AuNR1_{1.0}$, (c) centrifuged $AuNR1_{0.5}$, (d) centrifuged $AuNR1_{1.0}$, (e) as-prepared $AuNR2_{0.5}$, (f) as-prepared $AuNR2_{1.0}$, (g) centrifuged $AuNR2_{0.5}$, and (h) centrifuged $AuNR2_{1.0}$. The inset shows the change in degradation of 4-NP to 4-AP. The subscripts 0.5 and 1.0 represent the nanoparticles concentration in terms of optical density.

The degradation times of 4-NP using centrifuged AuNR1$_{0.5}$ and AuNR1$_{1.0}$ were 8 and 5 min with catalytic efficiencies of 91.95% and 93.83%, respectively. This confirmed that as-prepared AuNR1 showed higher efficiency for the degradation of 4-NP compared to centrifuged AuNR1. This might be due to excess CTAB in as-prepared AuNR1, which is also the case with CTAB-AuNS. CTAB, without nanoparticles, can reduce 4-NP to 4-AP (Supporting Information File 1, Figure S20a). However, the degradation time was much higher than that of the CTAB-capped nanoparticles, as observed in the case of CTAB-AuNR1. We also analyzed the role of nanoparticle size in the degradation of 4-NP. Therefore, the potential of longer CTAB-AuNR was also evaluated. As-prepared CTAB-AuNR2$_{0.5}$ and AuNR2$_{1.0}$ showed degradation times of 10 and 5 min with catalytic efficiencies of 94.76% and 93.83%, respectively (Figure 9e,f). Centrifuged CTAB-AuNR2$_{0.5}$ and AuNR2$_{1.0}$ degraded 4-NP within 15 and 7 min with catalytic efficiencies of 95.01% and 92.74%, respectively, similar to the case for CTAB-AuNR1 (Figure 9g,h). A slight change in degradation time was observed due to the size difference of the gold nanorods. A trend reversal in CTAB-AgNS was observed, where centrifuged AgNS showed minimal degradation time compared to as-prepared. The 4-NP degradation time of centrifuged CTAB-AgNS was comparable to that of bare AgNS (Supporting Information File 1, Figure S20). This study suggests that the degradation of 4-NP using nanoparticles highly depends on nanoparticle concentration, size, shape, and preparation. Table 3 summarizes various studies performed regarding the degradation of 4-nitrophenol using nanoparticle-based systems.

Possible mechanism of 4-NP degradation
The catalytic degradation of 4-NP was achieved using CTAB-capped nanoparticles as nanocatalysts, where CTAB-AuNS is highly efficient compared to CTAB-AgNS, CTAB-AuNR1, and CTAB-AuNR2. The underlying mechanism behind 4-NP degradation using CTAB-capped gold and silver nanoparticles involves a complex series of surface-mediated reactions. Initially, 4-NP in its ionic form (4-nitrophenolate) penetrates the CTAB bilayer and adsorbs onto the metal nanoparticle surface, facilitated by electrostatic interactions [69,70]. Concurrently, borohydride ions (BH^{4-}) from NaBH$_4$ also adsorb on the nanoparticle surface. The metal nanoparticle acts as an electron relay, accepting electrons from BH^{4-} and transferring them to the adsorbed 4-nitrophenolate [69]. This electron transfer initiates a stepwise reduction of the nitro group, proceeding through nitroso and hydroxylamine intermediates before finally yielding 4-aminophenol (4-AP).

The reduction follows the pathway: 4-NO$_2$-phenolate → 4-NO-phenolate → 4-NHOH-phenolate → 4-NH$_2$-phenolate. Once formed, 4-AP desorbs from the nanoparticle surface, allowing the catalytic cycle to continue [69]. The efficiency of this process is influenced by nanoparticle properties such as surface area, size, and shape, with smaller particles generally exhibiting higher catalytic activity due to their increased surface-to-volume ratio.

Conclusion
This study developed a flexible nanosensor without linkers, using cetyltrimethylammonium bromide as capping agent on gold and silver nanoparticles. The nanosensor was designed to rapidly detect heavy metal ions and degrade organic pollutants like 4-nitrophenol. CTAB-AgNS, CTAB-AuNS, CTAB-AuNR1, and CTAB-AuNR2 nanoparticles were characterized regarding size, shape, surface charge, functional group interactions, and crystalline structure. Stability tests with NaCl and NaOH showed that CTAB-AgNS exhibited decreased plas-

Table 3: Studies related to nanoparticles for the degradation of 4-nitrophenol.

System	Shape	Degradation time (min)	Reference
CTAB-AuNP	sphere	1	[61]
CTAB-AgNP and bare AgNP (in extract)	sphere	3	[62]
Silica coated CTAB-AuNR	rod	5–6	[64]
Cochliobolus geniculatus coated ZnO nanoparticles	quasi-spherical	30	[65]
B. amyloliquefaciens capped silver nanoparticles	sphere	15	[66]
Jatropha leaf extract capped iron nanoparticles	irregular shaped	60	[67]
polyvinyl alcohol/silver nanoparticle film	sphere	25	[68]
CTAB AgNS	sphere	30	this work[a]
CTAB-AuNS	sphere	1	
CTAB-AuNR1	rod	5	
CTAB-AuNR2	rod	5	

[a]The obtained degradation time depends on nanoparticle concentration, size, shape and preparation of the nanoparticles.

monic intensity and aggregation, while CTAB-AuNS and CTAB-AuNR1 demonstrated higher stability than CTAB-AuNR2. CTAB-AuNS efficiently degraded 4-nitrophenol (94.37% within 1 min), while CTAB-AuNR1 and AuNR2 degraded it within 5 min with an efficiency of 94.37% and 93.83%, respectively. The efficiency of the sensing probes depended on factors like nanoparticle concentration, preparation method (as-prepared/centrifuged), and NaOH addition. As-prepared CTAB-AgNS detected Cu^{2+} and Hg^{2+} ions at specific concentrations, whereas CTAB-AuNR1 and AuNR2 detected multiple metals under particular conditions. CTAB-AuNS showed no metal ion detection capability. These results highlight the importance of size, shape, concentration, and preparation method of the nanoparticles in sensing and catalytic applications. The sensor achieved metal ion detection at 1 ppm without linkers or buffer solvents and detected multiple metal ions based on reaction parameters. Future research will enhance sensitivity towards metal detection using linker-free CTAB-capped metal nanoparticles combined with advanced strategies. This study demonstrates the potential of linker-free CTAB-capped metal nanoparticles for simultaneous pollutant detection and degradation, offering promising environmental remediation and sensing applications.

Supporting Information

The file contains twenty figures. Figure S1 is an HPLC chromatogram showing peak retention time for CTAB and CTAB-capped nanoparticles. Figures S2–S9 are spectrophotometric and colorimetric visualizations of metal detection using isotropic CTAB-capped nanoparticles. Figure S10 depicts the spectrophotometric and colorimetric detection of metal ions using bare gold and silver nanoparticles. Figures S11–S18 show the detection of metal ions using anisotropic nanoparticles of gold (i.e., AuNR1 and AuNR2). Figures S19 and S20 present the quantification of Cr^{3+} using bare AuNS and the catalytic degradation of 4-NP with CTAB, bare AuNS and bare AgNS, respectively.

Supporting Information File 1
Additional figures.
[https://www.beilstein-journals.org/bjnano/content/supplementary/2190-4286-15-106-S1.pdf]

Conflict of Interest
The authors declare that there is no conflict of interest.

Author Contributions
Akash Kumar: data curation; investigation; methodology; validation; visualization; writing – original draft. Raja Gopal Rayavarapu: conceptualization; data curation; formal analysis; funding acquisition; investigation; project administration; resources; software; supervision; validation; visualization; writing – review & editing.

ORCID® iDs
Akash Kumar - https://orcid.org/0000-0002-0493-1991
Raja Gopal Rayavarapu - https://orcid.org/0000-0002-8769-4679

Data Availability Statement
The data that supports the findings of this study is available from the corresponding author upon reasonable request.

References
1. Das, A.; Dey, A. *J. Environ. Chem. Eng.* **2020,** *8,* 103830. doi:10.1016/j.jece.2020.103830
2. Ariga, K. *Bull. Chem. Soc. Jpn.* **2024,** *97,* uoad001. doi:10.1093/bulcsj/uoad001
3. Javed, R.; Zia, M.; Naz, S.; Aisida, S. O.; Ain, N. u.; Ao, Q. *J. Nanobiotechnol.* **2020,** *18,* 172. doi:10.1186/s12951-020-00704-4
4. Li, X.; Yoneda, M.; Shimada, Y.; Matsui, Y. *Sci. Total Environ.* **2017,** *574,* 176–182. doi:10.1016/j.scitotenv.2016.09.065
5. Al-Thabaiti, S. A.; Obaid, A. Y.; Hussain, S.; Khan, Z. *Arabian J. Chem.* **2015,** *8,* 538–544. doi:10.1016/j.arabjc.2014.11.030
6. Carnovale, C.; Bryant, G.; Shukla, R.; Bansal, V. *ACS Omega* **2019,** *4,* 242–256. doi:10.1021/acsomega.8b03227
7. El-Nahass, M. N.; Bakr, E. A.; Fayed, T. A.; Hamada, W. M.; Salem, M. M.; Radwan, A. M. *J. Iran. Chem. Soc.* **2024,** *21,* 699–718. doi:10.1007/s13738-023-02952-1
8. Anna, K. K.; Bogireddy, N. K. R.; Ramírez-Bon, R. *Nanotechnology* **2021,** *32,* 105707. doi:10.1088/1361-6528/abccee
9. Moudgil, L.; Jaiswal, J.; Mittal, A.; Saini, G. S. S.; Singh, G.; Kaura, A. *J. Mol. Liq.* **2019,** *276,* 910–918. doi:10.1016/j.molliq.2018.12.106
10. Tchieno, F. M. M.; Tonle, I. K. *Rev. Anal. Chem.* **2018,** *37,* 20170019. doi:10.1515/revac-2017-0019

11. Abd Elnabi, M. K.; Elkaliny, N. E.; Elyazied, M. M.; Azab, S. H.; Elkhalifa, S. A.; Elmasry, S.; Mouhamed, M. S.; Shalamesh, E. M.; Alhorieny, N. A.; Abd Elaty, A. E.; Elgendy, I. M.; Etman, A. E.; Saad, K. E.; Tsigkou, K.; Ali, S. S.; Kornaros, M.; Mahmoud, Y. A.-G. *Toxics* **2023,** *11,* 580. doi:10.3390/toxics11070580

12. Teschke, R. *Int. J. Mol. Sci.* **2022,** *23,* 12213. doi:10.3390/ijms232012213

13. Wyatt, L. H.; Luz, A. L.; Cao, X.; Maurer, L. L.; Blawas, A. M.; Aballay, A.; Pan, W. K. Y.; Meyer, J. N. *DNA Repair* **2017,** *52,* 31–48. doi:10.1016/j.dnarep.2017.02.005

14. Yuen, H.-W.; Becker, W. Iron toxicity. *StatPearls [Internet];* StatPearls Publishing, 2023. PMID:29083637.

15. Bradberry, S. M. *Medicine* **2016,** *44,* 182–184. doi:10.1016/j.mpmed.2015.12.008

16. Naushad, M.; Ahamad, T.; Rizwan Khan, M. *Chemosphere* **2022,** *303,* 135173. doi:10.1016/j.chemosphere.2022.135173

17. Szafran, B.; Klein, R.; Buser, M.; Balachandran, R.; Haire, K.; Derrick, H.; Roney, N.; Hall, S.; Gao, A.; Zaccaria, K. CHAPTER 1: RELEVANCE TO PUBLIC HEALTH. *Toxicological Profile for Nitrophenols;* Agency for Toxic Substances and Disease Registry (US): Atlanta (GA), 2023. https://www.ncbi.nlm.nih.gov/books/NBK601147/

18. Xu, G.; Song, P.; Xia, L. *Nanophotonics* **2021,** *10,* 4419–4445. doi:10.1515/nanoph-2021-0363

19. Singh, A.; Shah, S. S.; Sharma, C.; Gupta, V.; Sundramoorthy, A. K.; Kumar, P.; Arya, S. *J. Environ. Chem. Eng.* **2024,** *12,* 113032. doi:10.1016/j.jece.2024.113032

20. Javaid, R.; Kawasaki, S.-i.; Suzuki, A.; Suzuki, T. M. *Beilstein J. Org. Chem.* **2013,** *9,* 1156–1163. doi:10.3762/bjoc.9.129

21. Chen, Z.; Zhang, Z.; Qi, J.; You, J.; Ma, J.; Chen, L. *J. Hazard. Mater.* **2023,** *441,* 129889. doi:10.1016/j.jhazmat.2022.129889

22. Alberti, G.; Zanoni, C.; Magnaghi, L. R.; Biesuz, R. *Chemosensors* **2021,** *9,* 305. doi:10.3390/chemosensors9110305

23. Kailasa, S. K.; Chandel, M.; Mehta, V. N.; Park, T. J. *Spectrochim. Acta, Part A* **2018,** *195,* 120–127. doi:10.1016/j.saa.2018.01.038

24. Nguyen, N. L. T.; Kim, E. J.; Chang, S.-K.; Park, T. J. *BioChip J.* **2016,** *10,* 65–73. doi:10.1007/s13206-016-0109-8

25. Sung, H. K.; Oh, S. Y.; Park, C.; Kim, Y. *Langmuir* **2013,** *29,* 8978–8982. doi:10.1021/la401408f

26. Yagyu, J.; Islam, M. S.; Yasutake, H.; Hirayama, H.; Zenno, H.; Sugimoto, A.; Takagi, S.; Sekine, Y.; Ohira, S.-I.; Hayami, S. *Bull. Chem. Soc. Jpn.* **2022,** *95,* 862–870. doi:10.1246/bcsj.20220058

27. Fenger, R.; Fertitta, E.; Kirmse, H.; Thünemann, A. F.; Rademann, K. *Phys. Chem. Chem. Phys.* **2012,** *14,* 9343–9349. doi:10.1039/c2cp40792b

28. Sui, Z. M.; Chen, X.; Wang, L. Y.; Xu, L. M.; Zhuang, W. C.; Chai, Y. C.; Yang, C. J. *Phys. E (Amsterdam, Neth.)* **2006,** *33,* 308–314. doi:10.1016/j.physe.2006.03.151

29. Silva, L. I. M.; Pérez-Gramatges, A.; Larrude, D. G.; Almeida, J. M. S.; Aucélio, R. Q.; da Silva, A. R. *Colloids Surf., A* **2021,** *614,* 126174. doi:10.1016/j.colsurfa.2021.126174

30. Rayavarapu, R. G.; Petersen, W.; Hartsuiker, L.; Chin, P.; Janssen, H.; van Leeuwen, F. W. B.; Otto, C.; Manohar, S.; van Leeuwen, T. G. *Nanotechnology* **2010,** *21,* 145101. doi:10.1088/0957-4484/21/14/145101

31. Das, N.; Kumar, A.; Kumar Roy, S.; Kumar Satija, N.; Raja Gopal, R. *IET Nanobiotechnol.* **2020,** *14,* 851–857. doi:10.1049/iet-nbt.2020.0097

32. He, J.; Unser, S.; Bruzas, I.; Cary, R.; Shi, Z.; Mehra, R.; Aron, K.; Sagle, L. *Colloids Surf., B* **2018,** *163,* 140–145. doi:10.1016/j.colsurfb.2017.12.019

33. Kuperkar, K.; Abezgauz, L.; Prasad, K.; Bahadur, P. *J. Surfactants Deterg.* **2010,** *13,* 293–303. doi:10.1007/s11743-009-1173-z

34. Kianfar, E. Catalytic Properties of Nanomaterials and Factors Affecting it. *Importance & Applications of Nanotechnology;* MedDocs Publishers, 2020; Vol. 5, pp 22–25. https://meddocsonline.org/ebooks/ebook-nanotechnology/catalytic-properties-of-nanomaterials-and-factors-affecting-it.pdf

35. Ziai, Y.; Rinoldi, C.; Nakielski, P.; De Sio, L.; Pierini, F. *Curr. Opin. Biomed. Eng.* **2022,** *24,* 100413. doi:10.1016/j.cobme.2022.100413

36. Sahu, A. K.; Das, A.; Ghosh, A.; Raj, S. *Nano Express* **2021,** *2,* 010009. doi:10.1088/2632-959x/abd966

37. da Silva, J. A.; Netz, P. A.; Meneghetti, M. R. *Langmuir* **2020,** *36,* 257–263. doi:10.1021/acs.langmuir.9b03235

38. Kalipillai, P.; Raghuram, E.; Bandyopadhyay, S.; Mani, E. *Phys. Chem. Chem. Phys.* **2022,** *24,* 28353–28361. doi:10.1039/d2cp02202h

39. Fischer, K.; Schmidt, M. *Biomaterials* **2016,** *98,* 79–91. doi:10.1016/j.biomaterials.2016.05.003

40. Danaei, M.; Dehghankhold, M.; Ataei, S.; Hasanzadeh Davarani, F.; Javanmard, R.; Dokhani, A.; Khorasani, S.; Mozafari, M. R. *Pharmaceutics* **2018,** *10,* 57. doi:10.3390/pharmaceutics10020057

41. Joseph, E.; Singhvi, G. Multifunctional nanocrystals for cancer therapy: a potential nanocarrier. *Nanomaterials for Drug Delivery and Therapy;* Elsevier: Amsterdam, Netherlands, 2019; pp 91–116. doi:10.1016/b978-0-12-816505-8.00007-2

42. Mandal, S.; Arumugam, S. K.; Adyanthaya, S. D.; Pasricha, R.; Sastry, M. *J. Mater. Chem.* **2004,** *14,* 43–47. doi:10.1039/b308180j

43. Nikoobakht, B.; El-Sayed, M. A. *Langmuir* **2001,** *17,* 6368–6374. doi:10.1021/la010530o

44. Niu, Y.; Omurzak, E.; Cai, R.; Syrgakbek kyzy, D.; Zhasnakunov, Z.; Satyvaldiev, A.; Palmer, R. E. *Surfaces (Basel, Switz.)* **2022,** *5,* 202–208. doi:10.3390/surfaces5010013

45. Yadav, V. D.; Jain, R.; Dandekar, P. *Mater. Res. Express* **2017,** *4,* 085015. doi:10.1088/2053-1591/aa8088

46. Cunningham, B.; Engstrom, A. M.; Harper, B. J.; Harper, S. L.; Mackiewicz, M. R. *Nanomaterials* **2021,** *11,* 1516. doi:10.3390/nano11061516

47. Vashishtha, M.; Mishra, M.; Shah, D. O. *J. Mol. Liq.* **2015,** *210,* 151–159. doi:10.1016/j.molliq.2015.02.017

48. Roque, L.; Fernández, M.; Benito, J. M.; Escudero, I. *Colloids Surf., A* **2020,** *601,* 124999. doi:10.1016/j.colsurfa.2020.124999

49. Samuel, V. R.; Rao, K. J. *Appl. Nanosci.* **2024,** *14,* 33–42. doi:10.1007/s13204-023-02948-6

50. Placido, T.; Comparelli, R.; Striccoli, M.; Agostiano, A.; Merkoci, A.; Curri, M. L. *IEEE Sens. J.* **2013,** *13,* 2834–2841. doi:10.1109/jsen.2013.2257738

51. Shahbazi, N.; Zare-Dorabei, R. *ACS Omega* **2019,** *4,* 17519–17526. doi:10.1021/acsomega.9b02389

52. Xu, S.; Wang, Y.; Sun, Y.; Shan, G.; Chen, Y.; Liu, Y. *Sens. Actuators, B* **2017,** *248,* 761–768. doi:10.1016/j.snb.2017.04.016

53. Placido, T.; Aragay, G.; Pons, J.; Comparelli, R.; Curri, M. L.; Merkoci, A. *ACS Appl. Mater. Interfaces* **2013,** *5,* 1084–1092. doi:10.1021/am302870b

54. Jayabal, S.; Sathiyamurthi, R.; Ramaraj, R. *J. Mater. Chem. A* **2014,** *2,* 8918–8925. doi:10.1039/c4ta01363h

55. Chen, Z.; Liu, R.; Wang, S.; Qu, C.; Chen, L.; Wang, Z. *RSC Adv.* **2013,** *3,* 13318–13323. doi:10.1039/c3ra40559a

56. Zhang, Z.; Chen, Z.; Qu, C.; Chen, L. *Langmuir* **2014,** *30,* 3625–3630. doi:10.1021/la500106a

57. Ge, K.; Liu, J.; Fang, G.; Wang, P.; Zhang, D.; Wang, S. *Sensors* **2018,** *18,* 2372. doi:10.3390/s18072372

58. Guan, J.; Wang, Y.-C.; Gunasekaran, S. *J. Food Sci.* **2015,** *80,* N828–N833. doi:10.1111/1750-3841.12811

59. He, X.; He, R.; Lan, Q.; Duan, F.; Xiao, J.; Song, M.; Zhang, M.; Chen, Y.; Li, Y. *J. Nanomater.* **2016,** *2016,* 2127980. doi:10.1155/2016/2127980

60. Luo, K.; Li, Y.; Liu, T.; Zhuge, X.; Chung, E.; Timms, A. R.; Graham, S. P.; Ren, G. *ACS Omega* **2023,** *8,* 36171–36178. doi:10.1021/acsomega.3c03665

61. Satapathy, S.; Mohanta, J.; Si, S. *ChemistrySelect* **2016,** *1,* 4940–4948. doi:10.1002/slct.201600985

62. Shaikh, J. A. *J. Iran. Chem. Soc.* **2022,** *19,* 4149–4158. doi:10.1007/s13738-022-02593-w

63. De Oliveira, F. M.; Nascimento, L. R. B. d. A.; Calado, C. M. S.; Meneghetti, M. R.; Da Silva, M. G. A. *Catalysts* **2016,** *6,* 215. doi:10.3390/catal6120215

64. Mohanta, J.; Satapathy, S.; Si, S. *ChemPhysChem* **2016,** *17,* 364–368. doi:10.1002/cphc.201501127

65. Kadam, V. V.; Shanmugam, S. D.; Ettiyappan, J. P.; Balakrishnan, R. M. *Environ. Sci. Pollut. Res.* **2021,** *28,* 12119–12130. doi:10.1007/s11356-020-10833-w

66. Samuel, M. S.; Jose, S.; Selvarajan, E.; Mathimani, T.; Pugazhendhi, A. *J. Photochem. Photobiol., B* **2020,** *202,* 111642. doi:10.1016/j.jphotobiol.2019.111642

67. Rawat, S.; Singh, J.; Koduru, J. R. *Environ. Technol. Innovation* **2021,** *24,* 101857. doi:10.1016/j.eti.2021.101857

68. Mostafa, A. M.; Menazea, A. A. *J. Mol. Struct.* **2020,** *1212,* 128125. doi:10.1016/j.molstruc.2020.128125

69. Mejía, Y. R.; Reddy Bogireddy, N. K. *RSC Adv.* **2022,** *12,* 18661–18675. doi:10.1039/d2ra02663e

70. Das, T. K.; Das, N. C. *Int. Nano Lett.* **2022,** *12,* 223–242. doi:10.1007/s40089-021-00362-w

Clays enhanced with niobium: potential in wastewater treatment and reuse as pigment with antibacterial activity

Silvia Jaerger[*1,2], Patricia Appelt[‡2], Mario Antônio Alves da Cunha[‡3], Fabián Ccahuana Ayma[‡2], Ricardo Schneider[‡1], Carla Bittencourt[‡4] and Fauze Jacó Anaissi[*,‡2]

Full Research Paper

Address:
[1]Federal University of Technology - Paraná - UTFPR, Campus Toledo, Rua Cristo Rei, 19. 85902-490, Toledo, Brazil, [2]Chemistry Department, Universidade Estadual do Centro-Oeste, Guarapuava 85040-167, PR, Brazil, [3]Department of Chemistry, Universidade Tecnológica Federal do Paraná, Pato Branco 85503-390, Brazil and [4]Chimie des Interactions PlaBEa-Surface (ChIPS), Research Institute for Materials Science and Engineering, University of Mons, 7000 Mons, Belgium

Email:
Silvia Jaerger[*] - sjaerger@gmail.com; Fauze Jacó Anaissi[*] - anaissi@unicentro.br

* Corresponding author   ‡ Equal contributors

Abstract

Bentonite clay sourced from the Guarapuava region, Brazil, was modified with niobium oxide (BEOx) and niobium phosphate (BEPh) to act as an adsorbent and photocatalyst in the remediation of wastewater containing methylene blue (MB) dye. Additionally, colored materials were evaluated for their potential as antibacterial hybrid pigments. The bentonite clay modified with niobium was prepared by a solution containing swelling clay mixed with niobium oxide (NbOx) and niobium phosphate (NbPh) in a water solution; after that, the suspension was calcinated. X-ray diffractometry, X-ray photoelectron spectroscopy, and laser-induced breakdown spectroscopy assessed the modifications induced by the incorporation of niobium compounds into the clay, confirming the presence of niobium in the bentonite clay. Following characterization, the BEOx and BEPh samples were used as adsorbents or photocatalysts for treating solutions containing the MB dye (400 mg·L^{-1}) at 25 °C. The results showed adsorption and photocatalysis efficiency above 94% for both samples. The blue-colored BEOx and BEPh samples were then applied as a hybrid pigment. The power pigment and its dispersion in colorless paint were evaluated by the CIEL*a*b* color space, and the ΔE parameters show values above 12, indicating a very strong color parameter difference. Subsequently, the efficacy of BEOx and BEPh as a hybrid pigment was assessed using the minimum inhibitory concentration (MIC) assay against two bacteria strains: *Bacillus cereus* (ATCC 10876) and *Proteus mirabilis* (ATCC 35649). The analysis revealed remarkable antibacterial activity against *Proteus mirabilis*, suggesting a preferential selectivity for Gram-negative bacteria.

Introduction

The most found dye pollutants in wastewater on a global scale originate from textile, plastic, paper, food, cosmetics, mineral, and pharmaceutical industries, among others, resulting in significant environmental impacts [1]. Dyes, as chemical compounds that impart color to different materials, play a crucial role in industries requiring coloring, such as textile, food, cosmetics, rubber, printing, paper, and plastic. Globally, an estimated 7×10^5 tons of dyes are produced, with 10–15% typically disposed of as wastewater pollutants [2]. Among the most used dyes, methylene blue (MB) is an intense blue cationic dye important in medical sciences, chemistry, and biology, as well as widely used in the textile industry [2]. Prolonged exposure to MB can result in adverse health effects, including abdominal disorders, respiratory distress, skin sensitization, and blindness [3]. The dark blue color of MB in wastewater reduces light penetration into aquatic organisms, disturbing the balance of the ecosystem and harming various forms of life [3]. Effluents and water bodies containing MB require prioritized treatment due to its adverse effect on water quality. Therefore, it is crucial to explore remedial strategies for MB, especially considering the water scarcity challenges that many countries face [3].

To satisfy environmental regulations, a range of wastewater treatment technologies with inherent advantages and limitations are available, encompassing processes such as advanced oxidation, extraction, and biodegradation [4]. Unfortunately, these methods exhibit inefficiencies due to the generation of secondary pollution and high operational costs. Biological and anaerobic degradation of dyes may yield carcinogenic by-products [4,5], highlighting the significant challenge in purifying water contaminated with dyes necessitating the development of cost-effective technologies for their removal from industrial effluents.

Adsorption emerges as a widely used method for pollutant removal from wastewater due to its design simplicity, operational ease, and relatively straightforward regeneration of the adsorbent. Various adsorbents including chitosan, cellulose, organophilic clays, kaolinite and montmorillonite clays, and activated carbon have been used for removing toxic compounds from polluted water [6]. Among these adsorbents, bentonite and smectite clays exhibit advantageous properties as an adsorbent, characterized by their low cost, abundant availability, nontoxic nature, and large surface area [2,7]. Additionally, its negatively charged surface renders it favorable for the adsorption of cations [7]. Bentonite clay is abundantly found in Guarapuava, Paraná, Brazil. This natural clay has predominantly the bentonite phase (at least 50%), known as montmorillonite. Isomorphic substitution of cations between the interlayer space of montmorillonites by exchanging Na^+, Ca^{2+},

Mg^{2+}, and Cu^{2+} cations add other functionalities to the resulting material [7].

Heterogeneous photocatalysis is a cost-effective alternative to biological treatment methods for purifying polluted water [8]. Using semiconductors as heterogeneous catalysts proves to be more efficient than traditional methods, as the photocatalytic process gradually decomposes contaminating molecules without generating residues from the original organic matter, thus avoiding the disposal of sludge [8]. This approach allows the removal of various organic pollutants, including textile dyes, using solid semiconductors (e.g., $NbOPO_4$ and Nb_2O_5) and photons (with energy greater than the bandgap energy of the semiconductor) to generate $OH^•$ radicals (strong oxidants), leading to the mineralization of organic pollutants, including textile dyes [8].

In this study, the strategy and objective are to modify bentonite clay with niobium phosphate and niobium oxide by the calcinated method, and then use it as an adsorbent or photocatalyst to treat MB dye solutions and reuse this material as a hybrid pigment. Considering the semiconductor properties of niobium and the high capacity of the clay to remove pollutants from wastewater, we proposed in this research to use the niobium-modified clay as an adsorbent and photocatalyst to treat MB dye solutions. To reuse this colored material, recovered from the adsorption and photocatalysis tests, we propose using these as-prepared, blue-colored samples as a hybrid pigment. Subsequently, the as-prepared, blue-colored samples were evaluated for their color properties by CIEL*a*b* color space as a pigment in the powder form and dispersed in colorless paint. The novel-developed pigments, specifically the smectite clay modified with niobium-containing adsorbed dye, were investigated as antibacterial pigments.

Experimental
Materials

The bentonite clay from the Guarapuava region in the Parana State, Brazil, was purchased from a local supplier. Niobium phosphate ($NbOPO_4$) and niobium pentoxide (Nb_2O_5) were provided as donations by Companhia Brasileira de Metalurgia e Mineração (CBMM). Methylene blue, with molecular mass of $319.8513 \ g \cdot mol^{-1}$, was obtained from Nuclear (Brazil).

Clay modified with niobium

First, the clays were swollen; for this purpose, 2 g of bentonite clay was dispersed in 100 mL of water, and the resulting suspension was kept under stirring for 24 h. In this experiment step, the color of raw clay was brown (Figure 1a). Then, 3.14 g of $NbOPO_4$ and Nb_2O_5 was added. The clay/Nb suspension was

Figure 1: The appearance of the sample of bentonite: raw bentonite (a); bentonite modified with NbOPO₄ (b), and bentonite modified with Nb₂O₅ (c).

continuously stirred for 72 h at 65 °C. The color of the bentonite modified with niobium changes to light yellow (Figure 1b,c). Finally, after being cooled to room temperature, the suspensions were subjected to thermal treatment at 500 °C, with a heating rate of 5 °C/min. These samples were named BEPh and BEOx for modification with NbOPO₄ and Nb₂O₅, respectively.

Adsorption and photocatalysis tests

Before the adsorption and photocatalysis assessments, a stock solution of the MB dye was prepared at a concentration of $1\ \text{g·L}^{-1}$. The calibration analytical curve was established using a UV–vis spectrophotometer at a wavelength of 664 nm.

Adsorption experiments were conducted in batches containing 250 mg of the BEPh and BEOx samples under agitation at 25 °C. A volume of 100 mL of MB solutions at a concentration of $400\ \text{mg·L}^{-1}$ were used for 3 h. The adsorption experiment was carried out considering ambient light conditions in the laboratory. Following the adsorption process, the clay/Nb samples were centrifuged at 3500 rpm for 10 min, and the final concentration of the solutions was determined using a UV–vis spectrophotometer. These samples were named A-BEPh and A-BEOx to designate the modification with NbOPO₄ and Nb₂O₅, respectively.

Photocatalytic tests were performed using 100 mL of an MB solution at a concentration of $400\ \text{mg·L}^{-1}$. This experiment used 250 mg of the BEPh and BEOx samples as catalysts. The experimental setup system included a thermostatic Pyrex glass reactor at 25 °C (open), a magnetic stirrer, and a UV lamp (253.7 nm, 15 W, 220 V) within a dark chamber. After 3 h of exposure, the solutions were centrifuged at 3500 rpm for 10 min, and their final concentrations were determined using a UV–vis spectrophotometer. These samples were labeled as A-BEPhP and A-BEOxP to designate the modifications with NbOPO₄ and Nb₂O₅, respectively.

The adsorption efficiency of MB by the clays was calculated using Equation 1:

$$\%\text{Remotion} = 100 \cdot \frac{\left(C_0 - C_\text{f}\right)}{C_0}, \tag{1}$$

where C_0 (mg·L⁻¹) is the initial concentration of the solution, and C_f (mg·L⁻¹) is the concentration of the solution after the adsorption experiment.

The efficiency of MB photodegradation ($X\%$) was determined by Equation 2:

$$X\left(\%\right) = \frac{\left(M_0 - M_\text{f}\right)}{M_0} \cdot 100, \tag{2}$$

where M_0 and M_f are the concentrations of MB at the beginning and at the end of the photocatalytic test, respectively.

Dispersion of the pigments clay/Nb and clay/Nb/MB in colorless commercial paint

The samples A-BEPh, A-BEOx, A-BEPhP, and A-BEOxP were separated through centrifugation and dried in an oven at 70 °C. The clay powders, clay/Nb, and clay/Nb/MB powders were tested as pigments in colorless commercial paint. For this purpose, a 10% (w/w) ratio of the pigments in colorless commercial paint (a transparent paint) was used. A sodium hydroxide solution (NaOH, 1 mol·L⁻¹) was dripped onto the clay powders until reaching a pH between 8 and 10. Subsequently, this suspension was blended with the transparent paint. Plaster molds were painted with both colorless and pigmented paint. After the paint dried, the color was characterized through colorimetric analysis (CIEL*a*b*) and UV–vis spectroscopy.

Antimicrobial activity test

The antimicrobial properties of the BEPh, BEOx, A-BEPh, A-BEOx, A-BEPhP, and A-BEOxP samples were investigated against the bacteria *Bacillus cereus* (ATCC 10876) (Gram-positive) and *Proteus mirabilis* (ATCC 35649) (Gram-negative). The samples of bentonite clay modified with niobium were

dispersed in water. The assay followed the protocols described by the Clinical and Laboratory Standards Institute (CLSI). The samples were evaluated using the minimum inhibitory concentration (MIC) method [9,10] at concentrations ranging from 1.25 to 0.09 mg/mL.

The bacterial stock cultures were activated by culturing in brain heart infusion (BHI) broth at 37 °C for 24 h. Then, the cellular concentrations were standardized according to the McFarland 0.5 scale ($\approx 1.5 \times 10^8$ CFU/mL) using a spectrophotometer at a wavelength of 625 nm in saline water tubes. Subsequently, 100 µL of Mueller–Hinton broth was added to all wells in 96-well plates, followed by duplicate addition of the samples using serial microdilution, and finally, 10 µL of the inoculum. The plates were then incubated for 24 h at 37 °C. After incubation, 20 µL of the TTC dye (0.125% w/v - 2,3,5-triphenyltetrazolium chloride 0.125%) (NEON®) was added to all wells, and the plate was kept in an oven for an additional two hours. The antibacterial activity was determined by MIC, observing the presence/absence of viable bacteria due to the reaction of the TTC dye with the enzyme succinate dehydrogenase (present in the mitochondria), leading to the formation of a salt called Formazan with a pink-reddish color.

Characterization

X-ray diffraction (XRD) measurements of the powder were conducted using a Rigaku BEartLab SE 3 kW diffractometer equipped with Cu Kα radiation (λ = 1.5410 Å) operating at 40 kV and 30 mA. Data were collected in scanning mode in steps between 4° and 75° (2θ) with a step size of 0.05°/s. The basal distance was obtained using Bragg's Law.

Fourier-transform infrared spectroscopy (FTIR) spectra were collected on a Perkin Elmer Frontier FTIR spectrometer using KBr pellets containing 1% by weight of the samples. Analyses of all samples were performed in the range of 4000 to 400 cm^{-1} with a resolution of 4 cm^{-1}, accumulating 10 scans.

Absorbance measurements of the supernatant solutions were analyzed using a UV–vis spectrophotometer (UV-1800 SHIMADZU) with a 1 cm path length glass cuvette at λ$_{max}$ (maximum absorbance) in nanometers.

Samples collected after the adsorption process had the electronic spectra analyzed using an Ocean Optics USB-2000 instrument for solid samples with a tungsten lamp in the range of 200–800 nm in diffuse reflectance mode.

Powder and paint-applied samples were analyzed by colorimetry, based on the CIEL*a*b* system, using a portable colorimeter (NR60CP – 3NH).

The oxidation state and elemental composition of the samples were evaluated using X-ray photoelectron spectroscopy (XPS) with a PHI Genesis instrument from Physical Electronics (Chanhassen, MN, USA), equipped with a monochromatic Al Kα X-ray source. The binding energy was calibrated based on the C 1s peak at 284.6 eV.

Laser-induced breakdown spectroscopy (LIBS) analyses were carried out by using the Applied Spectra J200 equipment. The clay samples were pelletized in circular discs of 1.2 cm and approximately 0.2–0.3 cm of height. The discs were prepared using 5 mg of each sample, and then they was pressed at 10 tons. The spectra were collected under air atmosphere between 186 and 1050 nm using a laser line at 50% as the source performing 10 shots per spot with 50 µm of diameter and gate delay of 0.5 µs.

A static laser scattering (SLS) Horiba LA-960 equipment assessed the powder particle size distribution measurements using a 15 mL cuvette accessory and water as the dispersion medium. The refractive index was set to 1.640 for red and blue lines.

Results and Discussion

The XRD profile for bentonite clay, niobium phosphate, niobium oxide and its modifications with niobium phosphate and niobium oxide (BEPh and BEOx, respectively), as well as the samples obtained after adsorption/photocatalysis of MB (A-BEPh, A-BEOx, A-BEPhP, A-BEOxP), are shown in Figure 2. The XRD analysis for bentonite before modification with niobium indicates dioctahedral montmorillonite (M-COD 9002779 $M_x(Al_{4-x}Mg_x)Si_8O_{20}(OH)_4$) with an amount of kaolinite (K-COD 1011045 $Al_2H_4O_9Si_2$) and quartz (Q-COD 9012600 SiO_2) at 13.8%, 41.6%, and 44.6%, respectively [8].

The characteristic reflections of montmorillonite (M) for the basal spacing correspond to approximately 15 Å (d001 = 14.88 Å), related to the interlayer distance of 2:1 clays, resulting in a spacing between 14.0–15.0 Å corresponding to the peak at 6.17 2θ (°) [11]. The quartz phase (Q) was identified by the presence of reflections at 2θ = 50.02° and 68.32°. The characteristic peaks that allowed the identification of the kaolinite phase (K) were at 2θ = 12.48° and 20.14° [7].

Figure 2a,b presents diffraction patterns with amorphous characteristics of the niobium compounds $NbOPO_4$ and Nb_2O_5. Two broad peaks were identified, one at approximately 25.54° (2θ) and the other at 49.73° (2θ) [12,13]. The amorphous pattern characteristic of niobium compounds was maintained upon modification of the bentonite clay with these compounds.
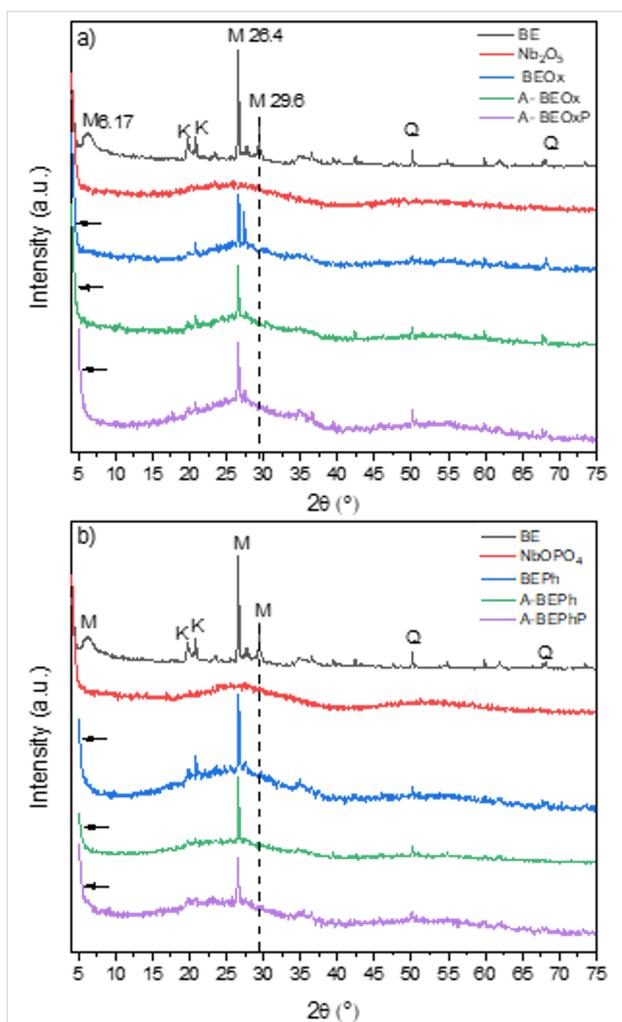
Figure 2: X-ray diffraction patterns of the bentonite samples and those modified with niobium oxide (a) and niobium phosphate (b).

The X-ray pattern of the samples of bentonite clay modified with the niobium compounds (BeOx and BEPh) and the same obtained after adsorption/photocatalysis of MB (A-BEPh, A-BEOx, A-BEPhP, and A-BEOxP) show the characteristic diffraction peak at approximately 26.4° (2θ) indicating that the niobium modification did not destroy the structure of the montmorillonite layer [14]. However, the relative intensity of the diffraction peak at 29.6° (2θ) decreased with the addition of the niobium compounds. This decrease can be attributed to the intercalation of the niobium in the interlayer of the clay, which increases the layer distance and the ion coordination of the interlayer to produce the polyhydroxyniobium. Another fact that can explain this result is the slight shifts of the montmorillonite characteristic diffraction peak (6.17° 2θ) to lower 2θ angles as observed in Figure 2a,b, suggesting increased interlayer space of the clay. The studies of Qiu et al. (2019) [14] and Gallo et al. (2006) [15] observed the same results, and indicated that the bentonite clay modified with niobium initiated the inorganic pillarization process from the polyhydroxyniobium process [14,15]. The supposed structure of bentonite clay modified with niobium phosphate and niobium oxide proposed in this study can be observed in Figure 3.

The FTIR spectra of the bentonite before and after modification with niobium are shown in Figure 4. It can be observed that for the BE samples and all those modified with $NbOPO_4$ (Figure 4a), the spectra show a narrow band in the region of 3638 cm^{-1}, associated with the (Al–OH–Al) Al_2OH vibrational stretching, indicative of bentonite with a high aluminum content in octahedra [7,16]. The spectra for the $NbOPO_4$ samples and for the bentonite modified with niobium phosphate (BEPh) before and after adsorption/photocatalysis (Figure 4a) show a
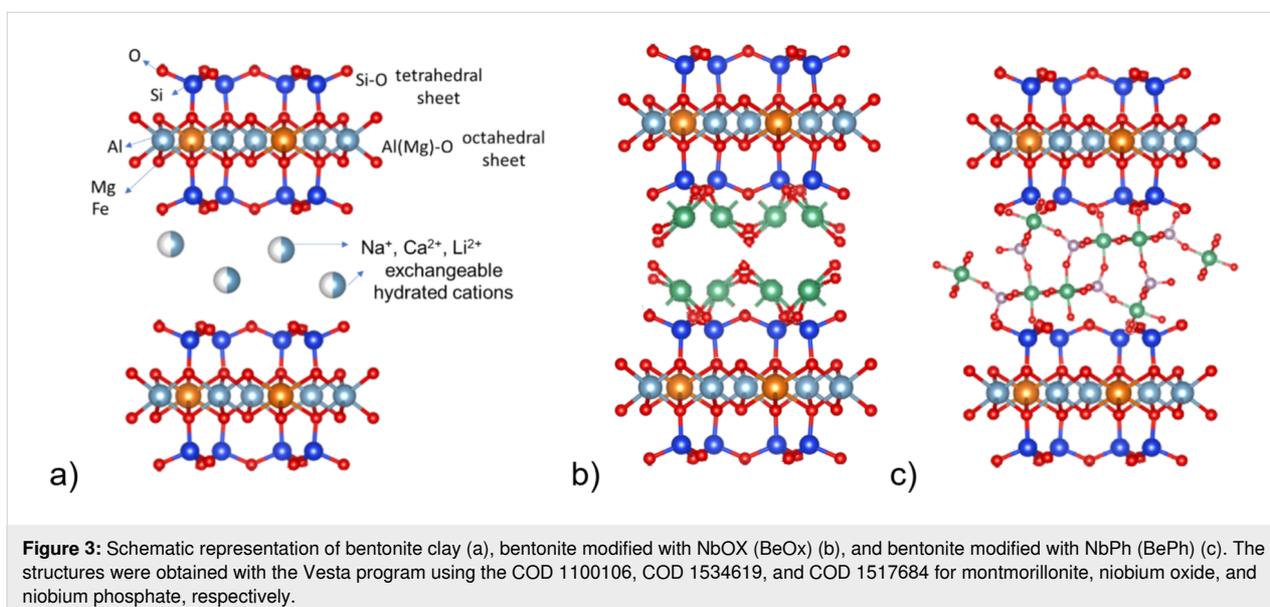
Figure 3: Schematic representation of bentonite clay (a), bentonite modified with NbOX (BeOx) (b), and bentonite modified with NbPh (BePh) (c). The structures were obtained with the Vesta program using the COD 1100106, COD 1534619, and COD 1517684 for montmorillonite, niobium oxide, and niobium phosphate, respectively.

band in the region of 1043 cm^{-1}, due to the vibrational mode (ν) of asymmetric stretching of the phosphate ion.
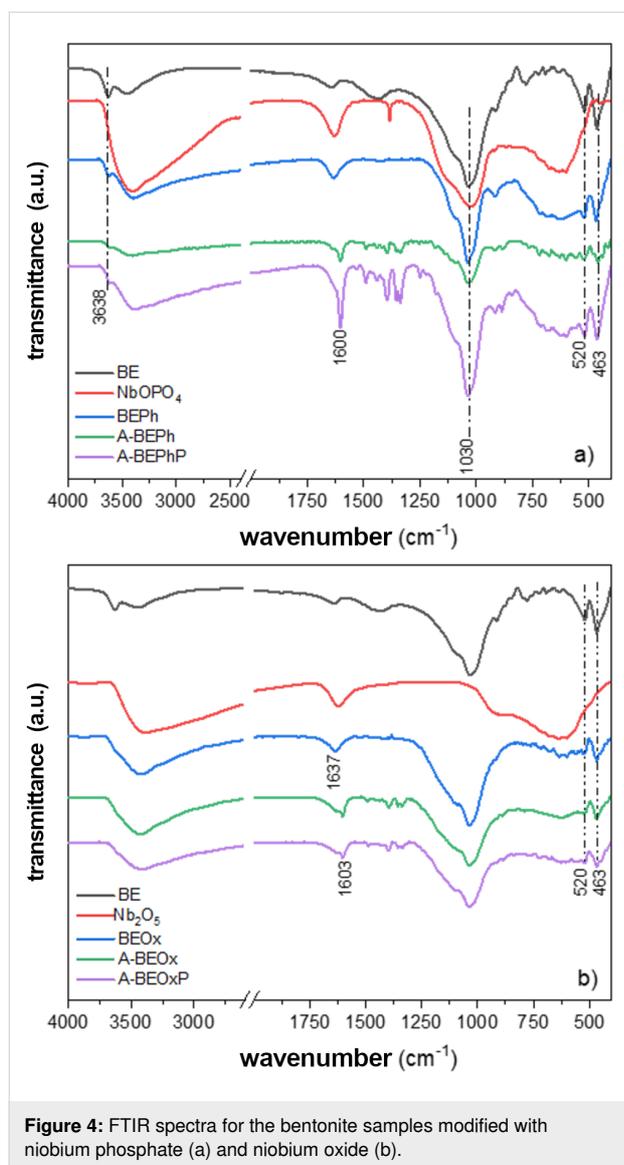
Figure 4: FTIR spectra for the bentonite samples modified with niobium phosphate (a) and niobium oxide (b).

The broad band in the region of 3385 cm^{-1} and the narrow band in the region of 1600 or 1637 cm^{-1} present in the spectrum for BE and the clay samples modified with NbOPO$_4$ and Nb$_2$O$_5$ are attributed to the stretching of hydroxyl and angular deformation of the water molecule, respectively [7,17]. The band in the region of approximately 1115 cm^{-1} is related to the stretching vibrations of Si–O. Bands in the region of 520 and 463 cm^{-1}, which appear in all spectra of bentonite and bentonite modified with niobium, are attributed to the stretching and bending of Si–O present in the clay layers [7].

The spectra for Nb$_2$O$_5$ and NbOPO$_4$ and the bentonite modified with niobium before and after adsorption/photocatalysis

present an intense band in the region of 630 cm^{-1} related to the stretching of the Nb–O bond. The A-BEPh, A-BEPhP, A-BEOx, and A-BEOxP samples exhibit a set of bands in the region from 1477 to 1277 cm^{-1} typical for the identification of the MB dye, indicating the presence of the dye in the clay structure [18].

Figure 5 shows the XPS analysis of niobium in BEOx and BEPh samples (Figure 4a and Figure 4b, respectively). The Nb 3d spectra exhibit two distinct peaks centered at 207.5 and 210.2 eV, corresponding to Nb 3d$_{5/2}$ and Nb 3d$_{3/2}$, respectively, indicative of niobium +5. The O 1s XPS spectra are shown in Figure 5c for BEOx and Figure 5d for BEPh. The spectra of samples BEOx and BEPh are reproduced with two components centered at 530.9 and 533.5 eV. The component centered at 531.0 eV can be attributed to photoelectrons emitted from oxygen atoms in Si–O, Al–O, or Nb–O bonds, whereas the low-intensity component at a higher binding energy can be associated with the hydroxyl OH$^-$ group of Nb–OH located in the interlayer region of the clay. These results confirm the increased interlayer space of the clay observed in DRX results (Figure 2). Figure 5e shows the O 1s spectrum recorded on sample BE. The high-intensity component centered at 532.0 eV is associated with oxygen bonds in Si–O–Si bonds [12].

Table 1 presents the chemical compositional analysis of the samples BE, BEOx, and BEPh determined by XPS. The results indicate that the bentonite clay modified with niobium phosphate (BEPh) exhibits a phosphorous content of 2.0% (wt %), thereby confirming the successful modification of the clay with this niobium compound. Furthermore, the samples BEOx and BEPh displayed niobium relative concentrations of 6.4 wt % and 4.0 wt %, respectively. These results suggest the incorporation of niobium into the clay matrix. In Table 1, considering the montmorillonite phase with the empirical formula M$_x$(Al$_{4-x}$Mg$_x$)Si$_8$O$_{20}$(OH)$_4$, when it was modified with the niobium compounds, the element sodium had its percentage decreased compared with that in the bentonite sample. However, the little change in the percentage of aluminum and silica, corresponding to the octahedral and tetrahedral layer, respectively, confirms that the niobium compounds are exchanged with sodium counter ions.

In recent years, laser-induced breakdown spectroscopy, an optical emission spectroscopic technique, has emerged as a rapid qualitative and quantitative analysis [19]. This spectroscopic technique can be explained by the short-duration, high-intensity pulsed laser being focused on a material, producing a plasma called laser-induced plasma (LIP). Qualitative and quantitative information about a sample is obtained by measuring the spectral delivery of the laser-induced plasma [19].

Figure 5: Photoelectron spectroscopy results for Nb3d (a and b for the samples BEOx and BEPh, respectively), O 1s (c, d, and e for the samples BEOx, BEPh, and BE, respectively).
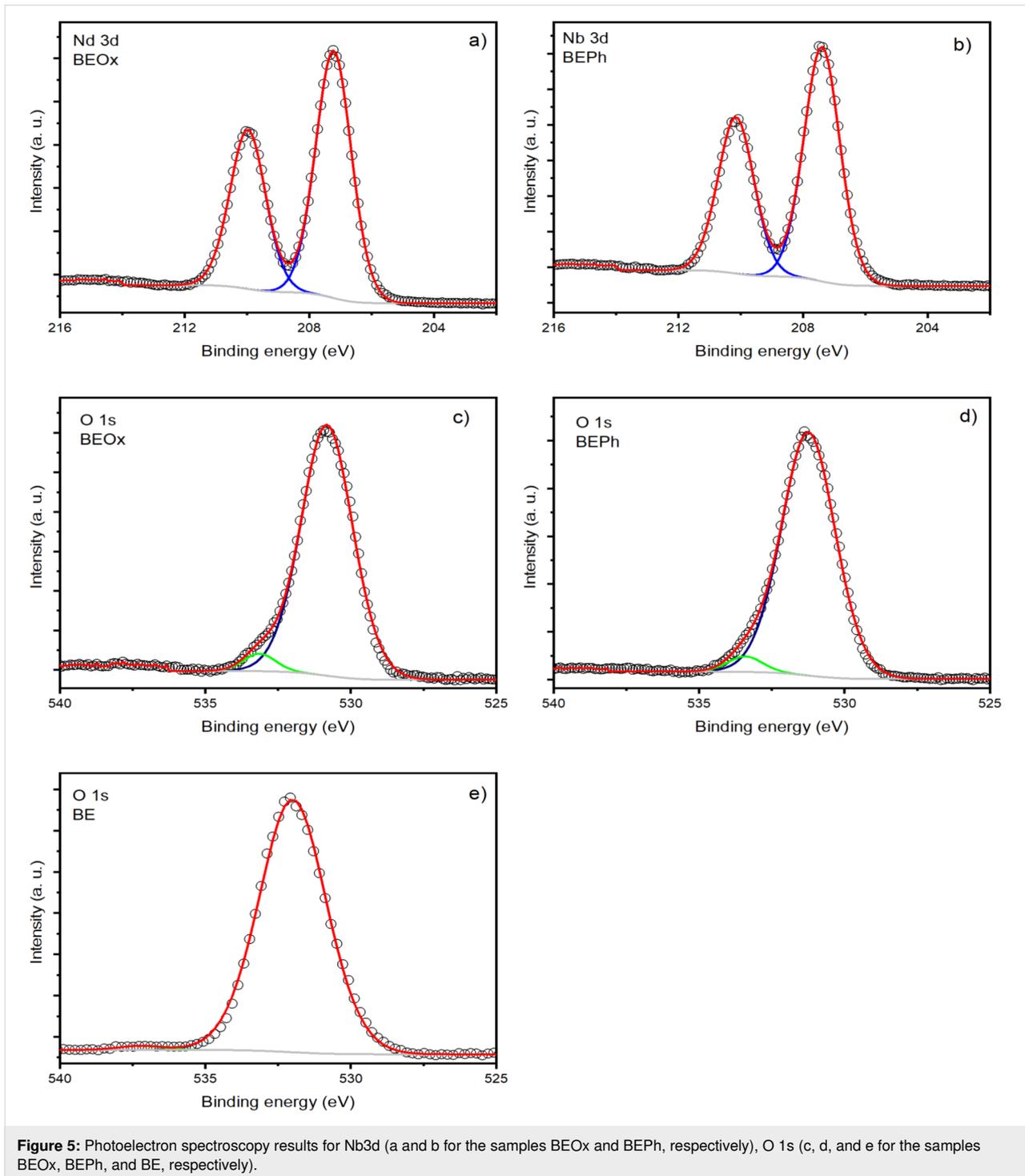
Figure 6 shows LIBS spectra for the samples BE, BEPh, and BEOx. It is observed that the samples containing niobium show a higher density of spectral lines. For the sample BE, the principal emissions lines for Mg^{2+}, Al^{3+}, Na^+, at around 279 nm, 309 nm and 589 nm, respectively, are consistent with the montmorillonite structure, and these results are coherent with XPS composition in Table 1. The modification of the clay samples with niobium was characterized by the presence of many other lines throughout the spectrum region, which highlighted the lines at 666 nm. XPS analysis (Table 1), as well as the XRD results (Figure 2), suggest that the niobium compounds ($NbOPO_4$ and Nb_2O_5) were exchanged with Na^+ ions of the clay, due to the decreased percentage of these elements in XPS composition as observed in Figure 5. The LIBS results showed

Table 1: Composition of the samples BE, BEOx, and BEPh determined by XPS.

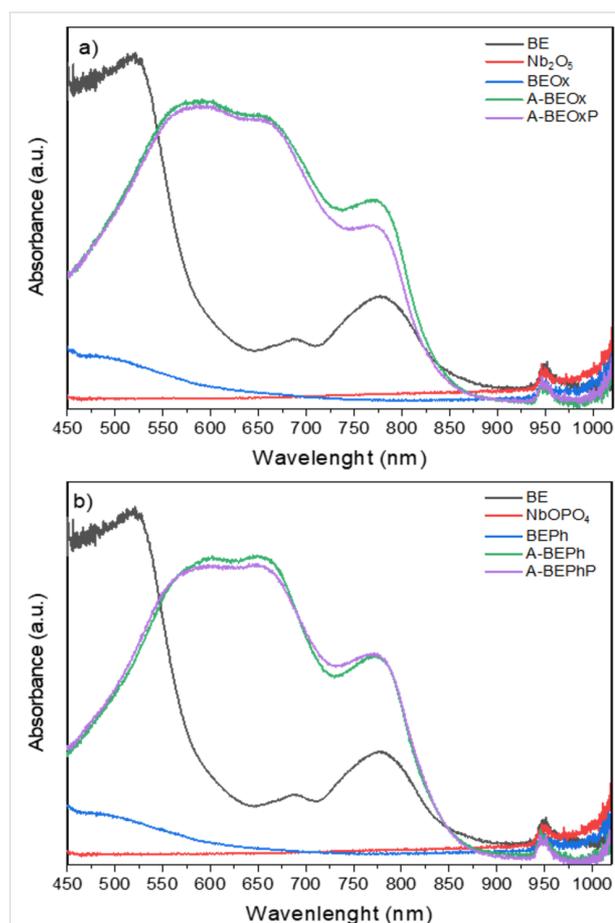| Samples	wt %											
	C	N	O	F	Na	Mg	Al	Si	P	Ca	Nb	Fe
BEOx	6.4	–	62.5	1.1	2.6	2.1	4.8	13.1	–	1.0	6.4	–
BEPh	7.9	1.5	62.7	1.0	1.7	1.3	4.4	12.5	2.0	1.0	4.0	–
BE	9.3	–	55.0	–	6.0	3.8	6.5	17.5	–	1.4	–	0.5

the presence of lines of Mg and Na for the BE sample, at around 280 nm and 819 nm, respectively. As demonstrated in Table 1, the compositions of Na were reduced when the BE sample was modified with niobium compounds.
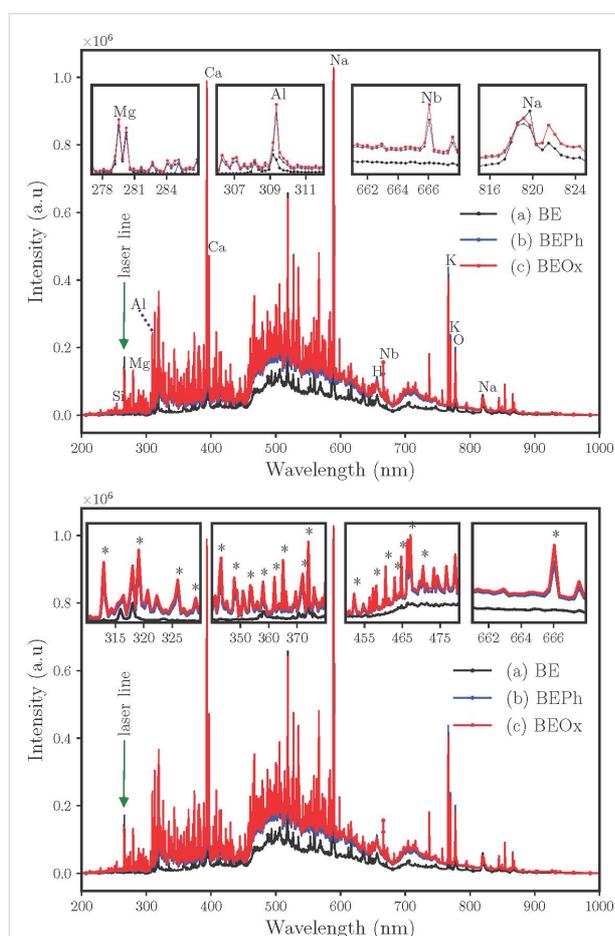
Figure 6: Laser-induced breakdown spectroscopy analysis for the samples BE (a), BEPh(b) and BEOx (c).

The average particle size for the samples BE, NbPh, and NbOx were 12, 410, and 54 μm, respectively, and it is present in Supporting Information File 1, Figure S1. The BEPh and BEOx samples presented different particle size distributions, so the average particle size (D50) for them was 4.52 and 86 μm, respectively. These values indicate that the clay aggregates are disso-

ciated and well dispersed, as shown in the study by Yang et al. [20].

The absorbance spectra profiles in the visible region for the bentonite samples and bentonite modified with niobium are presented in Figure 7. It can be observed that the NbOPO$_4$ and Nb$_2$O$_5$ powder samples do not show an absorption band. However, the bentonite modified with these compounds exhibited a band with a maximum of 493 nm. The samples BEOx and BEPh obtained after adsorption/photocatalysis present profiles like BE clay, with intense absorption in the UV region with a


Figure 7: The absorption spectra in the visible region for the samples of bentonite and their modifications with niobium oxide (a) and niobium phosphate(b).

sharp drop of around 550 nm [8]. This fact indicates the feasibility of activating the A-BEPh, A-BEPhP, A-BEOx, and A-BEOXPh samples under visible light (above 400 nm) [8].

The indirect bandgap energy values for the BE, NbOPO$_4$ and Nb$_2$O$_5$ and the bentonite clay modified with niobium BEPh and BEOx samples were estimated by the Tauc method [21]. For this, Kubelka–Munk method was applied as observed in Supporting Information File 1, Figure S2. The bandgap value of the BE sample (3.2 eV) was slightly higher than for the NbOPO$_4$ and Nb$_2$O$_5$ compounds (3.13 and 3.2 eV, respectively). The calculated bandgap is coherent with the literature, Nakhaei et al. (2019) [22] obtained a value of 3.6 eV for bentonite clay, and for the niobium compounds Ücker et al. 2018 obtained the values of a bandgap equal to 3.0 eV [23]. The bentonite clay

samples modified with niobium (BEOx and BEPh) remained with bandgap values lower compared with the clay, 3.07 and 3.13 eV, respectively. These values are consistent with the results of the study by Ascencios et al. 2019 [8] in which obtained bandgap values to clay/Nb were around 3.0 and 3.38 eV. The small decrease in values occurred due to the bentonite clay with high bandgap values, which generated impurity energy levels above the valence band edge. This results in lower energy values required to excite charge carriers, reducing the optical band [24].

Figure 8 shows the results of the comparison obtained regarding the percentage of removal from adsorption and heterogeneous photocatalysis tests. The photocatalysis mechanism can be explained as follows: a semiconductor such as the BEPh and
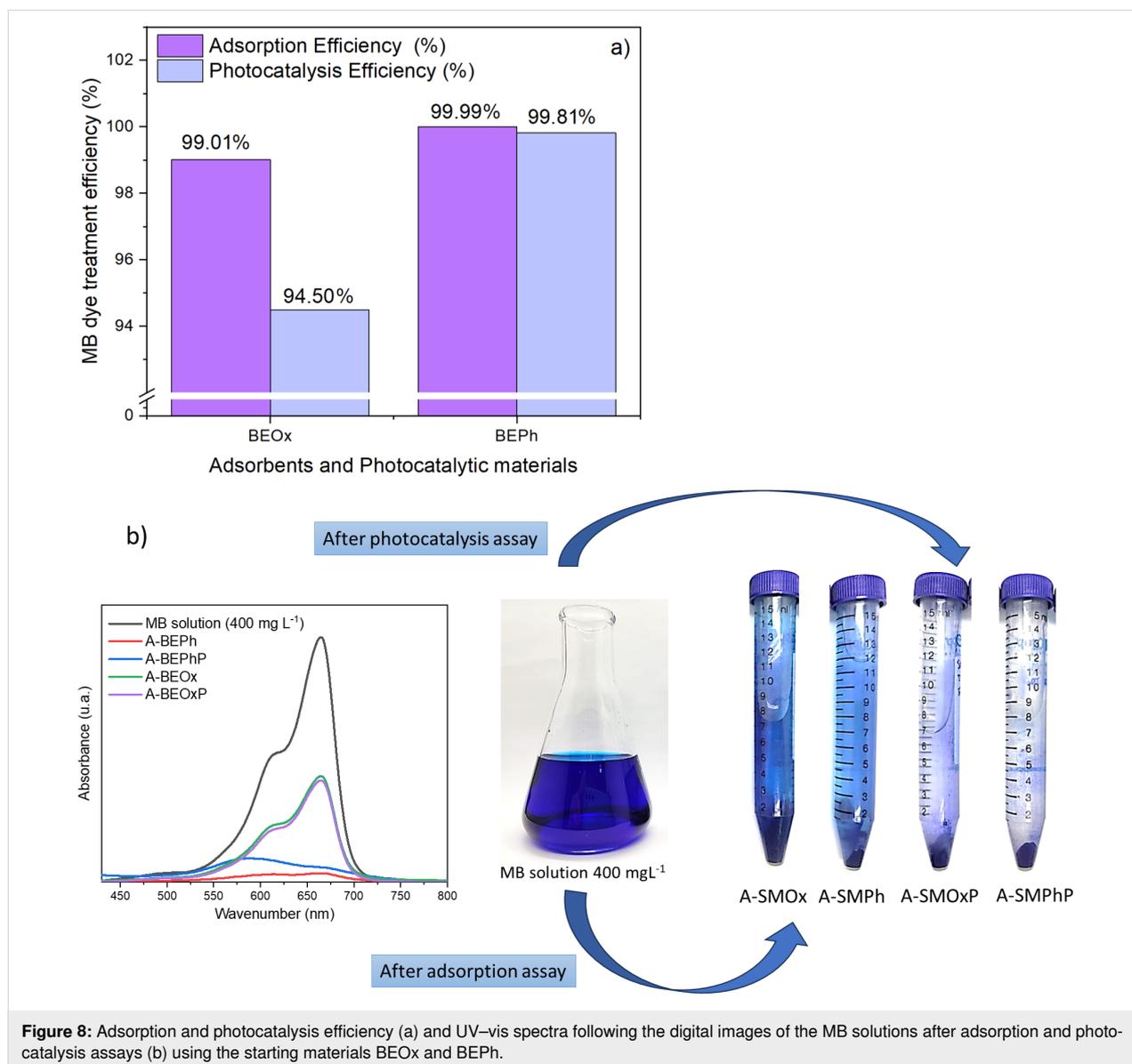
Figure 8: Adsorption and photocatalysis efficiency (a) and UV–vis spectra following the digital images of the MB solutions after adsorption and photocatalysis assays (b) using the starting materials BEOx and BEPh.

BEOx samples absorbs a photon, promoting an electron from the valence band (V_B) to the conduction band (C_B), creating a hole in the valence band (h_{BV}^+) [8]. These holes induce the oxidative decomposition of organic molecules adsorbed on the catalytic surface. They also react with water molecules, producing the hydroxyl radical (OH$^•$). This radical rapidly attacks the dye molecules in the solution, leading to mineralization into CO_2 and H_2O [8].

According to the observed results, the BEOx and BEPh samples notably exhibited higher efficiency in the adsorption process (99.01% and 99.99%, respectively) than in photocatalysis. This phenomenon can be attributed to the negative surface charge of the modified clays BEOx and BEPh, which exhibit a strong affinity with the positively charged structure of the MB dye. On the other hand, the BEOx and BEPh samples demonstrated significant efficacy in MB removal, with removal rates of 94.5% and 99.81%, respectively. The preferential electron–hole (h_{BV}^+) favoring of the BEOx catalyst hindered its photocatalytic activity [8].

In a study by Asencios et al. (2019) [8], niobium-modified clay was explored for the photocatalysis of rhodamine B dye, yielding removal rates close to 95%. Additionally, Lacerda et al. (2020) [25] achieved up to 90% efficiency in the removal of reactive blue 19 dye using niobium-modified bentonite. These reports demonstrate that the material obtained in this study presents high values of MB removal under UV light, standing out as a novel material.

The absorbance profiles of the niobium-modified samples dispersed in clear paint are shown in Supporting Information File 1, Figure S3. It is possible to observe that the BEOx and BEPh samples dispersed in clear paint, despite presenting a yellow coloration, did not show absorption bands. The samples collected after the adsorption/photocatalysis assays exhibited bands in the maximum region at 664 nm, corresponding to the $\pi \to \pi^*$ electronic transitions of the adsorbed MB dye [26].

Table 2 and Table 3 and Supporting Information File 1, Figures S4 and S5 present the values of the CIEL*a*b* colorimetric parameters for the samples BEOx and BEPh (powder sample, cycle) even as they disperse in colorless paint (paint sample, square), respectively. The tables also include color difference values between the samples in powder form and those dispersed in colorless paint. Colorless paint does not contain white pigment in its matrix, enhancing the dispersed pigment color. The ΔE parameter quantified the color difference between two samples, BEOx and BEPh, in powder form and those dispersed in colorless paint. As observed, the results of ΔE show that the samples A-BEPhP (12.17) and BEOx (9.82) before the adsorp-

tion/photocatalysis process when dispersed in colorless paint demonstrate a strong color parameter difference (ΔE = 6–12). The ΔE values obtained for the samples BEPh (13.62) before the adsorption/photocatalysis process, A-BEPh (23.38), A-BEOx (15.97), and A-BEOxP (13.80) were above 12, indicating a very strong color parameter difference [27].

The colorimetric parameters presented in Table 2 and Table 3 and in Supporting Information File 1, Figures S2 and S3 demonstrate that the test specimens painted with niobium-modified clay before the adsorption/photocatalysis of MB show higher luminosity (L). When the clay samples were colored MB, after the adsorption/photocatalysis process, the luminosity decreased. The A-BEPhP sample shows a slight tendency towards green coloration (-a*). On the other hand, when evaluating the b* parameter, it is observed that all samples obtained after adsorption/photocatalysis of MB (A-BEPh, A-BEPhP, A-BEOx and A-BEOxP), whether in powder form or dispersed in paint, show a tendency towards blue coloration, as observed in the negative b* values.
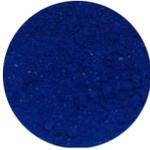
The BEPh, BEOx, A-BEPh, A-BEOx, A-BEPhP, and A-BEOxP samples were evaluated for their in vitro antibacterial capacity using the minimum inhibitory concentration (MIC) method against the pathogenic bacteria *Proteus mirabilis* and *Bacillus cereus*. The results obtained are presented in Table 4.

The samples A-BEPh, A-BEPhP, A-BEOx, and A-BEOxP demonstrated antibacterial activity against the *Proteus mirabilis* bacterial strains, with MIC values recorded at 0.31, 0.15, 0.31, and 0.62 mg/mL, respectively. In contrast, the BEPh and BEOx samples exhibited no inhibitory effects at the tested concentrations for this microorganism.

Observing the adsorption and photocatalysis efficiency in Figure 8a, similar values for the samples BEPhP and BEPh were obtained (99.81% and 99.81%, respectively) that is, the amount of dye present in these samples is practically the same. The MIC results of these samples indicated 0.15 mg/mL and 0.31 mg/mL for the samples A-BEPhP and A-BEPh, respectively. The adsorption and photocatalysis efficiency for the samples BEOxP and BEOx were 94.50% and 99.01%, respectively. These results suggest that sample A-BeOX contains a larger amount than sample A-BePh. The A-BEOxP sample yielded an MIC of 0.62 mg/mL, while the A-BEOx had an MIC of 0.31 mg/mL, indicating a more effective antibacterial action against the tested strains.

It is noteworthy that antibacterial activity was only observed in materials that had the addition of methylene blue, highlighting the influence of the dye on the assay outcomes. According to

Table 2: Colorimetric parameters obtained by the CIEL*a*b* system for the BEPh samples before and after the adsorption/photocatalysis assays in powder form (circle) and dispersed in colorless paint (square).

Sample	Colorimetric parameters						Images of the sample
	L*	a*	b*	C*	h	ΔE	
BEPh	77.02	2.47	10.38	10.67	76.67	–	
BEPh	90.54	2.19	12.03	12.23	68.01	13.62	
A-BEPh	13.45	4.91	−36.34	36.67	277.69	–	
A-BEPh	32.05	3.15	−22.29	22.51	278.05	23.38	
A-BEPhP	31.91	−5.08	−21.03	21.63	256.42	–	
A-BEPhP	32.98	5.97	−26.01	26.68	282.92	12.17	

Thesnaar (2021) [28], many studies have demonstrated that methylene blue, either alone or in combination with other compounds, possesses antibacterial activity; however, the precise mechanism of action remains unclear. The BEPh, BEOx, A-BEPh, A-BEOx, A-BEPhP, and A-BEOxP samples did not exhibit minimum inhibitory activity against the other studied bacterial strain *Bacillus cereus*.
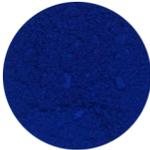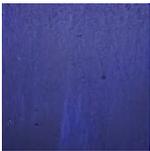
These results highlight the selectivity of the studied samples (A-BEPh, A-BEPhP, A-BEOx, and A-BEOxP) in inhibiting Gram-negative bacteria, which typically exhibit increased resistance due to the presence of an outer membrane that protects them from certain antimicrobial agents [29]. Therefore, the pre-

liminary results indicate that bentonite clay modification with niobium oxide (BEOx) and niobium phosphate (BEPh), when adsorbed and/or photocatalyzed for the treatment of wastewater containing MB, demonstrates promising selective antibacterial activity against Gram-negative bacteria.

Conclusion

In conclusion, the presented study demonstrates that the modification of bentonite clay with niobium phosphate and niobium oxide can be achieved through a simple and low-cost procedure. The XRD results revealed that the raw bentonite contains additional phases such as kaolinite and quartz. The niobium incorporated into bentonite clay (BEPh and BEOx) indicated that the

Table 3: Colorimetric parameters obtained by the CIEL*a*b* system for the BEPh samples before and after the adsorption/photocatalysis assays in powder form (circle) and dispersed in colorless paint (square).

Sample	Colorimetric parameters						Images of the sample
	L	a*	b*	C*	h	ΔE	
BEOx	80.96	3.07	13.17	11.05	73.85	–	
BEOx	90.42	0.71	12.03	9.63	85.78	9.82	
A-BEOx	22.91	13.94	–36.80	39.55	290.74	–	
A-BEOx	30.93	6.79	–24.99	25.90	285.20	15.97	
A-BEOxP	18.25	7.90	–30.06	31.00	284.72	–	
A-BEOxP	30.65	7.15	–24.06	25.10	286.54	13.80	

Table 4: MIC (mg/mL) for the in vitro antibacterial activity in water.

Sample	BEPh	BEOx	A-BEPh	A-BEOx	A-BEPhP	A-BEOxP
MIC *P. mirabilis*	–[a]	–[a]	0.31	0.31	0.15	0.62

[a]MIC values were not determined.

niobium modification did not destroy the structure of the montmorillonite layer, as indicated by the XRD results. Furthermore, analyses using XPS and LIBS confirmed that the niobium compounds exchanged with Na^+ ions of the clay tetrahedral sheet.

The bentonite sample, along with the BEPh and BEOx samples, exhibited adsorption and photocatalytic efficiencies exceeding 94% for the removal of MB in water. This process resulted in a final blue-colored product as evidenced by the colorimetric pa-

rameters obtained through the CIEL*a*b* color space. The samples derived from the adsorption/photocatalysis tests (A-BEPh, A-BEPhP, A-BEOx, and A-BEOxP) demonstrate significant antibacterial activity against the Gram-negative bacteria *Proteus mirabilis*, highlighting the influence of the dye in the assay outcomes.

The implications of this work extend to the development of a novel hybrid pigment. This pigment, synthesized from abundant natural clays of the Guarapuava region in conjunction with niobium, an abundant metal in Brazil, is easily synthesized, cost-effective, and has potential to be used as a pigment in commercial paints. Moreover, it exhibits antibacterial properties against pathogens responsible for various diseases, including ocular and ear infections.

Supporting Information

Supporting Information File 1
Additional figures.
[https://www.beilstein-journals.org/bjnano/content/supplementary/2190-4286-16-13-S1.pdf]

Acknowledgements

Funding

Author Contributions
Silvia Jaerger: conceptualization; data curation; formal analysis; investigation; methodology; project administration; resources; validation; visualization; writing – original draft; writing – review & editing. Patricia Appelt: conceptualization; data curation; formal analysis; investigation; methodology; validation; writing – original draft; writing – review & editing. Mario Antônio Alves da Cunha: investigation; methodology; visualization. Fabián Ccahuana Ayma: data curation; methodology; software. Ricardo Schneider: data curation; formal analysis; methodology; software; validation; visualization; writing – original draft; writing – review & editing. Carla Bittencourt: conceptualization; data curation; formal analysis; investigation; methodology; visualization; writing – original draft; writing –

review & editing. Fauze Jacó Anaissi: conceptualization; data curation; formal analysis; investigation; methodology; project administration; supervision; validation; visualization; writing – original draft; writing – review & editing.

ORCID® iDs
Patricia Appelt - https://orcid.org/0000-0003-4302-534X
Fabián Ccahuana Ayma - https://orcid.org/0000-0002-5610-0559
Ricardo Schneider - https://orcid.org/0000-0001-9501-8489
Carla Bittencourt - https://orcid.org/0000-0002-3330-6693
Fauze Jacó Anaissi - https://orcid.org/0000-0002-5454-472X

Data Availability Statement
Data generated and analyzed during this study is available from the corresponding author upon reasonable request.

Preprint
A non-peer-reviewed version of this article has been previously published as a preprint: https://doi.org/10.3762/bxiv.2024.59.v1

References
1. Saber-Samandari, S.; Saber-Samandari, S.; Joneidi-Yekta, H.; Mohseni, M. *Chem. Eng. J.* **2017,** *308,* 1133–1144. doi:10.1016/j.cej.2016.10.017
2. Bingül, Z. *J. Mol. Struct.* **2022,** *1250,* 131729. doi:10.1016/j.molstruc.2021.131729
3. Nayl, A. A.; Abd-Elhamid, A. I.; Arafa, W. A. A.; Ahmed, I. M.; AbdEl-Rahman, A. M. E.; Soliman, H. M. A.; Abdelgawad, M. A.; Ali, H. M.; Aly, A. A.; Bräse, S. *Materials* **2023,** *16,* 514. doi:10.3390/ma16020514
4. Ma, L.; Islam, S. M.; Xiao, C.; Zhao, J.; Liu, H.; Yuan, M.; Sun, G.; Li, H.; Ma, S.; Kanatzidis, M. G. *J. Am. Chem. Soc.* **2017,** *139,* 12745–12757. doi:10.1021/jacs.7b07123
5. Li, K.; Zheng, Z.; Feng, J.; Zhang, J.; Luo, X.; Zhao, G.; Huang, X. *J. Hazard. Mater.* **2009,** *166,* 1180–1185. doi:10.1016/j.jhazmat.2008.12.035
6. Akhtar, J.; Amin, N. A. S.; Shahzad, K. *Desalin. Water Treat.* **2016,** *57,* 12842–12860. doi:10.1080/19443994.2015.1051121
7. Rocha, M. L. M.; Balaba, N.; Jaerger, S.; Primo, J. O.; Horsth, D. F. L.; Appelt, P.; Meneguzzi, D.; Cunha, M. A. A.; Anaissi, F. J. *Minerals (Basel, Switz.)* **2023,** *13,* 785. doi:10.3390/min13060785
8. Asencios, Y. J. O.; Quijo, M. V.; Marcos, F. C. F.; Nogueira, A. E.; Rocca, R. R.; Assaf, E. M. *Sol. Energy* **2019,** *194,* 37–46. doi:10.1016/j.solener.2019.10.005
9. *M 07 Methods for Dilution Methods for Dilution Antimicrobial Susceptibility Tests for Bacteria that Grow Aerobically,* 11th ed.; Clinical and Laboratory Standards Institute (CLSI): Wayne, PA, USA, 2018.
10. Balouiri, M.; Sadiki, M.; Ibnsouda, S. K. *J. Pharm. Anal.* **2016,** *6,* 71–79. doi:10.1016/j.jpha.2015.11.005
11. Chen, J.; Lu, J.; Su, L.; Ruan, H.; Zhao, Y.; Lee, C.; Cai, Z.; Wu, Z.; Jiang, Y. *Appl. Sci.* **2022,** *12,* 3182. doi:10.3390/app12063182
12. Marin, L. M.; Hallett-Tapley, G. L.; Impellizzeri, S.; Fasciani, C.; Simoncelli, S.; Netto-Ferreira, J. C.; Scaiano, J. C. *Catal. Sci. Technol.* **2014,** *4,* 3044–3052. doi:10.1039/c4cy00238e

13. Liang, F.; Wu, D.; Jiang, L.; Zhang, Z.; Zhang, W.; Rui, Y.; Tang, B.; Liu, F. *ACS Appl. Mater. Interfaces* **2021,** *13,* 51057–51065. doi:10.1021/acsami.1c15763

14. Qiu, G.; Huang, C.; Sun, X.; Chen, B. *Green Chem.* **2019,** *21,* 3930–3939. doi:10.1039/c9gc01225g

15. Gallo, J. M. R.; Teixeira, S.; Schuchardt, U. *Appl. Catal., A* **2006,** *311,* 199–203. doi:10.1016/j.apcata.2006.06.019

16. Madejová, J. *Vib. Spectrosc.* **2003,** *31,* 1–10. doi:10.1016/s0924-2031(02)00065-6

17. Zhang, Y.; Wang, J.; Ren, J.; Liu, X.; Li, X.; Xia, Y.; Lu, G.; Wang, Y. *Catal. Sci. Technol.* **2012,** *2,* 2485–2491. doi:10.1039/c2cy20204b

18. Raiyaan, G. I. D.; Kalith, S. B. M.; Sheriff, M. A.; Arunachalam, K. D. *J. Aquacult. Mar. Biol.* **2021,** *10,* 146–150. doi:10.15406/jamb.2021.10.00316

19. Singh, P.; Mal, E.; Khare, A.; Sharma, S. *J. Cult. Heritage* **2018,** *33,* 71–82. doi:10.1016/j.culher.2018.03.011

20. Yang, T.; Wang, N.; Gu, H. *Appl. Clay Sci.* **2023,** *235,* 106866. doi:10.1016/j.clay.2023.106866

21. Borth, K. W.; Galdino, C. W.; Teixeira, V. d. C.; Anaissi, F. J. *Appl. Surf. Sci.* **2021,** *546,* 149126. doi:10.1016/j.apsusc.2021.149126

22. Nakhaei, M.; Barzgari, Z.; Mohammadi, S. S.; Ghazizadeh, A. *Res. Chem. Intermed.* **2019,** *45,* 4995–5005. doi:10.1007/s11164-019-03877-2

23. Ücker, C. L.; Gularte, L. T.; Fernandes, C. D.; Goetzke, V.; Moreira, E. C.; Raubach, C. W.; Moreira, M. L.; Cava, S. S. *J. Am. Ceram. Soc.* **2019,** *102,* 1884–1892. doi:10.1111/jace.16080

24. Zainab, S.; Azeem, M.; Awan, S. U.; Rizwan, S.; Iqbal, N.; Rashid, J. *Sci. Rep.* **2023,** *13,* 6954. doi:10.1038/s41598-023-33200-4

25. Hass Caetano Lacerda, E.; Monteiro, F. C.; Kloss, J. R.; Fujiwara, S. T. *J. Photochem. Photobiol., A* **2020,** *388,* 112084. doi:10.1016/j.jphotochem.2019.112084

26. Kostjukova, L. O.; Leontieva, S. V.; Kostjukov, V. V. *J. Mol. Liq.* **2021,** *336,* 116369. doi:10.1016/j.molliq.2021.116369

27. Quindici, M. *O Segredo das Cores;* All Print: São Paulo, Brazil, 2013.

28. Thesnaar, L.; Bezuidenhout, J. J.; Petzer, A.; Petzer, J. P.; Cloete, T. T. *Eur. J. Pharm. Sci.* **2021,** *157,* 105603. doi:10.1016/j.ejps.2020.105603

29. Ramachandran, G. *Virulence* **2014,** *5,* 213–218. doi:10.4161/viru.27024